POLITECNICO DI TORINO

DIPARTIMENTO DI ENERGETICA

Corso di Laurea Magistrale in
Ingegneria Energetica e Nucleare

Tesi di Laurea Magistrale

Study on the dynamics of the flexible cables of a KITE-GEN type of energy generator

Relatore
Prof.ssa Daniela Tordella

Correlatore
Prof. Giancarlo Abbate

Candidato
Felice Roselli

Marzo 2016

Abstract

The aim of this work was to evaluate the aerodynamic drag force generated by the cables connecting a kite to the ground station of a KiteGen system, one of the most promising technology in the field of the high altitude wind power generation. In particular, the accuracy of the most used approximation in this field, which considers the cables as straight lines, was investigated. This need has emerged due to experimental observations performed by KiteGen Research during the flight of their power kites. It has been noticed, indeed, that the ropes configuration strongly differs from that of two straight lines and, in particular, the ropes tend to follow the kite movement mainly with their highest portion, while the remaining part of the ropes tends to stay quieter closer to the axis of the kite trajectory. This behavior has a huge impact on the estimation of velocity with which the ropes move in the air and therefore on the estimation of the aerodynamic drag of the cables. The drag force of the cables is a key aspect to be considered in the estimation of the global system aerodynamic efficiency G_e, whose value affect the shape of the power curves. In general, the longer are the ropes and the higher will be the value of the cable aerodynamic drag force F_t and, as a consequence, the smaller will be G_e, since they are inversely proportional. A smaller value of G_e implies the need of stronger winds to produce a certain amount of power. On the other side, having longer ropes allows one to operate at higher altitude, where stronger winds are available. A correct estimation of F_t is therefore essential in order to have a realistic value of G_e and to evaluate the optimal cables length which allow to maximize the energy production.

Hence, in this thesis, the aerodynamic drag generated by the cables has been first evaluated considering the ropes as straight rigid lines, to create a reference case, and then as flexible ropes. In the second case, the position assumed by the ropes during the flight cannot be know a priori and, in order to find it, a dynamic system was set. The system has been derived from the application of the Newton's law of motion to the ropes and had as unknown also the variable tension along the ropes. In particular, the main forces acting on that system were considered: the aerodynamic drag force, the gravity and the variable tension along the ropes. The system was numerically solved considering as boundary conditions the movement at constant tangential velocity of the kite on a realistic eight-shaped trajectory and the constant value of the tension of the ropes at the generators. Moreover, another realistic phenomenon was considered, the unrolling of cables during the KiteGen operations. The found solution clearly indicate a discordance between the cables configuration and the positions of two ideal straight lines. The calculations have been performed exploring the cables length range between 500 m and 3000 m. It has been found that with ropes length between 500 m and roughly 900 m, the two approaches give the same value of the cables aerodynamic resistance. Nevertheless for ropes longer than 900 m it has been found that the straight lines approach gives a quasi-linear increase value of F_t as function of the cable length, while with the second approach F_t tends asymptotically to a lower value. It can be noticed then a significant difference between the two approaches.

In order to evaluate the energy obtainable from a KiteGen system it is needed to know the wind probability density function for a given location at different elevations from the ground.

To this purpose, the RAOB (Rawinsonde Observations) database of the National Oceanographic and Atmospheric Administration (NOAA) has been used to evaluate the wind probability density functions for the specific site of De Bilt, in The Netherlands. It has been shown that, with the present analysis, the maximum energy production for the specific location of De Bilt is reached with $500m$ long cables, a length for which both the approaches used give the same value of the cables drag force, while with longer ropes the value the annual energy production starts to the decrease. Nevertheless, starting from roughly $900m$, the difference in the estimation of AEP with the two approaches becomes significantly evident.

It has been highlighted, therefore, the need of a deeper study on the dynamics of the kite lines since there are still some physical phenomena which have been ignored in this work and that could possibly reduce the value of the cables drag force and maybe change the trend of the AEP as function of the cables length. Hence, for future works, the main phenomena to be added to the present analysis are the elasticity of the ropes, the finite velocity of propagation of the pulses that the kite movement sends to the ropes and the internal damping. Moreover, also the possibility of adopting special cables with reduced drag coefficient should be considered.

Riassunto

Lo scopo di questo lavoro di Tesi è stato quello di valutare la forza aerodinamica resistente generata dai cavi che connettono l'aquilone di potenza (kite) alla sala macchine di un sistema KiteGen, una delle tecnologie più promettenti nell'ambito della produzione di energia elettrica da venti di alta quota. In particolare, è stata studiata l'accuratezza dell'approssimazione più utilizzata in questo ambito scientifico, ovvero quella secondo la quale la configurazione assunta dai cavi durante il volo del kite sia approssimabile a delle linee rette e rigide. La necessità di questo studio è emersa a causa di osservazioni sperimentali condotte da KiteGen Research durante il volo dei loro aquiloni di potenza. E' stato notato, infatti, che la configurazione assunta dalle funi differisce fortemente da quella di due linee dritte e che, in particolare, le funi tendono a seguire il movimento del kite principalmente con la loro porzione più alta, mentre la restante parte dei cavi tende a rimanere più ferma vicino all'asse della traiettoria del kite. Questo comportamento ha una forte influenza sulla velocità con cui le funi si muovono nell'aria e quindi sulla stima della loro resistenza aerodinamica. Quest'ultima è un aspetto chiave da considerare nella stima dell'efficienza aerodinamica globale del sistema G_e, il cui valore determina la forma delle curve di potenza della tecnologia. In generale, più lunghe sono le funi e più alto sarà il valore della loro resistenza aerodinamica F_t e quindi più basso sarà invece G_e, essendo questo inversamente proporzionale a F_t. Un valore più basso di G_e implica la necessità di venti più potenti per produrre una certa quantità di potenza. D'altro canto, avere cavi più lunghi permette di operare a quote più elevate, dove vi è effettivamente disponibilità di venti più forti e costanti durante l'anno. Una corretta valutazione della resistenza aerodinamica dei cavi, quindi, è essenziale allo scopo di ottenere un realistico valore di G_e e quindi per valutare la lunghezza ottimale delle funi che permette di massimizzare l'energia prodotta.
Per questo motivo, in questo lavoro, il valore della resistenza aerodinamica delle funi è stata valutata prima utilizzando l'approssimazione delle funi come linee rigide, allo scopo di creare un caso base di riferimento, e poi considerando le funi come flessibili. Nel secondo caso, la posizione assunta dai cavi durante il volo del kite non può essere conosciuta a priori e, allo scopo di trovarla, è stato impostato un sistema dinamico. Il sistema è stato derivato dall'applicazione della Seconda legge di Newton alle funi e come incognite, oltre alla già menzionata posizione delle funi, era presente anche il valore della tensione lungo le funi stesse. Le principali forze agenti sul sistema sono state considerate, ovvero la resistenza aerodinamica, la forza peso e la tensione variabile lungo le funi. Il sistema è stato risolto numericamente avendo come condizioni al contorno il movimento a velocità tangenziale costante del kite e il valore costante della tensione dei cavi in corrispondenza dei generatori elettrici. Inoltre, altre condizioni realistiche sono state utilizzate, ovvero una traiettoria realistica del kite durante il suo volo (in particolare a forma di otto) e lo srotolamento dei cavi dai generatori elettrici a causa della forza di trazione generata dall'aquilone. Le simulazioni computazionali sono state realizzate facendo srotolare i cavi da una lunghezza iniziale di $500m$ fino ad una lunghezza di $3000m$. Si è trovato che per funi di lunghezza compresa tra i $500m$ e circa $900m$ i due approcci danno lo stesso valore di resistenza aerodinamica, tuttavia per funi più lunghe di $900m$ si è trovato che l'approccio funi rigide

dà un valore di F_t che continua a crescere in maniera quasi lineare, mentre con l'approccio funi flessibili F_t tende asintoticamente ad un valore più basso. Si nota dunque un significativo discostamento tra i due approcci.
Allo scopo di valutare l'energia ottenibile da un sistema KiteGen, è necessario conoscere la funzione di densità di probabilità del vento per una data località a diverse quote dal terreno. Per realizzarle, si è fatto ricorso al database RAOB (Rawinsonde Observations) della National Oceanographic and Atmospheric Administration (NOAA), un database di misurazioni del vento ad alta quota realizzate per mezzo di palloni aerostatici. In particolare, si è fatto riferimento al sito di De Bilt, nei Paesi Bassi.
Si è trovato che, per la specifica località di De Bilt, il valore massimo della produzione energetica annua (AEP) ottenibile viene raggiunto con funi lunghe $500m$, un valore per il quale sia l'approccio delle funi rigide che quello delle funi flessibili danno lo stesso valore della resistenza aerodinamica e quindi di AEP. Per funi più lunghe di $500m$, invece, il valore della produzione energetica annua inizia a diminuire. Tuttavia, a partire da una lunghezza delle funi di circa $900m$, la differenza nella valutazione della AEP ottenuta utilizzando i due diversi approcci diventa significativamente evidente.
E' quindi emersa la necessità di studi più profondi sulla dinamica delle funi dal momento che ci sono ancora fenomeni fisici che sono stati ignorati in questo lavoro e che potrebbero portare a una ulteriore riduzione della resistenza aerodinamica delle funi ed eventualmente ad una differente valutazione dell'andamento della curva di produzione energetica annua in funzione della lunghezza delle funi.
In particolare, per futuri lavori, i principali fenomeni da aggiungere alla presente analisi sono: l'elasticità delle funi, la velocità di propagazione finita degli impulsi che il moto del kite manda alle funi e l'attrito interno delle funi. Inoltre, dovrebbe essere considerata anche la possibilità di adottare funi speciali con ridotto valore del coefficiente di attrito aerodinamico.

Acknowledgements

The present work has been realized with the collaboration of KiteGen Research. In particular, I would like to thank Engr. Massimo Ippolito and Engr. Eugenio Saraceno for their explanations, which have been essential for the understanding of a KiteGen system.

I would like then to thank my Supervisor, Prof. Daniela Tordella, for her precious suggestions and the time she dedicated to me.

A special thank goes to Prof. Giancarlo Abbate of Università degli Studi di Napoli Federico II for his constant support during the whole period of this work. In particular, I would like to thank him and Prof. Addolorata Marasco of Università degli Studi di Napoli Federico II for having provided to me a preliminary version of the system of equations used in Section 4.2.

Summary

List of Symbols

P_w: wind power available in a certain area A_d
$\dot{m}_a$: air mass flow
V_w: wind speed
A_d: area of an idealized actuator disc
C_P: wind turbine power coefficient
PD: wind power density
ψ: control angle
Δl: difference in length of the two lines
b: distance between the two lines fixing points at the kite
(x, y, z): global Cartesian coordinate system
(r, ϑ, ϕ): spherical coordinate system
r: distance from the origin
ϑ: polar angle: angle from the vertical
ϕ: azimuth angle
$(\bar{e}_\vartheta, \bar{e}_\phi, \bar{e}_r)$: local coordinate system, centered in the kite center of gravity
F_ϑ: projection on the $\bar{e}_\vartheta$ direction of the global force acting on the kite
F_ϕ: projection on the $\bar{e}_\phi$ direction of the global force acting on the kite
F_r: projection on the $\bar{e}_r$ direction of the global force acting on the kite
m: mass of the kite
$\bar{F}^{grav}$: gravity force of the kite and the lines
$\bar{F}^{app}$: apparent forces
$\bar{F}^{aer}$: kite aerodynamic forces
$\bar{F}_t$: aerodynamic drag force of one cable
$\bar{F}^{c,trac}$: traction force generated on one cables
F_ϑ^{gra}: projection on the $\bar{e}_\vartheta$ direction of the gravity force
F_ϕ^{gra}: projection on the $\bar{e}_\phi$ direction of the gravity force
F_r^{gra}: projection on the $\bar{e}_r$ direction of the gravity force
F_ϑ^{aer}: projection on the $\bar{e}_\vartheta$ direction of the kite aerodynamic forces
F_ϕ^{aer}: projection on the $\bar{e}_\phi$ direction of the kite aerodynamic forces
F_r^{aer}: projection on the $\bar{e}_r$ direction of the kite aerodynamic forces
$D_{c,\vartheta}$: projection on the $\bar{e}_\vartheta$ direction of the aerodynamic drag force of the cables
$D_{c,\phi}$: projection on the $\bar{e}_\phi$ direction of the aerodynamic drag force of the cables
$D_{c,r}$: projection on the $\bar{e}_r$ direction of the aerodynamic drag force of the cables
ρ_c: density of the cable
d_c: cable diameter
g: gravitational acceleration
$\bar{V}_e$: effective wind speed
$\bar{V}_{kite}$: flying velocity of the kite with respect to the ground
$\bar{V}_L$: radial component of $\bar{V}_{kite}$, i.e. reel-out velocity of the cables

$\bar{V}_k$: tangential (crosswind) component of $\bar{V}_{kite}$
$(\bar{x}_w, \bar{y}_w, \bar{z}_w)$: wind coordinate system
$\bar{D}_k$: kite drag force
$\bar{L}$: kite lift force
C_d: kite drag coefficient
C_l: kite lift coefficient
A: kite reference area
ρ: air density
α: kite angle of attack
$(\bar{x}_b, \bar{y}_b, \bar{z}_b)$: kite body coordinate system
α_0: base angle of attack
$\Delta\alpha$: difference between α and α_0
$\bar{e}_r$: unit vector identifying the kite line direction
E: kite aerodynamic efficiency, i.e. C_l/C_d
Δs: length of a discretized piece of rope
$\bar{F}_{t,\Delta s}$: drag force acting on a discretized piece of rope Δs
$\bar{M}_d$: angular momentum acting on the rope given by $\bar{F}_t$
s: curvilinear abscissa, i.e. position along the rope
$\bar{e}_n$: unit vector normal to the cable surface
V_n: component of the cable effective velocity normal to the cable surface
$C_{d,c}$: cable drag coefficient
G_e: aerodynamic efficiency of the global system
d_c: cable diameter
A_c: cable cross area, i.e. $A_c = r\, d_c$
$\bar{V}_e$: effective wind velocity
$\bar{V}_{e,p}$: projection of the effective wind speed $\bar{V}_e$ on the plane perpendicular to the unit vector $\bar{e}_r$ (and formed by the unit vectors $\bar{e}_\vartheta$ and $\bar{e}_\phi$)
$\bar{e}_w$: unit vector identifying the crosswind direction, i.e. $\bar{e}_w = \frac{\bar{V}_{e,p}}{|\bar{V}_{e,p}|}$
D_c: overall drag force of the cables
F_w^{gra}: projection of the gravity force on $\bar{e}_w$ direction
F_k: global traction force generated from the kite on the cables
P: generated power
V_0: wind speed at the altitude z_0
α_p: roughness coefficient in the power law
z_r: roughness coefficient in the logarithmic law
μ: linear density of the rope, i.e. mass/length
$\bar{a}$: acceleration
$\bar{w}$: weight of the rope per unit length
$\bar{W}$: weight of the rope
$\bar{f}_t$: aerodynamic drag force of one cable per unit length
$\bar{T}$: variable tension along the rope
$V_{L,x}$: component on the x direction of V_L

$V_{L,y}$: component on the y direction of V_L
$V_{L,z}$: component on the z direction of V_L
t_0: initial time
t: time
T_0: tension of one rope at the drum
T_1: tension of one rope at the kite
X_v: x component of V_e, i.e. $\frac{\partial x}{\partial t}$
Y_v: y component of V_e, i.e. $\frac{\partial y}{\partial t}$
Z_v: z component of V_e, i.e. $\frac{\partial z}{\partial t}$
Δt: time step
ω: coefficient of the Successive Over-Relaxation (SOR) method
AEP: annual energy production
$\bar{\tau}$: tangential unit vector along the line element
$\Delta\beta$: angle between the direction of $\bar{\tau}$ and the direction normal to $\bar{V}_e$

1. Introduction

1.1 Climate changes

In the last years, there has been an increasing awareness on climate changes. As mentioned by IPCC (Intergovernamental Panel on Climate Change) in its annual report (see [1]), from 1880 to 2012 the globally averaged combined land and ocean surface temperature has grown of 0.85 °C. Moreover, the surface temperature of the last three decades has been successively higher than any previous decade since 1850 and it is likely that the whole period has been the warmest 30-year period of the last 1400 years in the Northern Hemisphere. Because of the higher temperatures, the amounts of ice and snow across the world have diminished and the sea level is rising.

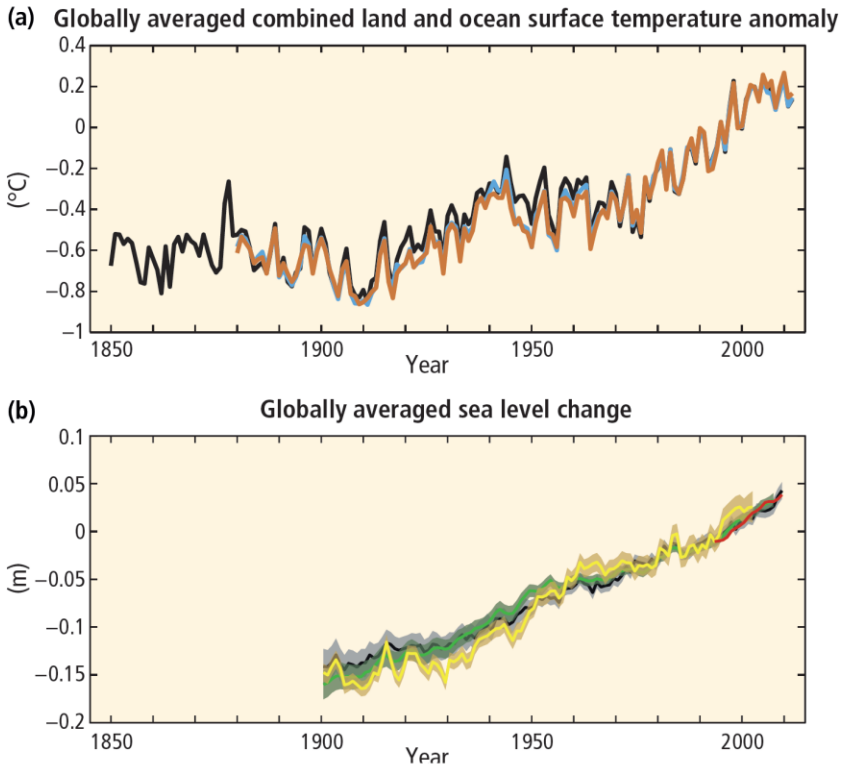

Fig. 1.1: (a) Globally averaged combined land and ocean surface temperature deviation with respect to the average temperature over the period 1986 to 2005. Different colors indicate different data sets. (b) Globally averaged sea level deviation with respect to the average level over the period 1986 to 2005. Different colors indicate different data sets. Source [1].

Climate changes have strong impacts on natural systems. Because of the changes in precipitations and the melting of snow and ice, the hydrological systems are being altered, affecting therefore the water availability. Some species have changed their geographic

ranges and migration patterns and their abundance is varied. The human system has also been touched, for instance with worse crop yields.

It is very likely that these unprecedented climate changes have an anthropogenic cause. In particular, they may find their origin in the extraordinary levels of carbon dioxide, methane and nitrous oxide, never been this high at least in the last 800 000 years [1]. The emission of these greenhouse gasses have strongly increase since the industrial era, as it can be seen in the next figures.

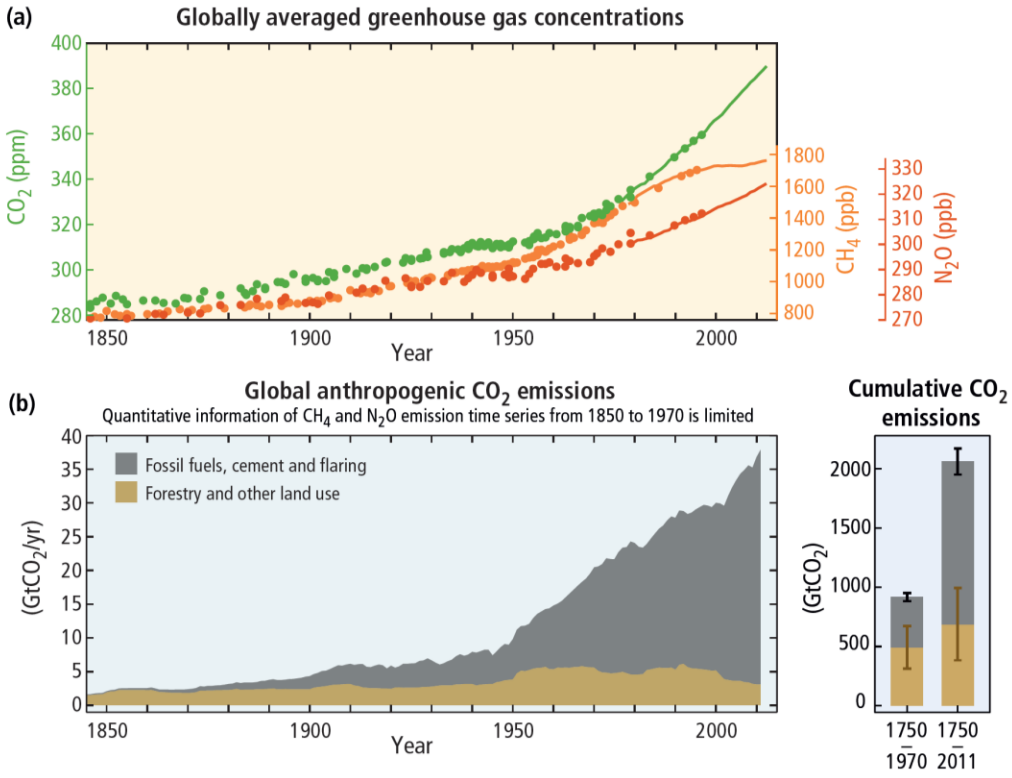

Fig. 1.2: (a) Concentrations in the atmosphere of CO2 (in green), methane (in orange) and nitrous oxide (in red) determined from ice core data (dots) and from direct atmospheric measurements (lines). (b) Global anthropogenic CO2 emissions from forestry and other land usage (in brown) and from burning of fossil fuel, cement production and flaring (in grey). On the right hand side instead there are the cumulative emissions of CO2 from the same sources (their uncertainties are shown as whiskers). Source [1].

1.2 Renewable Energy

In this context, the role of renewable energy becomes of primary importance. In 2013, according to the International Energy Agency (IEA), the percentage of primary energy supplied by fossil fuel was 81.4% [2].

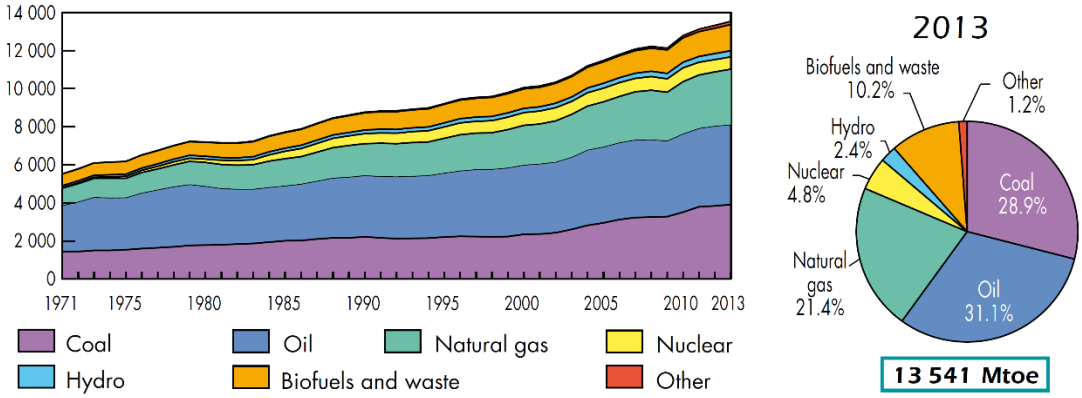

Fig. 1.3: World total primary energy supply by fuel (in Mtoe) from 1971 to 2013 and their percentage over the total primary energy supply in 2013. The term "Other" includes geothermal, solar, wind, etc. Source [2]

Focusing only on the electricity production, in 2013 the energy generated by fossil fuel amounts to the 67.4%, even with the yearly increase of the fraction of the global renewable-based power capacity additions over the total capacity additions, that in 2014 has reached the value of 45%.

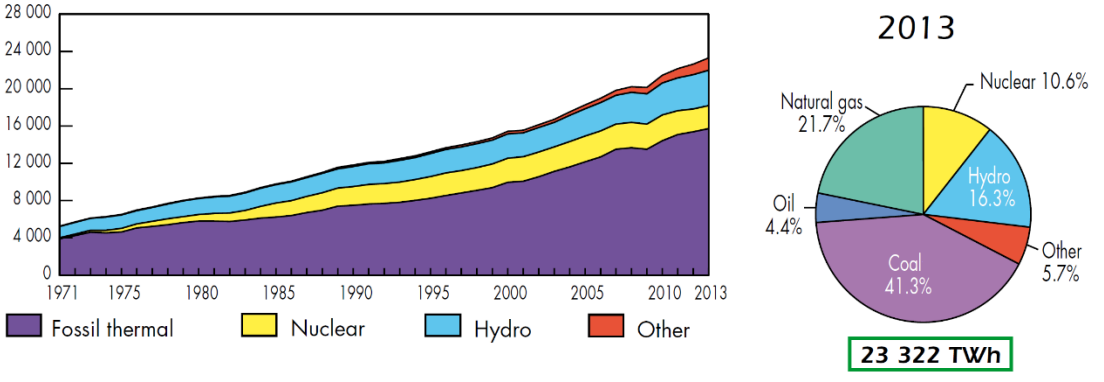

Fig. 1.4:World electricity production by fuel (in TWh) from 1971 to 2013 and their percentage over the total electricity production in 2013. The term "Other" includes geothermal, solar, wind, etc. Source [2]

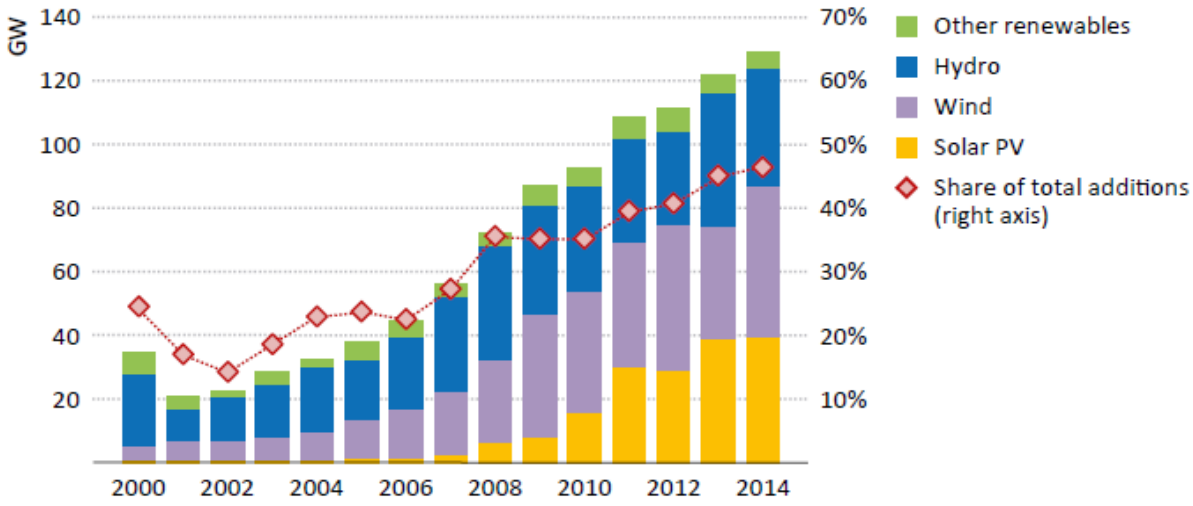

Fig. 1.5: Global renewables-based power capacity additions per year. On the left axis it is possible to read the capacity addition of each kind of renewable power source, while on the right axis it is possible to read the share of the global renewables-based power capacity additions over the total capacity additions. The term "Other renewables" includes geothermal, marine, bioenergy and concentrated solar power. Source [3].

These efforts, however, seem not to be enough to stop the climate changes. For this reason, energy has been the core of the discussion during the 21^{th} Conference of the Parties (COP21) held in Paris in December 2015. In order to avoid an increase of temperature of more than 1.5°C above the pre-industrial level, the Parties involved in the meeting have reached an historic deal. Even not describing in detail how the aim should be reached, the goal is to strongly minimize the emissions of CO_2 by 2030 and to push them to zero by 2050. In this context, it is evident the need for developing new renewable energy forms, more efficient than the existing ones and able to live even without the presence of national subsidies. In particular, in this thesis, the subject of the high altitude wind power generation will be explored, focusing on one of its more interesting and promising technology, KiteGen.

1.3 Wind Energy

Wind is a massive source of power, available in a kinetic form. As known, the Sun heats in different ways different places of the Earth. This phenomenon creates zones in which the air is warmer than in other and, since variation in temperature gives variation in density, in those places there will also be higher pressure. Wind is simply the way in which the atmospheric system tries to stabilize and reach both thermal and baric equilibrium.
The force of the wind has been used for centuries as propulsion for ships as well as in windmills to grind grain or to pump water for irrigation. When then, at the beginning of the 20^{th} century, electricity came into use, the windmills were gradually optimized and connected to an electric generator in order to produce electricity.
According to [4], the worldwide wind plants capacity reached $371\,559\,MW$ in 2014 and produced in the same year around 800 TWh of electric energy, accounting for approximately the 4% of the global electricity demand. The majority of this installed capacity is constituted by wind turbines with horizontal axis. These devices transform the kinetic energy of the wind in rotation of a rotor, obtaining therefore mechanical energy that is finally converted into electric energy in a generator. If a certain area A_d is considered, the kinetic power carried by a mass flow $\dot{m}$ can be expressed as:

$$P_w = \frac{1}{2}\,\dot{m}_a\,V_w^2 = \frac{1}{2}\,\rho\,A_d\,V_w^3 \qquad (1.1)$$

where ρ is the air density and V_w is the wind speed. However, not all of this available power can be converted in mechanical power and its maximum theoretical fraction that can be recovered is 0.593 [5], denoted as Betz limit and derived from the principles of conservation of mass and momentum of the air flow through an idealized actuator disc. The reason for this limit stands in the fact that if all the kinetic power of the incoming flow was exploited, then, after the rotor, the air would have velocity equal to zero and therefore would block the coming of new air. In particular, the maximum theoretical power is obtained when the velocity of the air afterward the rotor is 1/3 of the velocity of the incoming air. Modern optimized wind turbines can operate up to a value of 0.5 of this fraction (conventionally called power coefficient C_P).

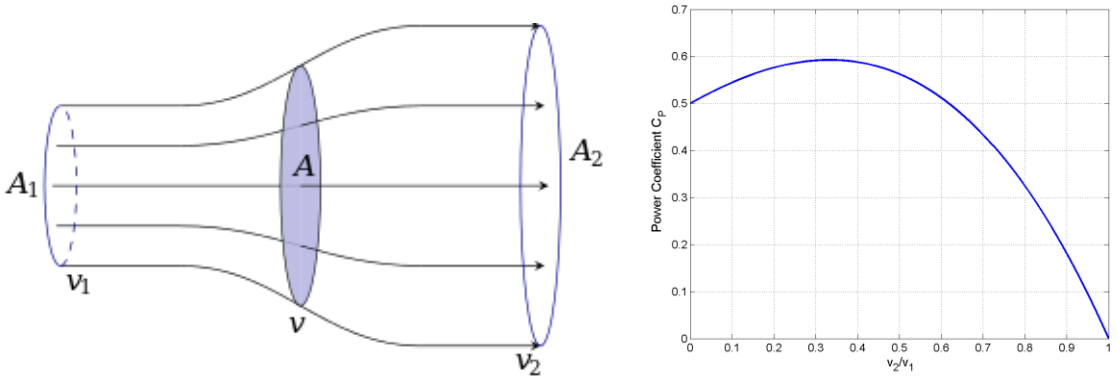

Fig. 1.6: Betz's airflow model (on the left) and power coefficient curve versus v_2/v_1 ratio (on the right) for an idealized actuator disc.

The actual wind technology exploits the wind at low altitude, usually in the range of $80 \div 120\ m$ height for big multi MW wind towers. The properties of the wind, however, change dramatically with the altitude. In particular, its velocity and occurrence grow significantly. On the other side, instead, the density of the air decrease with the altitude.

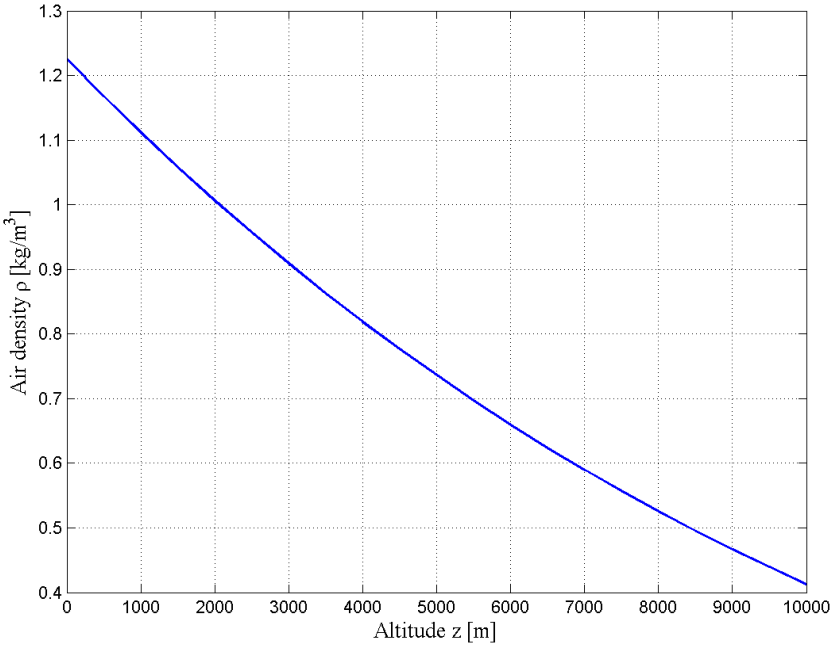

Fig. 1.7: Air density of the International Standard Atmosphere (ISA) as function of the altitude z. Data source [6].

Considering equation (1.1), however, it is clear that the velocity has a higher impact on the power carried by the wind than the density, since it appears in a cubic form and the density variations are not so big. Defining, indeed, the wind power density PD as the power carried by the wind per unit area, $PD = \frac{1}{2}\rho\, V_w^3$, it is possible to see from the data in [7] that the power density increases considerably if high altitude are considered.

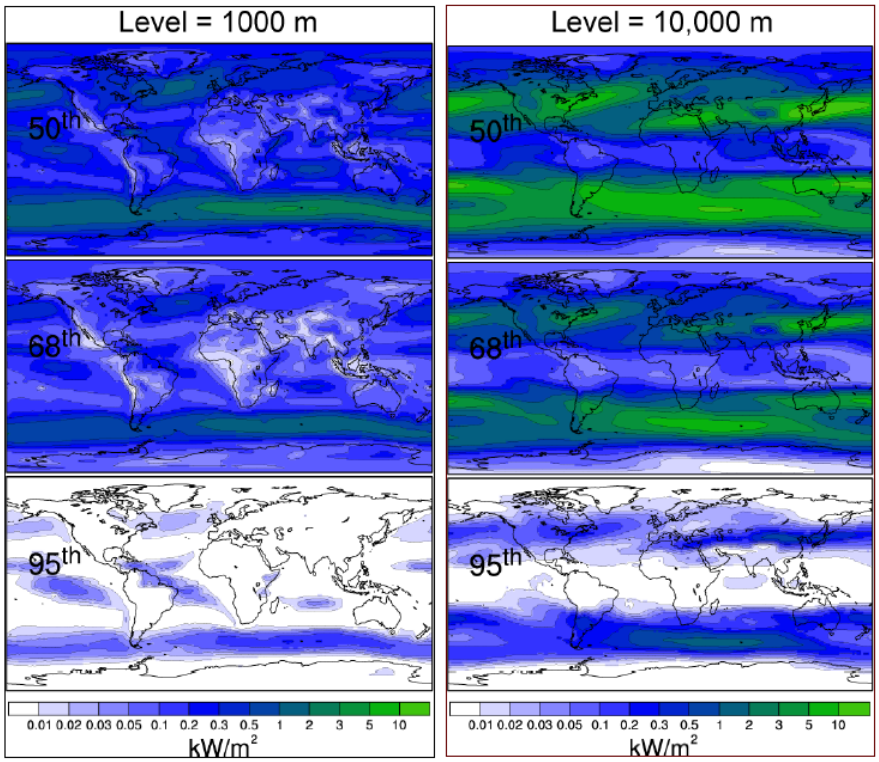

Fig. 1.8: Wind power density $[kW/m^2]$ that was exceeded for 50%, 68% and 95% of the time during the years 1979-2006 at 1000m and 10000m of altitude all over the world. Source [7].

This is the reason why, in the past years, a lot of interest has been put in designing devices able to harvest wind at high altitude. Moreover, the occurrence of the wind increases at high altitude and this allows these machines to operate more time during the year and therefore to obtain more energy.

1.4 High-Altitude Wind Technology

There are several systems, based on deeply different working principles, which try to harness high altitude wind for power production. In this section, a small overview of the different concepts will be presented, before focusing more in detail in the rest of the work on a particular system, the KiteGen Stem device.

In general, an high altitude wind energy system is composed by one or more aircrafts, an electrical generator and one or more ropes connecting the aircraft to the ground. The first classification that can be done is between *Ground-Gen* systems and *Fly-Gen* systems [8], depending on whether the conversion of mechanical energy into electrical energy takes place on the ground or on the aircraft.

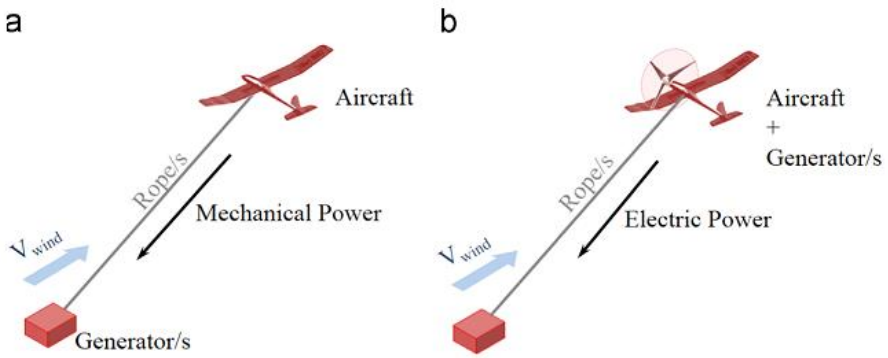

Fig. 1.9: Basic concept of Ground-Gen (a) and Fly-Gen (b) high altitude wind energy system. Source [8].

1.4.1 Ground-Gen systems

In Ground-Gen systems, the purpose is to exploit the aerodynamic forces generated on the aircraft from the action of the wind to produce traction force on the ropes connecting the aircraft to ground. These systems can be then distinguished in fixed-ground-station devices and moving-ground-station devices.

1.4.1.1 Fixed-Ground-Gen systems

In fixed-ground-station, the aircraft performs a two-phases cycle: a traction phase and a recovery phase. During the traction phase, the aircraft is driven in such a way to maximize the lift and therefore the traction force generated on the ropes. This traction force is then used to induce rotation of the electrical generators. During the recovery phase, instead, the ropes are wound back to the drums and the aircraft is brought to its original position at the beginning of the traction phase. In the recovery phase, therefore, it is needed to consume energy but this consumption is minimized by suitably controlling the aerodynamic characteristics of the aircraft. Thanks to this operation, it is possible to have positive net energy generation during the entire cycle. Because of the discontinuity in the power output, batteries or large capacitors are needed, even though a farm of these devices would minimize this need.
In the following, the most important projects dealing with Fixed-Ground-Gen systems will be presented.

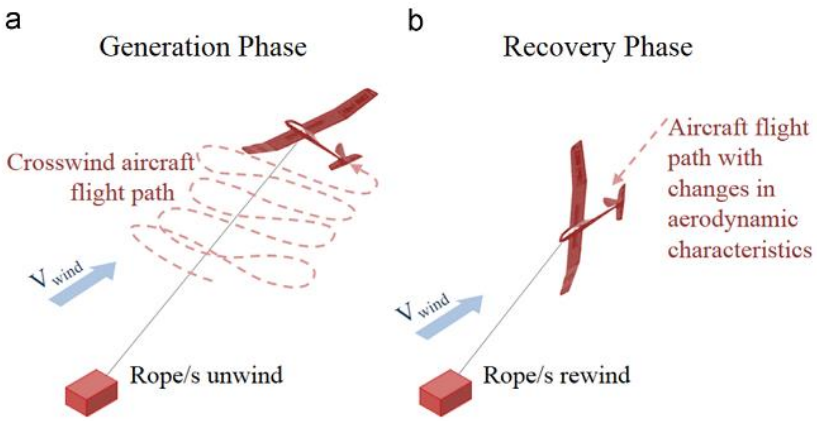

Fig. 1.10: Working principle of a two-phases Ground-Gen high altitude-wind power system. Source [8].

1.4.1.1.1 KiteGen Research

KiteGen Research is one of the leader companies of the sector and one of the first to test a working prototype of Ground-Gen system [9]. With some of its competitors, KiteGen Research has been included from the National Geographic among the "8 Tech Breakthroughs of 2015 That Could Help Power the World" [10]. Moreover, it has also been included in the "100 ones to watch list" of 2015 of Cleantech Group, a list of the top 100 private innovation companies in clean technology [11], and has been identified from the Italian Council of Innovation as the Italian company with the highest number of patents in the Renewable Energy Generation sector [12].

The company is currently working on the development of the so-called KiteGen Stem system, with nominal power of 3MW. This system, which will be better described in the following and is the subject of this work, is based on a semi-rigid wing, two ropes, the ground generator and a flexible rod $20m$ long connected to the control station. The functions of the stem, in which the ropes pass through, are to support and hold the kite when the device is not working and to damp the peak forces in the ropes due to sudden wind-gusts [8].

Fig. 1.11: Semi-rigid wing of the 3MW high altitude wind power plant of KiteGen Research.

1.4.1.1.2 SkySails Power

SkySails is a german company which has two divisions based on the kite technology. The first division, called SkySails Marine, is leader in the field of kite wind propulsion systems for ships. The second division, called instead SkySails Power, is developing a Ground-Gen high altitude wind energy system based on the same technology already used for the marine propulsion. The SkySails Power's technology is based on a foil kite flying at altitudes between 200 and 800 meters. The company has already realized a working prototype of 55 kW and is currently developing offshore systems with power output from 1 MW to 3.5 MW. The main difference between this technology and the Kitegen Research's technology is that in this case there is only one rope connecting the ground station to a control pod, an electrical device from which then start the bridles connected to the kite. The flight of the kite can be therefore controlled from the control pod by altering the lengths of the kite bridles. Finally, in the rope, there are electric cables whose functions are to communicate with the control pod and to provide the power needed for its work.

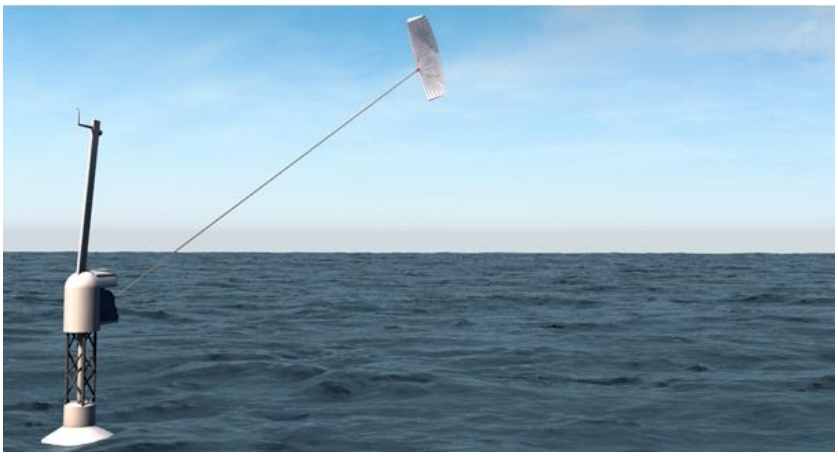

Fig. 1.12: Graphical rapresentation of a SkySails' power plant. Source [13].

1.4.1.1.3 Twing Tech

Twing Tech is a Swiss which has developed a containerized mobile wind energy system of 100kW of rated power, expressly thought for areas hard to reach. It is based on a glider which is integrated with small propellers to perform the launch and landing, making the system completely autonomous.

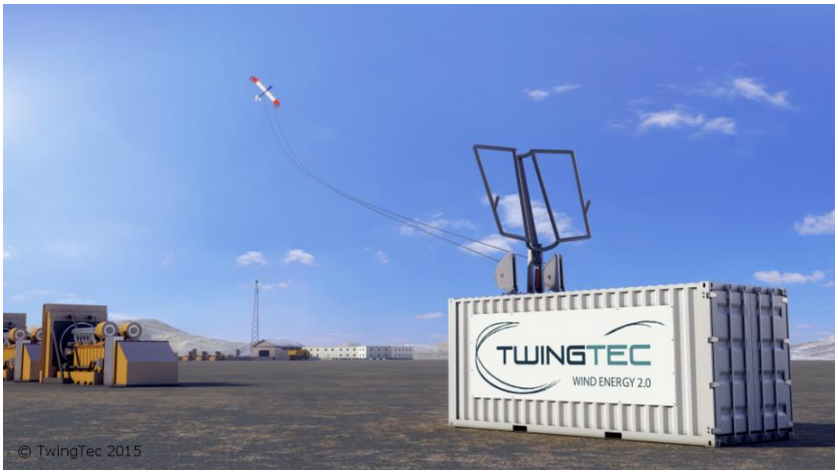

Fig. 1.13: Twing Tech 100kW system. Source [14]

1.4.1.1.4 TU Delft

The University of Technology of Delft has been among the first organizations to operate in this field. Their first research started in 1996 [8]. The technology of TU Delft is based on a kite connected with only one rope to the generator. The flight control is operated with a control pod, which is also able to control the angle of attack of the system according to the needs of the active and passive phase. In 2012, their 20kW prototype, based on an inflatable wing of 25 m^2, has demonstrated the capability of fully automated operation [15].

Fig. 1.14: TU Delft prototype. The control-pod is visible. Source [16].

1.4.1.1.5 EnerKite

EnerKite is a German company whose aircraft does not have on-board sensors and is controlled from the ground by means of three ropes. A system for autonomous launch and landing for semi-rigid wings is under development. The company has already a prototype of 30kW and is planning to produce a 100kW and 500kW system.

1.4.1.1.6 Kitenergy

Kitenergy is an Italian company whose system is based on a foil kite and two ropes. Their prototype reaches the 60kW of rated power. Another their prototype has reached 4 hours of autonomous flight without power production in 2012 [8].

1.4.1.1.7 Ampyx Power

The technology of Ampyx Power is based on glider instead that on a wing. Their 50kW prototype is able to automatically perform the launch, the pumping phase and the landing. Both the launch and the landing are performed in a way similar to that of an airplane. At the launch the glider is positioned at some meters of distance from the ground station, then the cables are reeled-in and the glider starts to move on the ground: when the lift force is strong enough the glider starts to fly. The company is now planning to scale up the system in order to reach 2MW of rated power.

1.4.1.2 Moving-Ground-Gen Systems

As the name suggests, in Moving-Ground-Gen systems the ground station is not fixed on the ground. This field is still object of study, therefore still no working prototype has been realized, but, nevertheless, there is certain number of patents on this subject. The main advantage of these systems is the possible continuous power production. In the following, the main projects dealing with Moving-Ground-Gen systems are summarized.

1.4.1.2.1 KiteGen Research

The so-called KiteGen Carousel is a system composed by a vertical axis generator connected with a great ring to several KiteGen Stem machines. Each kite is controlled in such a way to keep the traction force on its ropes constant, while the length of the ropes is varied in order

to obtain the optimal trajectories for the energy generation. As the kites move in the air, induce a torque on the rotating frame and finally torque and rotation are converted into electrical power by the generators. According to the company, a 1GW plant can be reached using a diameter of approximately $1600m$ [17].

Fig. 1.15: Graphical representation of the KiteGen Carousel concept. Source [18].

1.4.1.2.2 NTS Energie

Another concept is based on ground stations which are moving on closed track circuits being pulled from a kite. The concept has been proposed by KiteGen Research and NTS Energie und Transportsysteme [8]. In particular, NTS has tested a prototype composed from a kite and a ground station mounted on a vehicle moving on a $400m$ long straight track. During the test, kites with area up to $40m^2$ were tested, obtaining 1 kW of power per m^2 of kite.

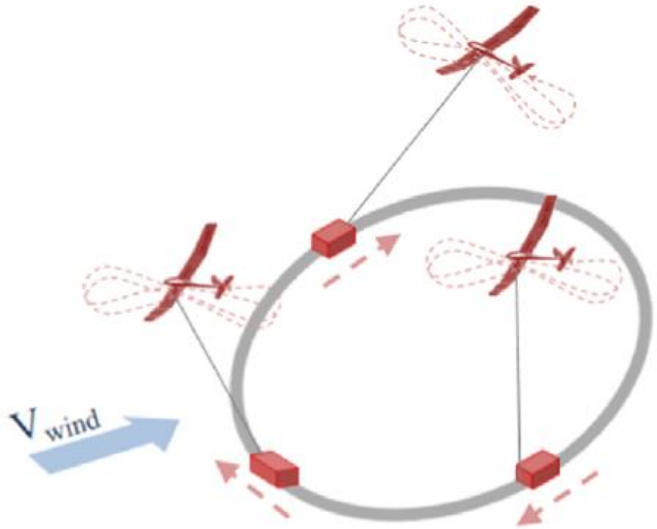

Fig. 1.16: Graphical representation of system based on moving vehicles as ground stations. Source [8].

1.4.1.2.3 Kitenergy

The concept developed by Kitenergy is composed by a straight rail track able to rotate on a joint. The rail direction is set in such a way to be normal to the wind direction. On the rail there is a wheeled vehicle which moves from one side to the other of the track being pulled from a kite. Electrical power is generated by means of electromagnetic rotational generators on the wheels of the vehicle or by means of linear electromagnetic generators on the rail. Because of the inversion of the motion at the end of the track, the system doesn't provide a fully continuous power generation.

1.4.2 Fly-Gen system

In a Fly-Gen system, the production of electric power takes place onboard of the aircraft. The rope connecting the aircraft to the ground, therefore, is also provided of a electric cables in order to transmit the electric power to the ground. In the following, the main projects involving Fly-Gen systems are shown.

1.4.2.1 Makani Power

Makani Power is among the most important companies for the high-altitude wind power generation and in 2013 has been acquired by Google. Its technology is based on an Airborne Wind Turbine, an airborne provided with several rotors that can act like propellers or like generators according to the need. During the take-off maneuver, the propellers lift the airborne, which in this phase is vertical position, up until the desired elevation. At this point, the propellers stop to work and the airborne starts to perform a circular trajectory possible thanks to the wing lift. During this phase, the rotors operate as generators, producing electrical power. The idea behind this operation is to simulate the operations of the tip of a wind turbine, which is the part of the turbine which generates the most of the power. For the landing operation, instead, the airborne comes back in a vertical position and is driven to the ground station from the rotors, which come back to work as propellers. The first fully automated prototype produced by Makani Power was $8m$ long and with rated power of $20kW$. The company is now developing a $600\ kW$ system, provided of 8 rotors onboard and able to work at the full rated power with $11.5\ m/s$ of wind [19].

Fig. 1.17: Example of one of the Makani Power's airborne. Source [20].

1.4.2.2 Joby Energy

The technology that Joby Energy is developing is very similar to the one of Makani Power. In this case, however, a special structures is used to support an array of rotors. These rotors, like in the Makani technology, are used as propellers during the take-off and landing operations, and as generators during the crosswind flight.

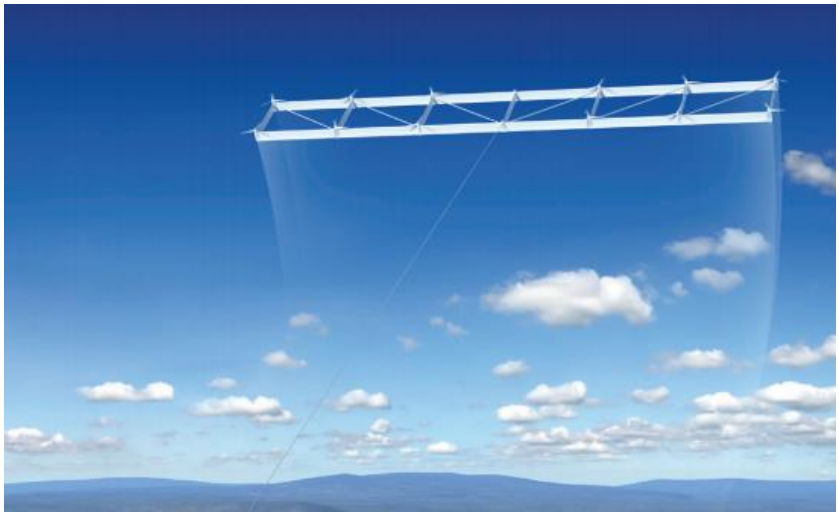

Fig. 1.18: Illustration of a Joby Energy system. Source [21].

1.4.2.3 Altaeros Energies

Altaeros Energies' technology is based on a flying wind turbine kept at high altitude thanks to a special ring shaped aerostat. The system is provided of a flight control system which allows the system to automatically ascent, operate at high altitude, descend and secure on its ground station during severe weather.

Fig. 1.19: Altaeros' Airborne wind technology. Source [22].

1.5 Contribution of this Thesis and its structure

As already mentioned, in this thesis the main topic is the study of the working principles of a particular type of high altitude wind energy generator, the KiteGen Stem. In particular, the focus of this work will be on the estimation of the aerodynamic resistance of the cables connecting the ground station to the kite. As it will be seen, indeed, the evaluation of this drag force is of primary importance since it affects the energy output of the whole system.
The computing of the aerodynamic resistance will be performed using two different approaches. In the first approach, most widely used in the scientific literature, the ropes will be considered as straight rigid lines. This assumption has the implication of having the velocity with which each piece of the ropes moves in the air linearly decreasing from the velocity at which the kite flies to zero at the ground, so for instance if the kite flies at $80\ m/s$ the rope velocity will be linearly decreasing from $80\ m/s$ to $0\ m/s$. Moreover this approach doesn't take into consideration the effective kite trajectory during the flight. The second approach, which instead is the main contribution of this work, consists in not pre-assigning the rope configuration, therefore considering it as flexible. Its position is found solving a dynamic system which takes into account the main forces acting on the rope while the kite is flying performing an eight-shaped trajectory, which is typical for these systems.
The need for this study has emerged due to experimental observations during the operations of these systems. It has been noticed, indeed, that the behavior of each rope strongly differs from that of a straight line, but instead it tends to curve and to follow the kite flight mostly only with the highest part of the rope, while the remaining part tends to stay quieter close to the axis of the trajectory performed by the kite. This behavior will affect the flying velocity of each piece of the rope and therefore the evaluation of the aerodynamic drag force of the cables. This fact has a dramatic implication on the evaluation of the energy obtainable with these devices as it will be shown.

The remaining part of the thesis is organized as follows. In Chapter 2, the KiteGen technology is presented, including also the dynamic model of the system and the KiteGen characteristic curves. In Chapter 3 the wind model is presented. In Chapter 4 the estimation of the cables aerodynamic drag force is performed. In Chapter 5, the global system power curves and the annual energy production are evaluated. In last Chapter presents the conclusions of this thesis with the main results and possible future works.

2. KiteGen technology

2.1 KiteGen Stem working principles

In order to understand the concept of the KiteGen technology, it is important to know firstly how in conventional wind turbines the wind is harvested. About 80% of the power extracted from the wind is produced by the 20% outer part of the blades. This is due to the fact that the tips of the blades have higher tangential velocity and the generated power is proportional to the cube of the effective wind velocity. The remaining 80% of the blades produces only a little fraction of the power, while the tower is not an active part in the energy production. On the other side, the tower determines most of the cost of the device and does not allow to reach very high altitude because of structural limits.
In the KiteGen project, the outer part of the blades is substituted by a kite, while all the remaining part of the structure is substituted only by two cables in with very high tensile strength. These cables are linked to drums connected with two electric drives which can operate both as generator and motor according to the needs. The kite flight is controlled by electronic devices both on the kite (whose power is provided by a micro turbine set on the kite) and at the ground. The electric drives, the drums, the sensors and the hardware used to control the kite compose a system called Kite Steering Unit (KSU). Because of the less material needed, the entire device becomes much lighter and cheaper than a wind turbine. Moreover, since it is like using only the outer (more efficient) part of the wind turbine rotor, this system is characterized by an higher power output per wing surface area.

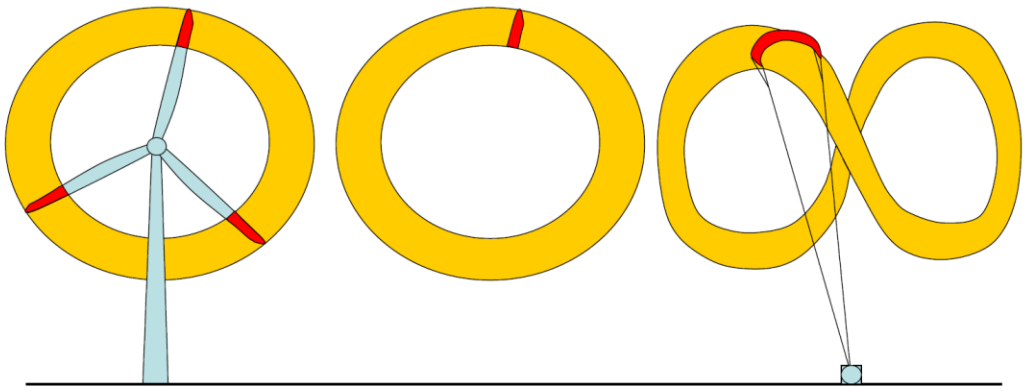

Fig. 2.1: Schematic representation of the basic concept of a KiteGen system. Source [23].

2.1.1 Wind Window and Power Zone

The wind window is defined as the portion of the sky in which the kite is able to fly. It roughly coincides with the area that an observer can see when facing downwind. The back of the window is determined by the length of the kite lines, while the edge of the wind window is defined as the portion of the sky after which the kite cannot longer fly forward toward the observer.

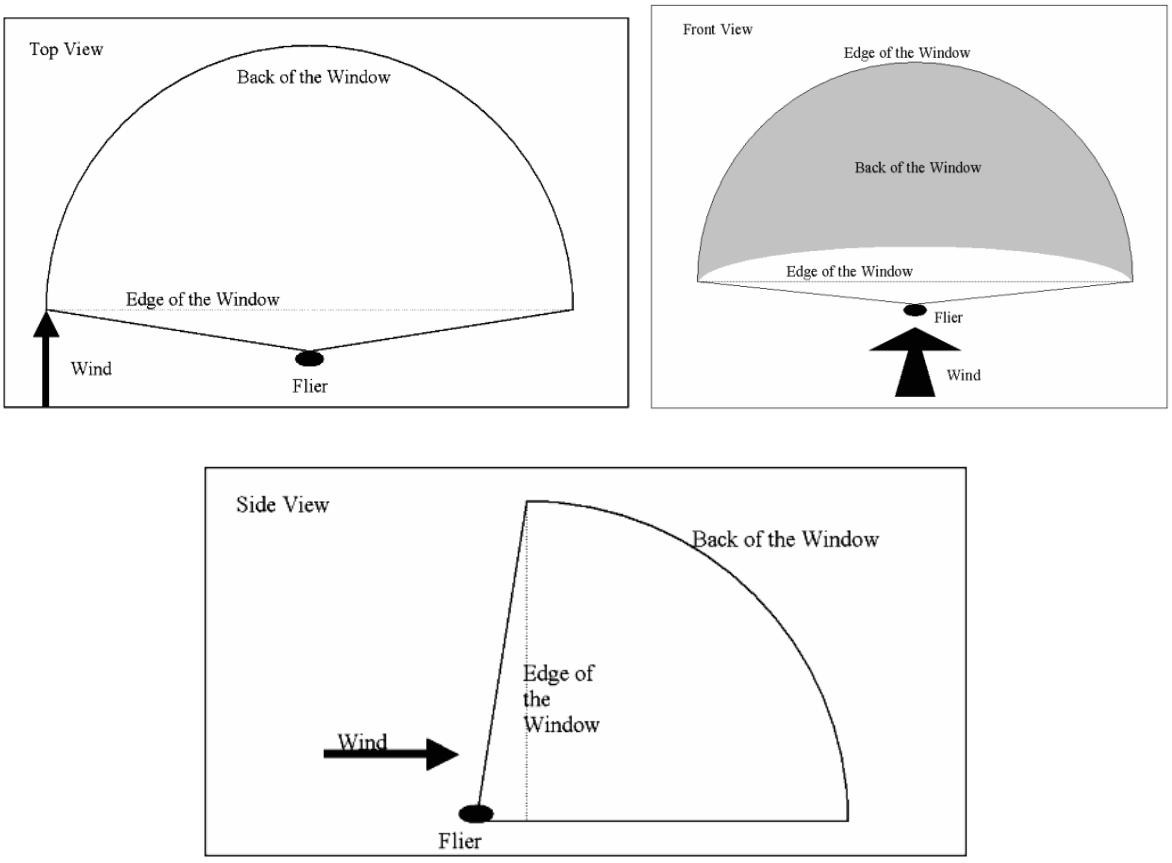

Fig. 2.2: Wind window from different points of view. Source picture [24]

The portion of the wind window that is directly downwind is usually called Power Zone. From the kitesurfing it is well known, indeed, that flying in transverse direction (crosswind) in this portion of the wind window, allows the kite to fly fast and to obtain maximum power from the wind.

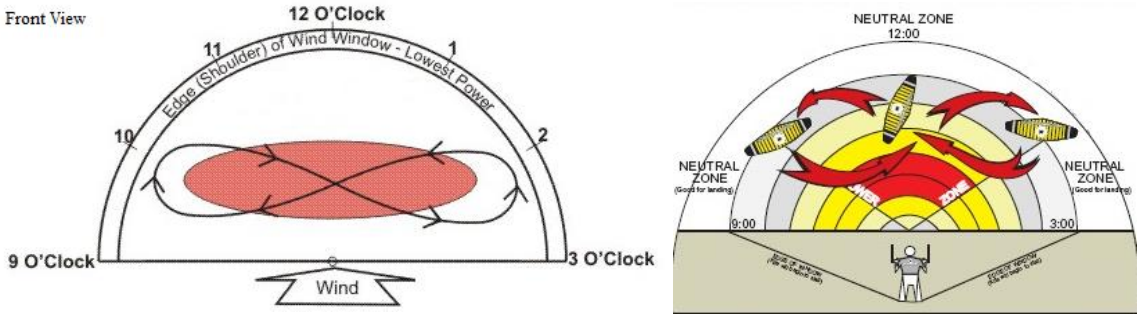

Fig. 2.3: Transverse flight through the power zone (highlighted in red). Note the clock-based notation common in kitesurfing. Picture on the left based on picture from [25], while picture on the right is taken from [26].

The edge of the wind, instead, is where the least power can be obtained, while, in between of these two zones, there is a zone of intermediate power.

2.1.2 KiteGen *yo-yo* configuration

As already mentioned in the introduction, one possible utilization of the kite technology is with the two phases cycle, often called *yo-yo configuration*. In this configuration, the kite performs a *traction phase* and a *passive phase*. During the traction phase, the kite is controlled in such a way to make it fly approximately in crosswind direction, which allows to maximize the energy generation. During this phase, the kite describes eight-shaped trajectories and reels out the lines from the drums, making the electric drives work as generators. The passive phase starts when the maximum line length is reached and therefore the electric drives start to work as motors since it is needed to roll again the cables over the drums in order to start a new traction phase. The recovery operation may be performed with two different procedures [23]: *low power maneuver* and *wing glide maneuver* or *side-slip*. In the low power maneuver, the kite is driven by the KSU to the borders of the power zone in order to make the aerodynamic lift decrease and making it possible to recover the kite with low energy consumption. In the side-slip, instead, a big length difference between the two cables is induced, making the kite stall. In this way, the aerodynamic lift will drop down and it is possible to quickly recover the cables with low energy consumption as the kite precipitates. The second procedure, chosen by KiteGen Research, allows to minimize the energy consumption and the aerial space needed during the recovery phase and in order to perform it, a flexible foil kite or a semi-rigid wing is needed. For this reason, the new power wing realized by KiteGen Research is made of several rigid pieces linked together with flexible joints. A video showing this procedure with a flexible wing can be found in [27].
In order to make the system efficient, the energy spent in the passive phase has to be a small fraction of the energy generated during the traction phase.

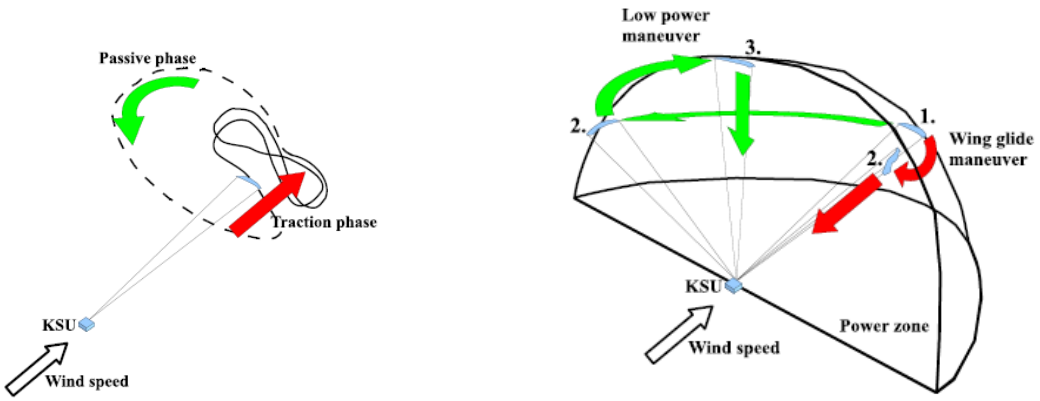

Fig. 2.4: On the left: graphical representation of a (reduced) traction phase and of a passive phase. On the right: possible passive phase operations. Source for both pictures [23].

As it may be noticed, control is a key point in this technology. In particular, the kite flight can be controlled by differentially controlling the reel-out speed or reel-in speed of the two ropes. The control input is the angle ψ, where:

$$\psi = \arcsin\left(\frac{\Delta l}{b}\right) \qquad (2.1)$$

being Δl the difference in length of the two lines and b the distance between the two lines fixing points at the kite.

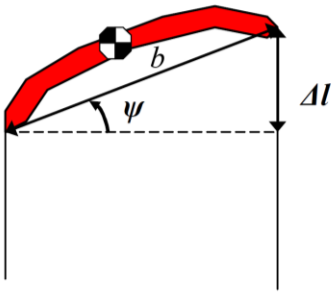

Fig. 2.5: Control angle ψ, obtained through a differential pulling of the lines. Picture source [23].

During the past years, several approaches have been used in this field to derive suitable kinds of control, such as a "fast" implementation of Nonlinear Model Predictive Control [9] or a Direct Data-Driven Inverse Control [28]. The detailed description of these approaches goes beyond the purposes of this thesis. It is important to know, however, that the control unit performs continuously an optimization procedure to find the best value of the angle of attack, kite flight direction and reel out velocity in order to obtain the maximum possible power. The eight-shaped trajectory, for instance, is not preassigned but is the result of this optimization procedure.

2.2 KiteGen Dynamic Model

In this section, the dynamic model of a KiteGen system is presented. In particular the approach of [29] will be followed. In order to describe the physics behind the dynamic behavior of a KiteGen system, several coordinate systems are needed. The first one is a global Cartesian coordinate system (x, y, z). It is supposed that the wind velocity vector $\bar{V}_W$ is aligned with the x axis and has intensity function of the altitude z:

$$\bar{V}_W = \begin{pmatrix} V_W(z) \\ 0 \\ 0 \end{pmatrix} \qquad (2.2)$$

The trend of the function $V_W(z)$ may be evaluated for several locations using the database RAOB (Radiosonde Observation) of the National Oceanographic and Atmospheric Administration (NOAA), an american federal agency focused on the condition of the oceans and the atmosphere. In particular, for this thesis, the wind data for the location of De Bilt have been analyzed. The details about the wind model will be discussed in the next paragraph.

The kite position may also be expressed using a spherical coordinate system by means of the distance r from the origin, the polar angle ϑ and the azimuth angle ϕ. In particular, the polar angle ϑ is defined as the angle between the vertical axis z and the kite position, while the the azimuth angle ϕ is defined as the angle with the absolute wind direction. The third coordinate system introduced is the local coordinate system which is centered in the kite center of gravity and has as unit vectors $(\bar{e}_\vartheta, \bar{e}_\phi, \bar{e}_r)$. In particular, the local unit vectors $(\bar{e}_\vartheta, \bar{e}_\phi, \bar{e}_r)$ can be expressed in the global Cartesian system (x, y, z) as:

$$\left(\bar{e}_\vartheta, \bar{e}_\phi, \bar{e}_r\right) = \begin{pmatrix} \cos(\vartheta)\cos(\phi) & -\sin(\phi) & \sin(\vartheta)\cos(\phi) \\ \cos(\vartheta)\sin(\phi) & \cos(\phi) & \sin(\vartheta)\sin(\phi) \\ -\sin(\vartheta) & 0 & \cos(\vartheta) \end{pmatrix} \qquad (2.3)$$

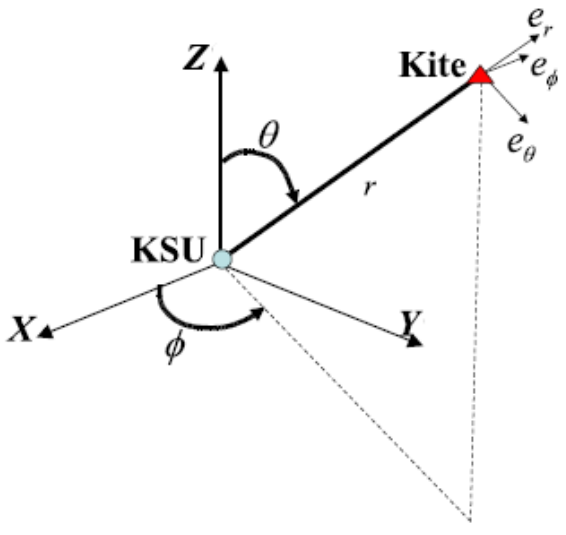

Fig. 2.6: Global and local coordinate systems. Source [23].

Applying the Newton's law of motion to the kite in the frame of the local coordinate system, the following equations are obtained:

$$\ddot{\theta} = \frac{F_{\vartheta}}{m\, r} \qquad (2.4)$$

$$\ddot{\phi} = \frac{F_{\phi}}{m\, r\, sin\theta} \qquad (2.5)$$

$$\ddot{r} = \frac{F_r}{m} \qquad (2.6)$$

where m is the mass of the kite. The forces on the right side of the previous equations are given by the gravity force $\bar{F}^{grav}$ of the kite and the lines, the apparent forces $\bar{F}^{app}$, the kite aerodynamic force $\bar{F}^{aer}$, the aerodynamic drag force of the cables $\bar{D}_c$ and the traction force on the cables $\bar{F}_k$. In particular, indicating with $\bar{F}_t$ the aerodynamic drag force of one cable, if the system, like for a KiteGen machine, has two cable, then $\bar{D}_c = 2\,\bar{F}_t$.
Using the local coordinates system it is possible to write:

$$\begin{aligned} F_{\vartheta} &= F_{\vartheta}^{gra} + F_{\vartheta}^{aer} + D_{c,\vartheta} \\ F_{\phi} &= F_{\phi}^{gra} + F_{\phi}^{aer} + D_{c,\phi} \\ F_r &= F_r^{gra} + F_r^{aer} + D_{c,r} - F_k \end{aligned} \qquad (2.7)$$

Each of these forces will be now better discussed.

The ***gravity force*** on a KiteGen system is acting both on the kite and on the two lines. The overall gravity force $\bar{F}^{grav}$ may be then expressed as:

$$|\bar{F}^{grav}| = mg + 2\,\bar{W} = \left(m + 2\frac{\rho_c \pi\, d_c^2 r}{4}\right) g \qquad (2.8)$$

where $\bar{W}$ is the weight force acting on one cable, ρ_c is the density of the cable, d_c is the cable diameter and g is the gravitational acceleration. The gravity force vector is oriented on the negative z direction and its formulation in the local coordinates system is:

$$\bar{F}^{grav} = \begin{pmatrix} F_{\theta}^{gra} \\ F_{\phi}^{gra} \\ F_r^{gra} \end{pmatrix} = \begin{pmatrix} \left(m + 2\frac{\rho_c \pi\, d_c^2 r}{4}\right) g \sin\theta \\ 0 \\ -\left(m + 2\frac{\rho_c \pi\, d_c^2 r}{4}\right) g \cos\theta \end{pmatrix} \qquad (2.9)$$

The ***apparent forces*** to be considered are the centrifugal inertial forces acting on the kite, expressed as:

$$\begin{aligned} F_{\theta}^{app} &= m\,(\dot{\phi}^2 r \sin\theta\, \cos\theta - 2\,\dot{r}\,\dot{\theta}) \\ F_{\phi}^{app} &= m\,(-2\,\dot{r}\,\dot{\phi} \sin\theta - 2\,\dot{\phi}\,\dot{\theta}\, r \cos\theta) \\ F_r^{app} &= m\,(r\,\dot{\theta}^2 + r\,\dot{\phi}^2 \sin^2\theta) \end{aligned} \qquad (2.10)$$

The magnitude of the apparent forces, however, is negligible with respect to the other forces acting on the system, therefore in the following their presence will be neglected.

In order to evaluate the ***aerodynamic forces***, instead, the effective wind speed $\bar{V}_e = \bar{V}_w - \bar{V}_{kite}$ is needed. $\bar{V}_{kite}$ is the flying velocity of the kite with respect to the ground and, in the local coordinate system $(\bar{e}_\vartheta, \bar{e}_\phi, \bar{e}_r)$, it can be expressed as:

$$\bar{V}_{kite} = \begin{pmatrix} \dot{\theta}\, r \\ \dot{\phi}\, r \sin\theta \\ \dot{r} \end{pmatrix} \qquad (2.11)$$

It is useful, also, to introduce another coordinate system, the *kite wind coordinate system* $(\bar{x}_w, \bar{y}_w, \bar{z}_w)$. It has the origin in the kite center of gravity, $\bar{x}_w$ aligned with the effective wind speed vector and pointing from the trailing edge of the kite to the leading edge, $\bar{z}_w$ contained in the kite symmetry plane and pointing from the top surface of the kite to the bottom and $\bar{y}_w$ positioned in such a way to complete the right handed system. Expressing these unit vectors in the local coordinate system $(\bar{e}_\vartheta, \bar{e}_\phi, \bar{e}_r)$, it is found that (see [23]):

$$\bar{x}_w = -\frac{\bar{V}_e}{|\bar{V}_e|} \qquad (2.12)$$

$$\bar{y}_w = \bar{e}_w(-\cos(\psi)\sin(\eta)) + (\bar{e}_r \times \bar{e}_w)(\cos(\psi)\cos(\eta)) + \bar{e}_r \sin(\psi) \qquad (2.13)$$

$$\bar{z}_w = \bar{x}_w \times \bar{y}_w \qquad (2.14)$$

where ψ is the control angle already introduced and:

$$\bar{e}_w = \frac{\bar{V}_e - \bar{e}_r(\bar{e}_r \cdot \bar{V}_e)}{|\,\bar{V}_e - \bar{e}_r(\bar{e}_r \cdot \bar{V}_e)|} \qquad (2.15)$$

$$\eta \doteq \arcsin\frac{\bar{V}_e \cdot \bar{e}_r}{|\,\bar{V}_e - \bar{e}_r(\bar{e}_r \cdot \bar{V}_e)|}\tan\psi \qquad (2.16)$$

The aerodynamic force acting of the kite can be split in a drag force and a lift force. The drag force is acting on the direction of the effective wind speed and constitutes a resistance to the kite movement, the lift force instead is perpendicular to the effective wind speed:

$$\bar{F}^{aer} = \bar{D}_k + \bar{L} = -\frac{1}{2}\, C_d\, A\, \rho\, |\bar{V}_e|^2 \bar{x}_w - \frac{1}{2}\, C_l\, A\, \rho\, |\bar{V}_e|^2 \bar{z}_w \qquad (2.17)$$

being A the kite reference area, ρ the air density and C_d and C_l the kite drag and lift coefficients which are nonlinear functions of the angle of attack α. To define the angle of attack α, a last coordinate system needs to be introduced, the *kite body coordinate system* $(\bar{x}_b, \bar{y}_b, \bar{z}_b)$, centered in the kite center of gravity. The unit vector $\bar{x}_b$ is contained in the kite symmetry plane and is pointing from the trailing edge of the kite to the leading edge, the unit

vector $\bar{z}_b$ is perpendicular to the kite surface area and is pointing down and finally $\bar{y}_b$ is set in such a way to complete the right-handed coordinate system. The angle of attack α can be then defined as the angle between $\bar{x}_w$ and $\bar{x}_b$.

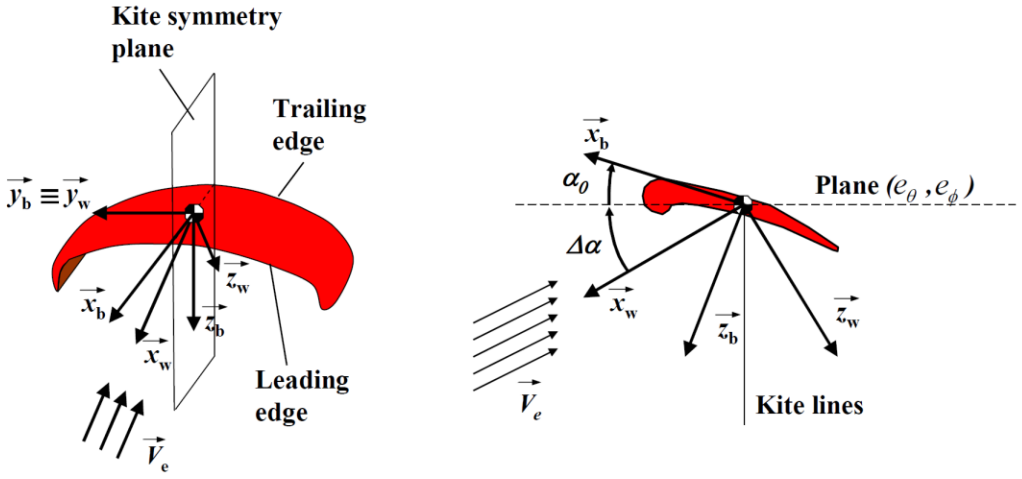

Fig. 2.7: Representation of the kite wind coordinate system ($\bar{x}_w, \bar{y}_w, \bar{z}_w$), body coordinate system ($\bar{x}_w, \bar{y}_w, \bar{z}_w$) and angles α_0 and $\Delta\alpha$. Source [23].

As it can be noticed in the previous picture, the angle of attack may be seen as:

$$\alpha = \alpha_0 + \Delta\alpha \qquad (2.18)$$

It is possible, indeed, to impose a desired base angle of attack α_0 by simply regulating in a suitable way the attack points of the lines to the kite. The difference between α and α_0 is given by:

$$\Delta\alpha = \arcsin\left(\frac{\bar{e_r} \cdot \bar{V_e}}{|\bar{V}_e|}\right) \qquad (2.19)$$

where $\bar{e_r}$ is the unit vector identifying the kite line direction.
The curves of C_l and C_d and of their ratio, i.e. the kite aerodynamic efficiency E, used in this work will be shown in the next chapter, relatively to the KiteGen machine of 3MW.

The ***drag force of one cable*** $\bar{F}_t$ is usually computed considering the approach of [30], which means finding $\bar{F}_t$ passing through the overall angular momentum given by the cable drag force, $\bar{M}_d = r\,\bar{e_r} \times \bar{F}_t$. In particular, $\bar{M}_d$ is computed by means of the integration along the line length of the angular momentum given by the drag force $\bar{F}_{t,\Delta s}$ acting on all the infinitely small line segments:

$$\bar{M}_d = \int_0^r \left(s\,\bar{e_r} \times \bar{F}_{t,\Delta s}(s)\right) ds \qquad (2.20)$$

where:

$$\bar{F}_{t,\Delta s}(s) = \frac{1}{2}\,\rho\, C_{d,c}\, d_c\, \Delta s\, V_n^2(s)\, \bar{e}_n \qquad (2.21)$$

with s identifying the curvilinear abscissa, i.e. the position along the rope, $C_{d,c}$ the cable drag coefficient, d_c the cable diameter, Δs the length of a discretized piece of rope, $\bar{e}_n$ the unit vector normal to the cable surface and $V_n(s)$ the normal component to the cable surface of the effective velocity through the air of the specific discretized piece of rope Δs at the position s. The definition of $\bar{F}_{t,\Delta s}$ points out that the only component of the effective wind velocity along the cable $\bar{V}_e(s)$ responsible for the aerodynamic drag of the cable is the normal one, i.e. $V_n(s)$.

In particular, the conventional approach used in the literature (see [30]) is to consider the cable as a straight line. The velocity $V_n(s)$ along the rope can be computed then simply making a linear interpolation between the kite tangential speed V_k and $0\ m/s$ (at the ground) and $\bar{e}_n$ is simply $\bar{e}_n = -\bar{V}_k/|\bar{V}_k|$. It results therefore that:

$$\bar{M}_d = \int_0^r \left(s\,\bar{e_r} \times \bar{F}_{t,\Delta s}\right) ds = \int_0^r \left(s\,\bar{e_r} \times \frac{\rho\, C_{d,c}\, d_c}{2}\left(\frac{s\,|\bar{V}_k|}{r}\right)^2 \bar{e}_n\right) ds = \\ = r\,\bar{e_r} \times \frac{\rho\, C_{d,c}\, A_c}{8}|\bar{V}_k|^2 \bar{e}_n \qquad (2.22)$$

and the final expression of the cable drag force must be:

$$\bar{F}_t = \frac{\rho\, C_{d,c}\, A_c}{8}|\bar{V}_k|^2\, \bar{e}_n \qquad (2.23)$$

where A_c is the line cross area, i.e. $A_c = r\, d_c$.

Finally, in a KiteGen machine, the ***overall traction force*** $\bar{F}_k$ generated from the kite on the lines is measured by a force transducer on the KSU and is kept constant to a design value by suitably regulating the reel out velocity V_L, as it will be better explained in the following.

2.2.1 Crosswind equations

There are several ways to fly a kite. In the power generation, it was found by Loyd (see [31]) that instead of simply facing the wind, a much more effective flight mode is the so-called crosswind mode. In this mode, "the kite's motion would be approximately transverse to the wind, in the same sense that a wind turbine's blade moves transverse to the wind" [31]. Actually, the kite flight lies on a plane that varies its orientation. In particular, the trajectory of a power kite is typically eight-shaped, its inclination with respect to the ground varies from $35°$ to $60°$, while the azimuth angle ϕ with respect to the absolute wind direction varies between $-22°$ and $22°$.

The equations ruling the dynamic of the kite in crosswind conditions have been derived in several papers (like [23], [31], [32]). In particular the approaches used in [23] and [32] will now be followed. The major equations to be obtain are the equations giving the crosswind velocity and the crosswind power.

2.2.1.1 Crosswind motion law

Let us assume that the kite flies in crosswind conditions with constant speed with respect to the ground and that the inertial and apparent forces are negligible with respect to the aerodynamic ones. Moreover, the projection of the effective wind speed $\bar{V}_e$ on the plane perpendicular to the unit vector $\bar{e}_r$ (and formed by the unit vectors $\bar{e}_\vartheta$ and $\bar{e}_\phi$) is introduced and is called $\bar{V}_{e,p}$. The direction of $\bar{V}_{e,p}$ coincides with the crosswind direction and is identified by the unit vector $\bar{e}_w$ defined as:

$$\bar{e}_w = \frac{\bar{V}_{e,p}}{|\bar{V}_{e,p}|} \qquad (2.24)$$

The kite drag force $\bar{D}_k$ is always directed as the effective wind speed $\bar{V}_e$, while $\bar{L}$ is perpendicular to $\bar{V}_e$. Moreover, under the considered assumptions, the lift force, lies on the plane $(\bar{V}_{e,p}, \bar{e}_r)$. The vectors $\bar{V}_{e,p}$ and $\bar{e}_r$ are instead perpendicular by definition. Therefore the angle between $\bar{L}$ and $\bar{e}_r$ is equal to the angle $\Delta\alpha$ formed between $\bar{D}_k$ and $\bar{V}_{e,p}$.

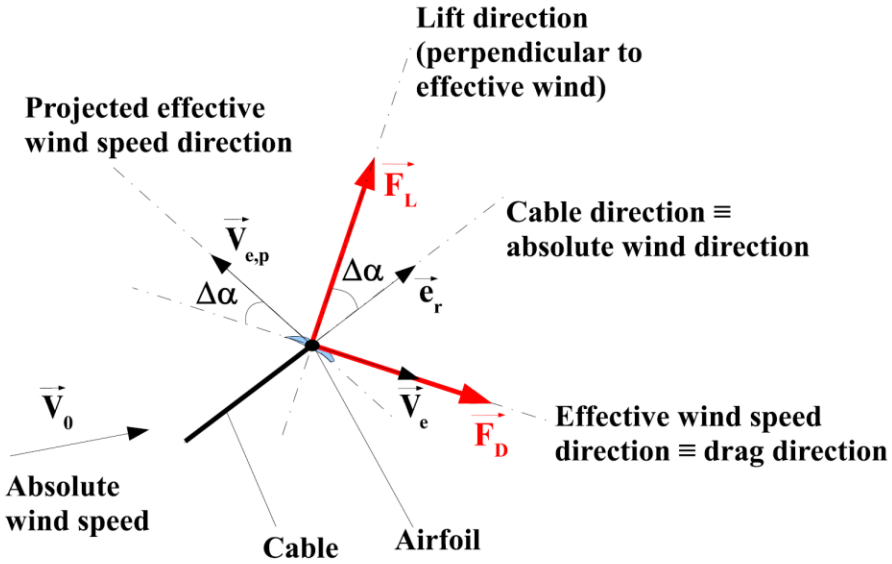

Fig. 2.8: Velocities and forces on a kite flying in crosswind. Picture based on picture from [23].

The kite movement is a combination of a transverse (crosswind) movement and a movement parallel to the kite lines. The crosswind movement is given by the algebraic sum of the projections of the lift and drag forces on the plane (e_ϑ, e_ϕ). The parallel movement, instead, is given by the projections of the lift and drag force on the plane perpendicular to (e_ϑ, e_ϕ) and is the movement responsible for the unrolling of the cables from drums, thanks which electric power is produced.

In the first picture of Fig. 2.9, it is possible to see from a top view how the effective velocity is formed: in general it is given by the algebraic sum between $\bar{V}_w \sin(\vartheta)\cos(\phi)$ and the kite velocity vector $\bar{V}_{kite}$. In particular, $\bar{V}_w \sin(\vartheta)\cos(\phi)$ is the projection of the wind vector on the line direction $\bar{e}_r$, while $\bar{V}_{kite}$ can be split in a radial component $\bar{V}_L$, also lying on the $\bar{e}_r$ direction, and in a tangential component $\bar{V}_k$, lying on the plane (e_ϑ, e_ϕ).

$$\bar{V}_{kite} = V_k\, \bar{e}_w + V_L\, \bar{e}_r \qquad (2.25)$$

Therefore, the effective wind speed is given by the vector sum of $(\bar{V}_w \sin(\vartheta)\cos(\phi) - \bar{V}_L)$ and the crosswind velocity $\bar{V}_k$.
In the particular case that the kite flies perfectly in crosswind direction, then, the reel-out velocity $\bar{V}_L$ is collinear with the absolute wind speed $\bar{V}_w$.

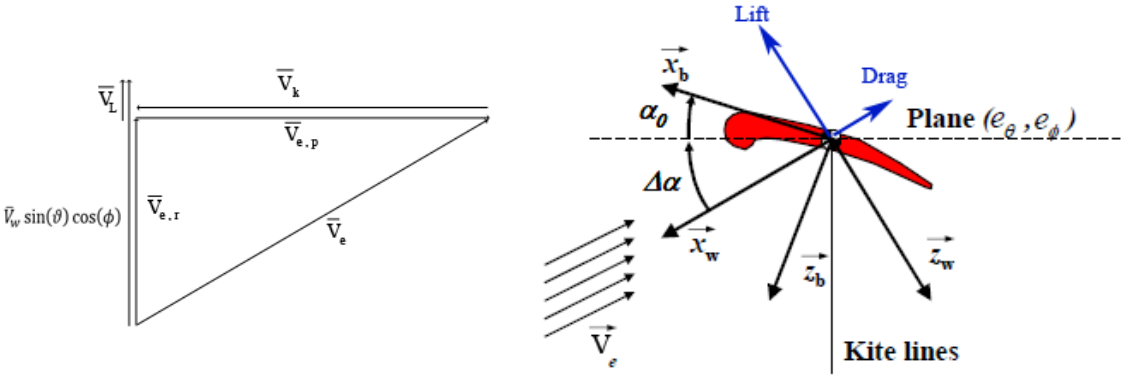

Fig. 2.9: On the left: velocity triangle given by wind velocity $\bar{V}_w$, its projection on the kite line direction $\bar{V}_w \sin(\vartheta)\cos(\phi)$, kite tangential velocity $\bar{V}_k$, kite radial velocity $\bar{V}_L$ and effective velocity $\bar{V}_e$. On the right: Lift and Drag force formation. Picture on the right based on picture from [23].

The value of the crosswind velocity $\bar{V}_{e,p}$, the projection of the effective wind speed on the plane $(\bar{e}_\vartheta, \bar{e}_\phi)$, can be derived following the approach of [32]. Let us describe the aerodynamic force with its projections on the $\bar{e}_w$ and $\bar{e}_r$ directions:

$$\bar{F}^{aer} = \left(-L\sin(\Delta\alpha) + D_k\cos(\Delta\alpha)\right)\bar{e}_w + \left(L\cos(\Delta\alpha) + D_k\sin(\Delta\alpha)\right)\bar{e}_r \qquad (2.26)$$

The angle $\Delta\alpha$ is characterized by:

$$\sin(\Delta\alpha) = \frac{\bar{e}_r \cdot \bar{V}_e}{|\bar{V}_e|} \qquad (2.27)$$

$$\cos(\Delta\alpha) = \frac{\bar{V}_{e,p}}{|\bar{V}_e|} \qquad (2.28)$$

$$\tan(\Delta\alpha) = \frac{\bar{e}_r \cdot \bar{V}_e}{|\bar{V}_{e,p}|} \qquad (2.29)$$

In order to obtain the crosswind velocity, the force balance in the crosswind direction $\bar{e}_w$ is needed:

$$-L\sin(\Delta\alpha) + D_k\, cos(\Delta\alpha) + \ D_c + F_w^{gra} = 0 \qquad (2.30)$$

where D_c is the resulting drag of the cables acting on the kite and $F_w^{gra} = \bar{F}^{\,gra} \cdot \bar{e}_w$ is the component of the gravitational force in the direction of $\bar{V}_{e,p}$. Let us now consider the quadratic formulation of the equation (2.30):

$$(L^2 - F^2)\tan^2(\Delta\alpha) - 2LD_k\tan(\Delta\alpha) + D_k^2 - F^2 = 0 \qquad (2.31)$$

where $F = D_c + F_w^{gra}$. Assuming that $\frac{D_k}{L} \ll 1$ and that $\frac{F}{L} \ll 1$, it is possible to derive

$$\tan(\Delta\alpha) = \frac{D_k}{L} + \frac{F}{L}. \qquad (2.32)$$

Therefore, comparing equation (2.29) with equation (2.32), it is possible to derive that:

$$\left|\bar{V}_{e,p}\right| = (\bar{e}_r \cdot \bar{V}_e)\,\frac{L}{D_k + D_c + F_w^{gra}} = \ \left|\bar{V}_{e,r}\right|\,\frac{L}{D_k + D_c + F_w^{gra}} \qquad (2.33)$$

Finally, since

$$\left|\bar{V}_{e,r}\right| = \left||\bar{V}_w|\sin(\vartheta)\cos(\phi) - \bar{V}_L\right| \qquad (2.34)$$

it is possible to find the final formulation of the crosswind motion law:

$$\left|\bar{V}_{e,p}\right| = \left||\bar{V}_w|\sin(\vartheta)\cos(\phi) - V_L\right|\,\frac{L}{D_k + D_c + F_w^{gra}} \qquad (2.35)$$

This equation, referred in [32] as the *refined crosswind law*, states that the kite crosswind velocity is increased above the projection of the effective wind on the tether direction by the factor $L/(D_k + D_c + F_w^{gra})$. It should be highlighted that F_w^{gra} may be positive or negative according if the kite is moving respectively upwards or downwards. However, it is possible to suitably control the kite flight in such a way to make the kite fly upwards when it is at the center of the eight-shaped trajectory (and therefore at the center of the power zone) and downwards when it is at the edges of the trajectory (and therefore at the edges of the power zone, where there is less power available). It is possible to notice therefore that there is a sort of compensation between the contribution given by the force carried by the wind and the gravitational force.

2.2.1.2 Crosswind Power equation

Using the equilibrium condition between $|\bar{L}|\sin(\Delta\alpha)$ and $|\bar{D}_k|\cos(\Delta\alpha)$ on the plane perpendicular to the vector $\bar{e}_r$, if the contributions of D_c and F_w^{gra} are neglected, it is found that:

$$\frac{|\bar{D}_k|}{|\bar{L}|} = \frac{\sin(\Delta\alpha)}{\cos(\Delta\alpha)} \qquad (2.36)$$

and therefore, using the definition of the kite lift and drag force (see equation (2.17)):

$$\frac{\sin(\Delta\alpha)}{\cos(\Delta\alpha)} = \frac{C_d}{C_l} = \frac{1}{E} \qquad (2.37)$$

where E is the so called aerodynamic efficiency.
From the last equation, considering the relationship $\cos(\Delta\alpha)^2 + \sin(\Delta\alpha)^2 = 1$, it is possible to find:

$$\sin(\Delta\alpha) = \sqrt{\frac{1}{E^2+1}} \qquad (2.38)$$

$$\cos(\Delta\alpha) = \sqrt{\frac{E^2}{E^2+1}} \qquad (2.39)$$

The traction force generated from the kite and acting on the cables is given by the projection of the lift and drag forces on the cable direction, identified by the unit vector $\bar{e}_r$, so:

$$F_k\ \bar{e}_r = \bar{L} \cdot \bar{e}_r + \bar{D}_k \cdot \bar{e}_r \qquad (2.40)$$

The magnitude of F_k can be calculated as:

$$F_k = |\bar{L}| \cos(\Delta\alpha) + |\bar{D}_k| \sin(\Delta\alpha) \qquad (2.41)$$

Recalling the definition of $|\bar{L}|$ and $|\bar{D}_k|$(2.17) and the expressions of $\sin(\Delta\alpha)$ and $\cos(\Delta\alpha)$, see (2.27) and (2.28), it is possible to write:

$$F_k = \frac{1}{2}\rho A C_l \sqrt{\frac{E^2}{E^2+1}} |\bar{V}_e|^2 + \frac{1}{2}\rho A \frac{C_l}{E} \sqrt{\frac{1}{E^2+1}} |\bar{V}_e|^2 = \frac{1}{2}\rho A C_l \sqrt{\frac{E^2+1}{E^2}} |\bar{V}_e|^2 \qquad (2.42)$$

The effective wind velocity may also be defined by means of its projection over the cable direction $\bar{V}_{e,r} = \bar{V}_e \cdot \bar{e}_r$. Then, under the considered assumptions, it is true that:

$$|\bar{V}_e| = \frac{|\bar{V}_{e,r}|}{\sin(\Delta\alpha)} = |\bar{V}_{e,r}| \sqrt{\frac{E^2+1}{1}} \qquad (2.43)$$

Therefore the traction force may be expressed as function of the projection of the effective wind speed on the cable direction:

$$F_k = \frac{1}{2}\rho A C_l \sqrt{\frac{E^2+1}{E^2}}\,(E^2+1)\,\left|\bar{V}_{e,r}\right|^2 \qquad (2.44)$$

$$F_k = \frac{1}{2}\rho A C_l E^2 \left(1+\frac{1}{E^2}\right)^{3/2} \left|\bar{V}_{e,r}\right|^2 \qquad (2.45)$$

Moreover $\left|\bar{V}_{e,r}\right|$ can be expressed as:

$$\left|\bar{V}_{e,r}\right| = \left||\bar{V}_w|\sin(\vartheta)\cos(\phi) - \bar{V}_L\right| \qquad (2.46)$$

where $|\bar{V}_w|$ is the intensity of the wind speed, ϑ and ϕ are the angles identifying the positions of the kite and $\bar{V}_L$ is the reel out velocity.
Since the generated power is the product of the traction force seen by the generators and the reel out velocity, it is found that:

$$P = F_k * V_L = \frac{1}{2}\rho A C_l E^2 \left(1+\frac{1}{E^2}\right)^{3/2} (|\bar{V}_w|\sin(\vartheta)\cos(\phi) - V_L)^2\, V_L \qquad (2.47)$$

In equation (2.47), however, it is neglected the contribution given by the cables to the total drag. In order to consider also this contribution, in the last equation the global aerodynamic coefficient G_e should be used in place of E. In particular, G_e is define as the ratio between the kite lift and the overall drag force, given by the kite drag force D_k and the cable drag force D_c. In the particular case of a system with two cables, like KiteGen, $D_c = 2\,F_t$:

$$G_e = \frac{L}{D_k + D_c} = \frac{L}{D_k + 2\,F_t} \qquad (2.48)$$

The power generated from a KiteGen system can be therefore expressed as:

$$P = F_k * V_L = \frac{1}{2}\rho A C_l G_e^2 \left(1+\frac{1}{G_e^2}\right)^{3/2} (|\bar{V}_w|\sin(\vartheta)\cos(\phi) - V_L)^2\, V_L \qquad (2.49)$$

2.3 KiteGen 3MW machine specifications

As already mentioned in the introduction, the company is currently working on the development of the so-called KiteGen Stem system, with nominal power of 3MW. This system is based on a semi-rigid wing, two ropes, the ground generator and a flexible rod, called *stem*, $20m$ long connected to the control station. The functions of the stem, in which the ropes pass through, are to support and hold the kite when the device is not working and to damp the peak forces in the ropes due to sudden wind-gusts [8].
The *KiteGen power wing* is a semi-rigid wing of $120\ m^2$, wing span of roughly $34\ m$, mean aerodynamic chord of $3.686\ m$ and weight of roughly $180\ kg$. It is formed of nine rigid pieces in composite material linked together by flexible connections. For the central parts of the wing, the E377m airfoil has been used, for the tips of the wing a NACA 1402 and finally the penultimate segments are designed in order to give a smooth transition between the two airfoils.

Fig. 2.10: KiteGen's wing of its 3MW system. Source [18].

In order to evaluate the power performances of the system, it is important to know the aerodynamic characteristics of the wing and in particular the behavior of the lift coefficient C_l, of the drag coefficient C_d and of their ratio, the aerodynamic efficiency $E = C_l/C_d$, to the angle of attack variation. To date, two computational studies and one experimental test have been performed to evaluate these curves, but the issue is still object of study.
The results of the first CFD test of the global wing are here shown.

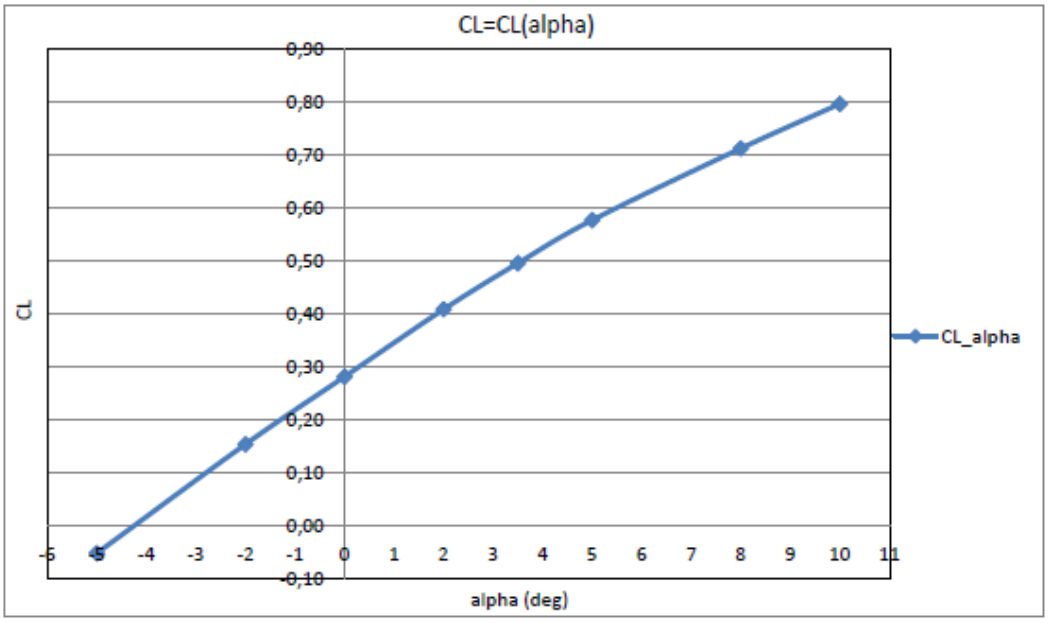

Fig. 2.11: Lift coefficient vs angle of attack α. Data provided by KiteGen Research. First study.

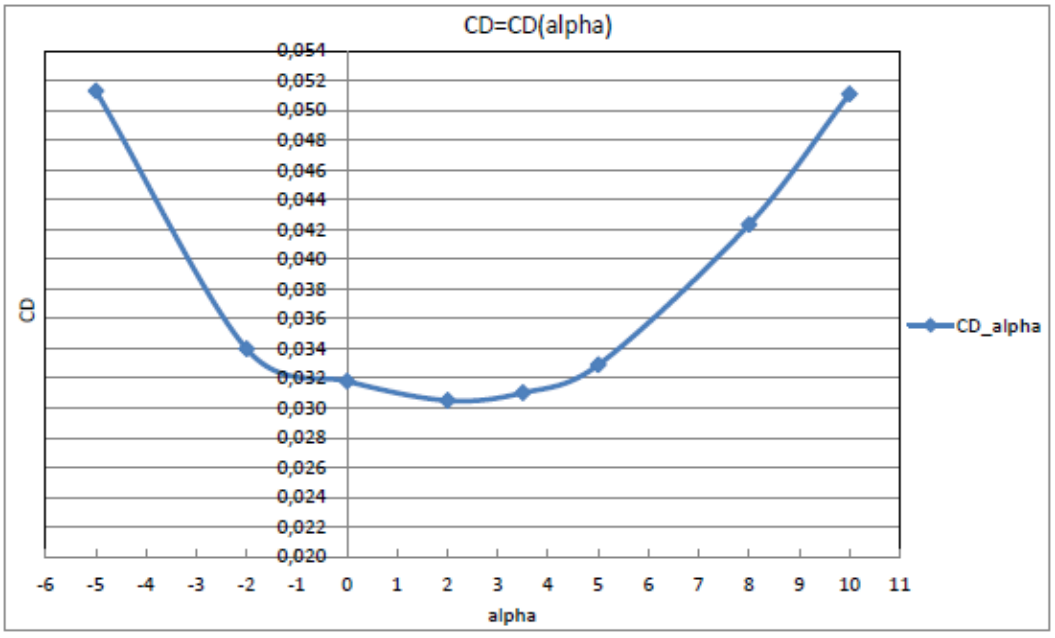

Fig. 2.12: Wing drag coefficient vs angle of attack α. Data provided by KiteGen Research. First study.

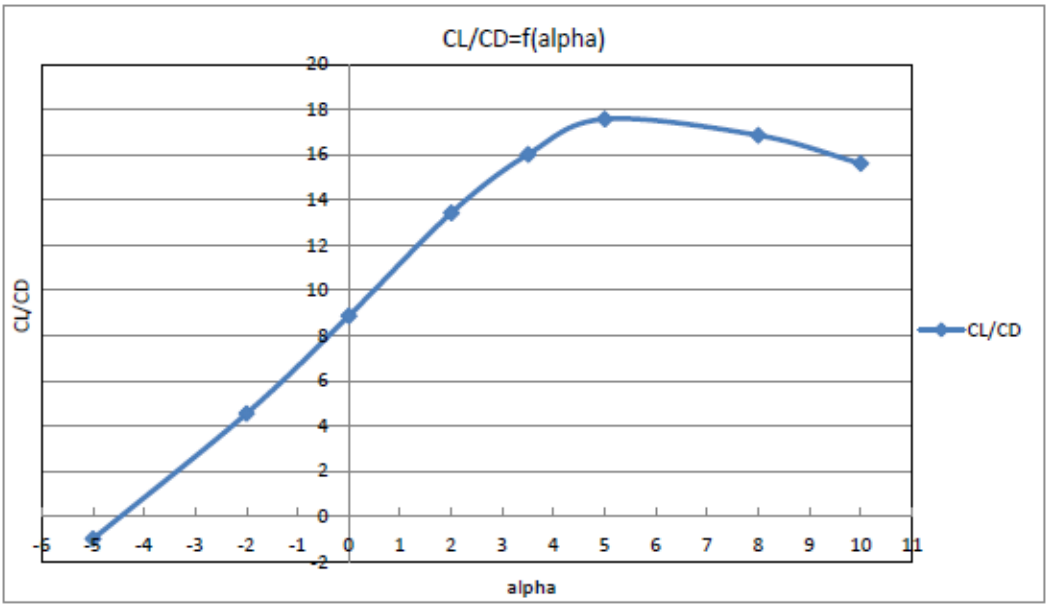

Fig. 2.13: Aerodynamic efficiency vs angle of attack α. Data provided by KiteGen Research. First study.

The previous curves, however, seem to be strongly conservative. The second aerodynamic study, focused instead on the main airfoil used for the wing, the Eppler 377m, highlighted instead how this airfoil should be able to have a much higher aerodynamic efficiency E.

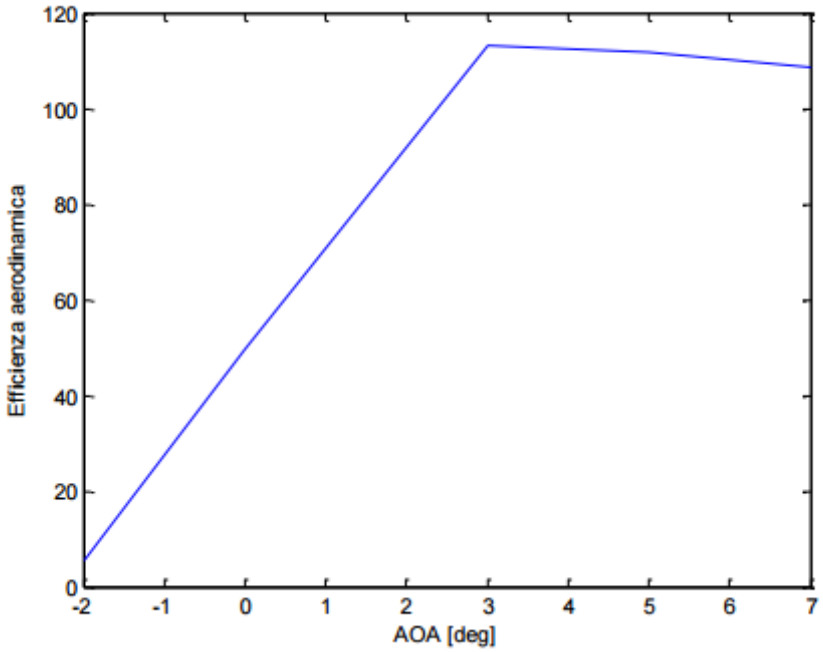

Fig. 2.14: Aerodynamic efficiency $E = C_l/C_d$ vs angle of attack α of an Eppler 377m airfoil. Data provided from KiteGen Research.

The difference between the two analysis seems to be too high to be attributed only to the presence of the last segments with different airfoil.

The experimental test has allowed to identify a maximum aerodynamic efficiency of the overall wing of $\boldsymbol{E = 28}$ with lift coefficient approximately equal to $\boldsymbol{C_L = 1}$. Therefore, from now on, these parameters will be considered in this work, also considering that those values are the design goals of *KiteGen Research* anyway.

2.3.1 Cables specifications

Cables are a key element of a KiteGen system. They connect the kite to the ground generators and therefore allow the power production. During the recovery phase, instead, they are used by the electric drives (in this case acting like motors) to recover the kite in order to start a new cycle. Thanks to the control system, during the recovery phase the force acting on the ropes is much smaller than the force acting during the traction phase, therefore the suitable cables for this application should be found considering the loads during the active phase.
As it will be seen, the control system acts in such a way to keep the traction force on the ropes almost constant during the power production by means of variation of the reel out velocity. This kind of control, therefore, allows to minimize the fatigue stress of the ropes.
The value of the traction force to be kept constant during the flight is the so-called nominal load. Because of the power that KiteGen Research wants to achieve for its machines ($3\ MW$ at the current state), the nominal load applied on each rope is of $150kN$. However, since wind gusts may occur and the control system acts with a certain delay, it is suitable to define a maximum load, which is the nominal force multiplied for a safety coefficient. The value of the maximum load should be still minor than the breaking load of the rope.
Among all the different types of fibers tested by KiteGen Research, it has been found that the best ones for this application are the Dyneema® fibers. They are polyethilenic fibers HT (high tension) produced by DSM in the original form of a thread of around 20 micron of diameter. Several threads are woven together to form a composite which is usually sold by DSM as a raw material for the construction of ropes and fabrics. The ropes are then produced by other companies, like Armare in Italy.
These fibers are known for their extraordinary combination of lightness, strength and durability. They are also characterized by extremely reduced elongation, good creep behavior, extraordinary resistance to abrasion and impermeability. At the state of the art, the best performing Dyneema® fiber produced by DSM is the SK99.
With regard to the breaking load, on the website of Armare [33], it is possible to find a table giving the breaking load and the linear density of ropes done with Dyneema® SK99 as function of the diameter.

	SINGLE BRAID (WITHOUT A COVER)	
ø [mm]	BREAKING LOAD [daN]	WEIGHT [g/m]
1	300	1.20
1,5	450	1.81
2	615	2.41
2,5	960	3.61
3	1,444	6.02
3,5	2,200	9.63
4	3,000	11.20
5	4,282	18.05
6	6,200	22.86
7	8,080	29.90
8	9,836	38.80
9	12,446	48.13
10	14,680	58.80
11	16,495	62.00
12	18,220	77.00
13	22,177	95.22
14	25,262	110.00
15	28,748	129.00
16	30,000	145.00
17	-	-
18	34,600	180.00
20	45,900	216.00

Tab. 2.1: Characteristics of a rope made of Dyneema® SK99 as function of its diameter. Source [33].

If compared to steel wire ropes, a rope of Dyneema® with the same diameter results to be roughly 8 times lighter and 2 times stronger.
Concerning instead the elasticity of the rope, Dyneema® fibers are characterized by a very high elasticity modulus, of 155 GPa [34] for the SK99.

2.4 KiteGen power curves

During the years, several attempts of optimizing the operations of a KiteGen system have been done. Let us recall equation (2.47), which describes the generated power during crosswind operations:

$$P = F_k * V_L = \frac{1}{2}\rho A C_l E^2 \left(1 + \frac{1}{E^2}\right)^{\frac{3}{2}} (|\bar{V}_w| \sin(\vartheta)\cos(\phi) - V_L)^2 \, V_L \qquad (2.50)$$

where F_k represents the traction force generated from the kite. Firstly, it can be noticed that the generated power is proportional to the quantity $|\bar{V}_w| \sin(\vartheta)\cos(\phi)$, and therefore, if the wind speed is assumed to be constant with respect to the elevation and parallel to the ground, the theoretical optimal condition occurs when $\vartheta = \pi/2$ and $\phi = 0$. Moreover, from [31] on, the conventional approach used is to optimize the generated power as function of the reel-out velocity V_L having as physical constrain that $V_L < |\bar{V}_w|$. Therefore, it is possible to find the optimal value of V_L by imposing that:

$$\frac{d\,P}{d\,V_L} = 0 \qquad (2.51)$$

From straightforward calculations, it is found that:

$$\frac{d\,P}{d\,V_L} = 3\,V_L^2 - 4\,|\bar{V}_w|\,V_L + |\bar{V}_w|^2 = 0 \qquad (2.52)$$

which gives as optimal result:

$$P = \frac{1}{2}\rho A C_l E^2 \left(1 + \frac{1}{E^2}\right)^{3/2} (|\bar{V}_w| - V_L)^2 \, V_L = \frac{4}{27}\,\frac{1}{2}\rho A C_l E^2 \left(1 + \frac{1}{E^2}\right)^{3/2} |\bar{V}_w|^3 \qquad (2.53)$$

when

$$V_L = \frac{|\bar{V}_w|}{3} \qquad (2.54)$$

as already obtained in [31]. It is important to underline that this expression of the maximum power is only a theoretical upper bound since considers constant wind speed with the altitude. Moreover, if an entire active cycle is considered it is clear that, since the kite is moving in the air, it cannot stay in theoretical optimal position $\vartheta = \pi/2$ and $\phi = 0$, even though the eight-shaped trajectory comes from the attempt of staying as close as possible to the optimal angle $\phi = 0$. Nevertheless, even when these factors are considered, this kind of optimization brings to a situation in which, in order to maximize the power output of the machine, both the reel-out velocity of the cable and the traction force on the lines should be able to increase with increasing absolute wind speed. In reality, however, the cables are characterized by a tensile strength and following the Loyd's scenario, the tension would quickly overpass this value, bringing to the breakage of the cables. This kind of operation has therefore a dramatic conclusion: the use of the tropospheric wind technology has an intrinsic limit due to the fact that beyond a certain altitude the wind speed would create a traction force on the tether so high to break the cables.

KiteGen Research decided therefore to use a different practical approach for the operation specifications, which has led to the creation of the KiteGen characteristics curves.

Before introducing these curves, it is important to clarify, ones again, that in this section the aerodynamic drag generated from the cables F_t will be neglected, i.e. in the next equations E will be used in place of G_e. Then, Chapter 4, F_t will be computed using different numerical approaches and in Chapter 5 the power curves obtained using G_e will be evaluated.

The characteristics curves show how the KiteGen machines will operate with respect to the value of the absolute wind velocity and in particular may be divided in four zones:

- zone A: the device is switched off because the wind speed is below the *cut-in wind speed*, which is the value of the absolute wind speed that allows the kite to fly at the design crosswind speed of $80\ m/s$. The cut-in velocity is therefore calculated computing $|\bar{V}_w|$ from the equation

$$\left|\bar{V}_{e,p}\right| = \left||\bar{V}_w| \sin(\vartheta)\cos(\phi) - V_L\right| E \qquad (2.55)$$

- zone B: the cables are hold in position without unrolling from the drums and the force increases following the equation

$$F_k = \frac{1}{2}\rho A C_l E^2 \left(1 + \frac{1}{E^2}\right)^{3/2} (|\bar{V}_w| \sin(\vartheta)\cos(\phi) - V_L)^2 \qquad (2.56)$$

  Since $V_L = 0$, the power output is still equal to zero. The aim of this zone is to reach the nominal force of $F_k = 300kN$, which means traction force of $150kN$ per rope;

- zone C: the force reaches the nominal value of $300\ kN$ and the corresponding starting wind velocity of the zone is called *full-force velocity*. In this zone, the cables are reeled out with a speed computed in such a way to keep the force constant at its nominal value. Practically, this calculation is easily performed by computing V_L as:

$$V_L = |\bar{V}_w| \sin(\vartheta)\cos(\phi) - V_{full-force} \sin(\vartheta)\cos(\phi) \qquad (2.57)$$

  Since now both V_L and F_k are different from zero, the power generation starts;

- zone D: when also the reel out speed reaches its maximum value, the maximum power output of the machine is reached and in order to keep it constant the kite is positioned outside the power zone, and in particular in a position in which the design traction force of $150kN$ per rope can be obtain with the maximum value of the reel out velocity V_L. The wind speed at which this zone begins is called *full-power velocity*.

Since, during the operations, the inclination angle with respect to the ground (the complementary angle of ϑ) is expected to vary in the range of $35° \div 60°$, while the azimuth angle ϕ is expected to vary in the range of $-22° \div 22°$, in the previous calculations the values of $\vartheta = 45°$ and $\phi = 11°$ have been used. As already mentioned, the lift coefficient and aerodynamic coefficient have bee set equal to $C_l = 1$ and $E = 28$. Regarding the air density, a conservative value of $\rho = 1\ kg/m^3$ (that corresponds to the air density at $2000m$ of elevation) has been used. The kite reference area is instead $A = 120\ m^2$. The maximum value of the reel out velocity has been set to $V_L = 13.5\ m/s$. The next curves, therefore,

describe a machine with power output during the active phase of $4\ MW$. According to the indications provided from KiteGen Research, indeed, this should allow to obtain a mean power output of $3MW$ considering that the energy actually spent during the recovery phase is very low (remember that the side slip maneuver is used) and that this phase can be performed very quickly thanks to the reel-in velocity of the drums of roughly $15 \div 20\ m/s$.

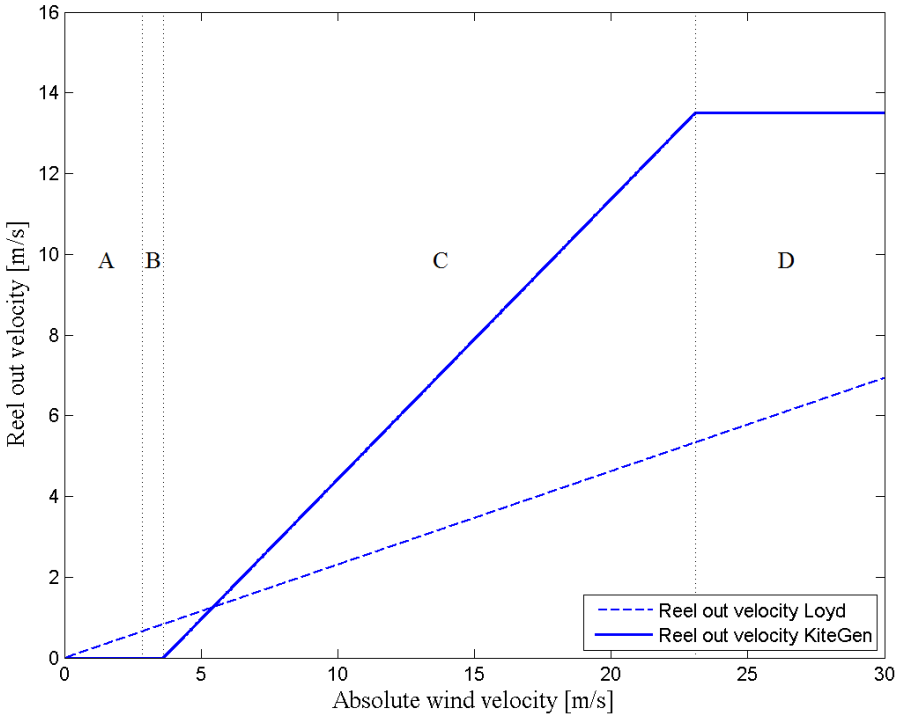

Fig. 2.15: Reel out velocity vs absolute wind velocity during the KiteGen operations and with the Loyd's approach. The four characteristic zones are visible.

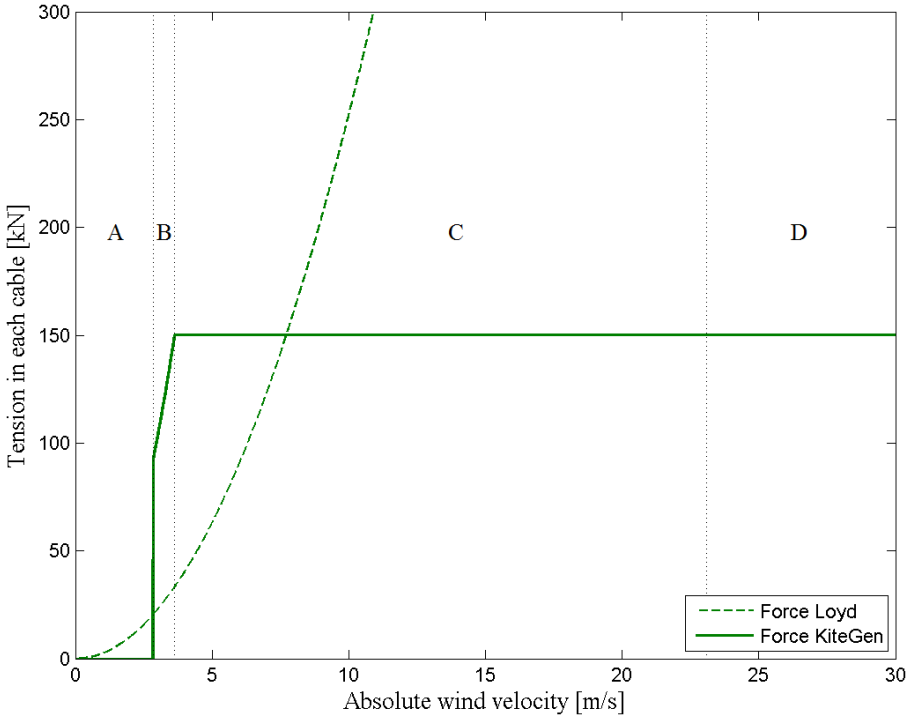

Fig. 2.16: Traction force generated on each cable vs absolute wind velocity during the KiteGen operations and with the Loyd's approach. The four characteristic zones are visible.

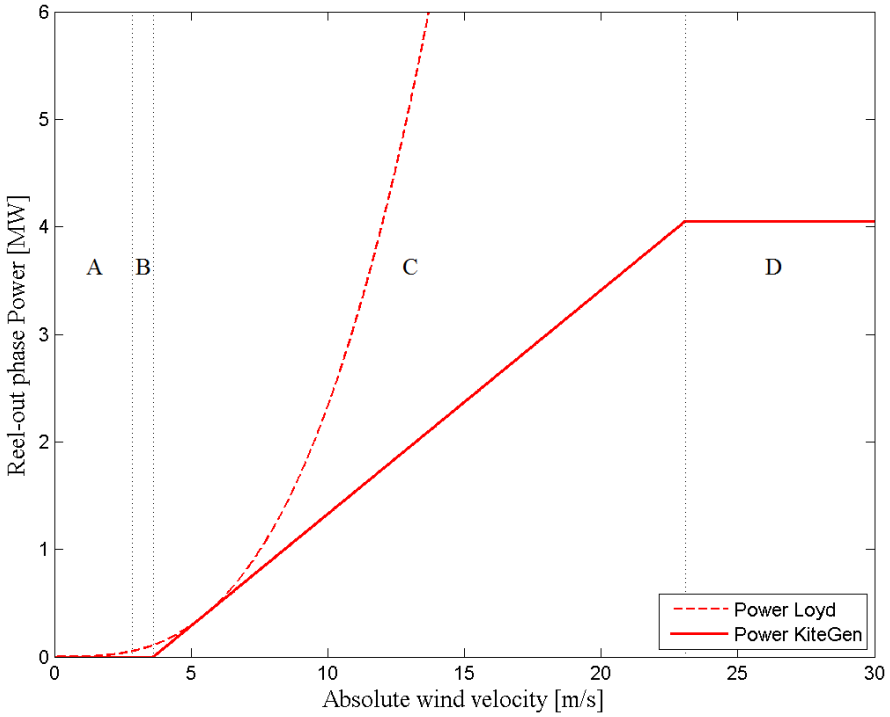

Fig. 2.17: Power generated during the active phase vs absolute wind velocity during the KiteGen operations and with the Loyd's approach. The four characteristic zones are visible.

In the previous figures, also the curves that could be obtained using the Loyd's approach have been represented. In particular, these curves have been obtained using the equations (2.53) and (2.54).

Regarding the KiteGen characteristic curves, with the operational parameters previously described, it is possible to notice that the *cut-in velocity* is $2.86\ m/s$, the *full force velocity* is $3.63\ m/s$ and the *full power velocity* is $23.09\ m/s$.

3. Wind model

From the previous discussion, it is clear how important the characteristics of the wind as function of the altitude are. In particular, it is important to have data regarding the wind speed and the occurrence of the wind during the year for a specific location. These information may be obtained for several locations using the RAOB (Radiosonde Observation) database of the National Oceanographic and Atmospheric Administration (NOAA), an american federal agency focused on the condition of the oceans and the atmosphere.
During these measurements, a sounding balloon is used. This special balloon carries instruments aloft able to measure atmospheric pressure, temperature, humidity, wind speed magnitude and direction. All these data are then sent back to the ground station via radio. In particular, a radiosonde whose position is tracked during the flight in order to give wind speed and direction is called *rawinsonde* (from "radar wind-sonde").

Fig. 3.1: Picture of a sounding balloon. Source [35].

Since in several papers dealing with kite power production the evaluations of the possible performances of these machines are done for the site of De Bilt in The Netherlands, in order to make the results easily comparable, the same location is considered in this work.
The wind shear (i.e. the difference in wind speed with altitude variation) has been modelled in the literature in several ways. The most common models used are the *wind power law* and the *wind logarithmic law*.

The wind power law is formulated as:

$$V_w(z) = V_0 \left(\frac{z}{z_0}\right)^{\alpha_p} \qquad (3.1)$$

where $V_w(z)$ is the wind speed at the altitude z, V_0 is the wind speed at the altitude z_0 and the coefficient α_p is an empirically derived coefficient which takes into account the roughness of a specific surface. For instance, for smooth ground its value is 0.10, while for urban areas with tall buildings it can reach the value of 0.4.
The logarithmic law states instead:

$$V_w(z) = V_0 \frac{\ln\left(\frac{z}{z_r}\right)}{\ln\left(\frac{z_0}{z_r}\right)} \qquad (3.2)$$

where this time the roughness effect is considered with the coefficient z_r.
In the following sections of this work, the logarithmic law will be used and in particular for the site of De Bilt the coefficients V_0, z_0 and z_r already derived in [23] with least square procedure will be used. The value of these coefficients varies according to the considered period of the year (winter: $V_0 = 5.1\ m/s$, $z_0 = 27.5\ m$ and $z_r = 3.5\ m$; summer: $V_0 = 4.4\ m/s$, $z_0 = 27.5\ m$ and $z_r = 2.1\ m$) and in particular it is found that during the winter months the wind is characterized by an higher speed.

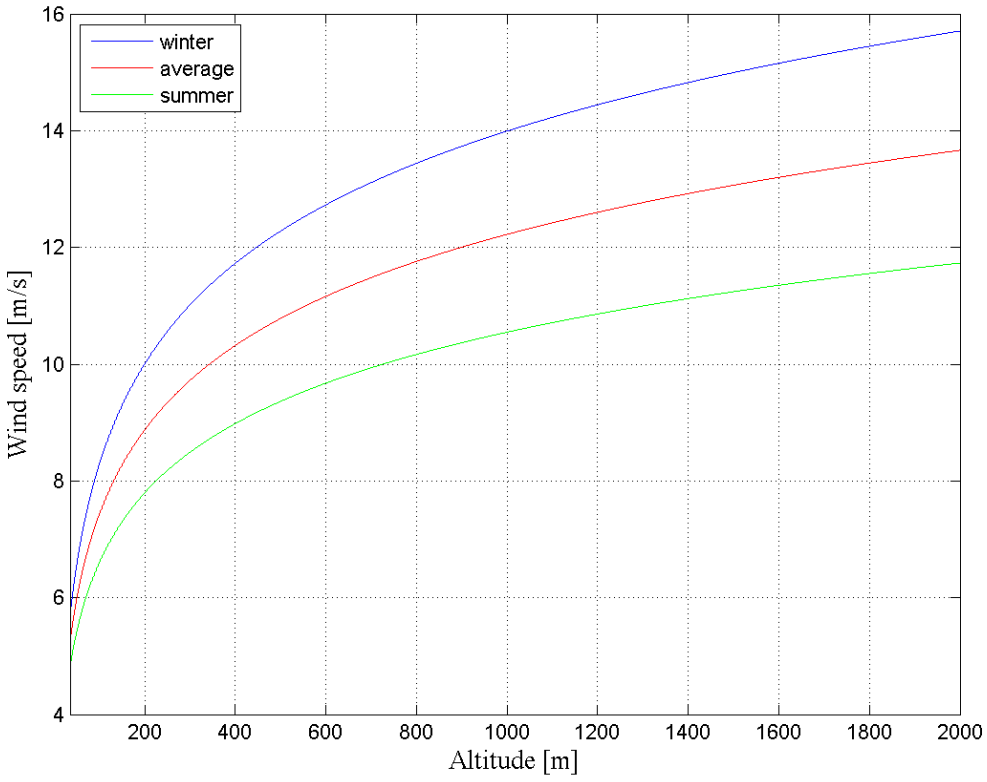

Fig. 3.2: Wind profile vs altitude for the location of De Bilt. The coefficients for the wind logarithmic law have been taken from [23].

Regarding the wind occurrence, instead, several probability functions have been obtained in this work based on the RAOB measurements from 2004 to 2014 of the NOAA database for the site of De Bilt. Each function refers to a specific range of altitude and describes the probability of having wind at a certain speed at the considered elevation. In particular, each of the following probability functions refer to a range of altitude $\Delta z = 300m$, starting from $z = 200m$ up to $z = 2300m$. The value of Δz has been chosen since in the following it will be assumed a KiteGen machine operating with average $\vartheta = 45°$, whose cables will unroll from the drums for roughly $450m$.
In the following, the wind probability functions referring to the elevation ranges of $200 \div 500m$ and $2000 \div 2300m$ will be shown, while the probability functions of the remaining ranges will be shown in Appendix A.

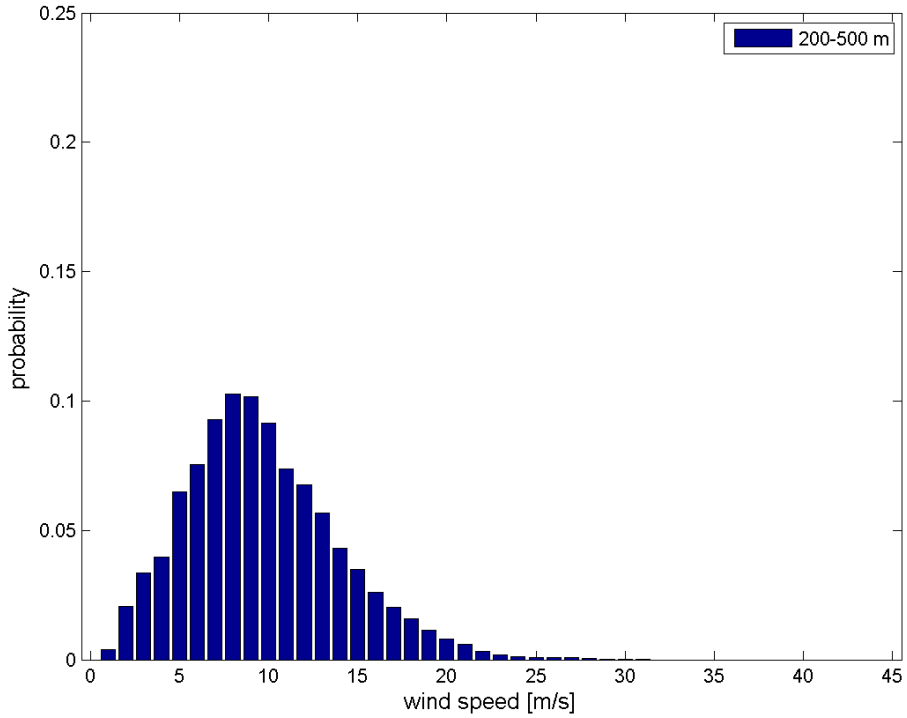

Fig. 3.3: Wind probability function for the site of De Bilt between 200m and 500m of altitude.

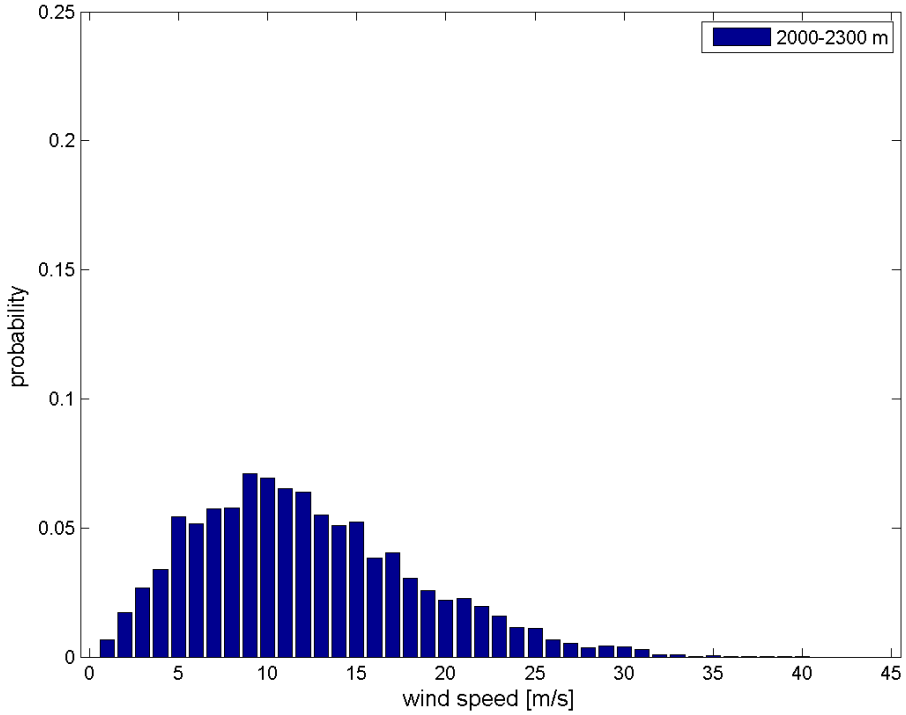

Fig. 3.4: Wind probability function for the site of De Bilt between 2000m and 2300m of altitude.

4. Estimation of the cables aerodynamic drag

Ones that the capability of the machine during the reel-out phase has been established with the curves of section 2.4, in order to find the actual average power output two main phenomena should be considered. The first is the effect of the aerodynamic drag of the cables to the flight dynamics, i.e. the influence of the cables drag to the definition of the global aerodynamic efficiency G_e. The second phenomenon is the recovery phase, which reduces the average power output because of the (little) power consumption needed in this phase and, most importantly, because of the not production during the period of time needed to perform the maneuver.

In particular, in this chapter, the aerodynamic drag of the cable will be estimated using two different approaches: first the cable will be considered as a straight line and then as a flexible rope connected to a kite performing a realistic trajectory. In both the cases, however, the rope will be treated as inelastic. Moreover, as it will be seen, in the second approach another effect neglected in the first analysis will be added: the variation of the cable tension along the rope due to the external forces.

Both the cases will be analyzed through numerical simulation and the value of the overall aerodynamic drag force of the cable will be computed following the approach of [30]. In particular, first the overall angular momentum given by the drag force is found from the integration of the angular momenta given from the aerodynamic drag forces $\bar{F}_{t,\Delta s}$ acting on each discretized piece of rope Δs, then, knowing the distance r from the origin of the Cartesian coordinate system to the kite, it is possible to find the overall aerodynamic drag force of the cable $\bar{F}_t$. In formula:

$$\bar{M}_d = \int_0^r \left(s\ \bar{e_r} \times \bar{F}_{t,\Delta s}\right) ds = r\ \bar{e_r} \times \bar{F}_t \qquad (4.1)$$

where $\bar{e_r}$ is the unit vector identifying the direction of r. Finally, the cable diameter d_c has been set equal to $11\ mm$, where this value has been chosen according to Tab. 2.1 in such a way to high breaking load bigger than $150\ kN$.

4.1 Straight lines

In this first simple model, the lines are considered to be inelastic and straight during the flight. It is the most used model in the literature and will be used as a reference case for the next calculations. In this first simple analysis, it is considered that the kite is flying at constant transversal speed of 80 m/s and that the ropes are kept at constant length, i.e. they are not unrolling from the drum. Since it is assumed that the air is quiet and the length of the cables is constant, the effective speed of each element of the rope will be equal to its crosswind velocity, i.e. $V_e(s) = V_n(s)$. Because of the straight configuration of the rope, the velocity at which it is moving in the air will be equal to 80 m/s at the top and then will linearly decrease to 0 m/s at the bottom. Finally, as example for the first simulation, the length of the rope has been set to $1000m$ and the polar angle $\vartheta = 45°$.
The purpose of the simulation is to find the aerodynamic drag of one cable and then the overall drag of two cables will be simply found doubling the obtained result.
As already mentioned, the overall aerodynamic drag force of one cable will be computed by means of the angular momentum given from the drag force $F_{t,\Delta s}$ acting on all the discretized pieces of the rope Δs as the cable moves in quiet air. In particular $F_{t,\Delta s}$ is computed as:

$$F_{t,\Delta s}(s) = \frac{1}{2}\,\rho(z)\,C_{d,c}(Re)\,d_c\,\Delta s\,V_n^2(s) \qquad (4.2)$$

where $\rho(z)$ is the density of the air, function of the altitude z, $C_{d,c}(Re)$ is the cable drag coefficient, function of the Reynolds number R, d_c is the diameter of the line, Δs is the length of the discretized piece of the line and $V_n(s)$ is the normal component of the effective wind velocity of a specific point of the rope, identified from the curvilinear abscissa s.

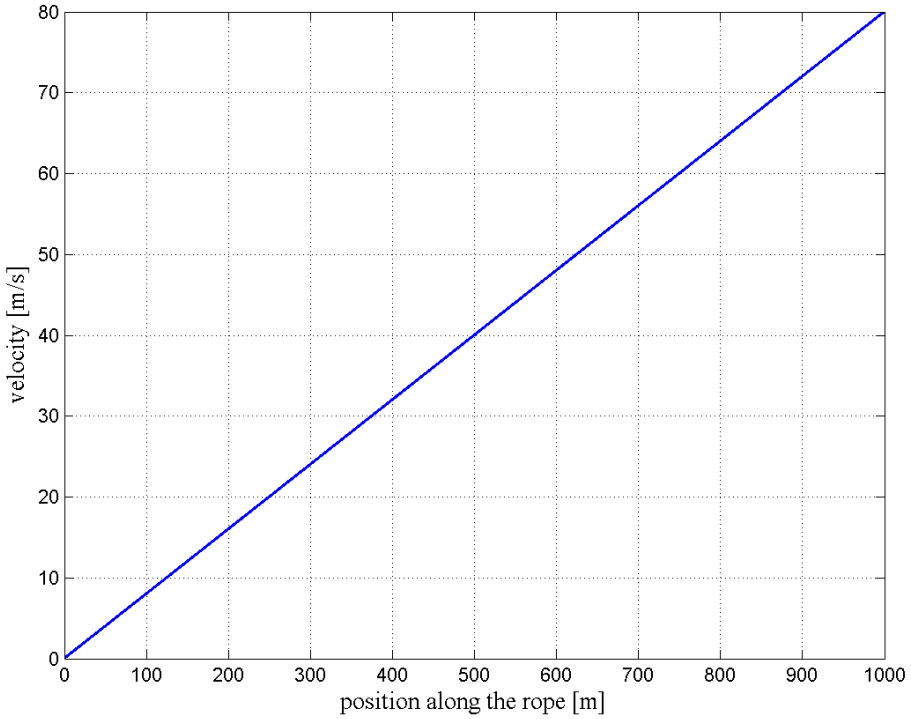

Fig. 4.1: Line velocity along a 1000m long straight cable attached to a kite flying at 80 m/s..

Ones that the velocity of the cable is known, the value of the cable drag coefficient $C_{d,c}$ is needed. In the literature there are several papers (such as [36] or [37]) which, mostly through experimental tests, give the value of C_d of a cylinder as function of the Reynolds number Re, whose formulation is

$$Re(s) = \frac{\rho(z)\ V_n(s)\ d_c}{\mu_{air}(z)} \qquad (4.3)$$

where $\mu_{air}(z)$ is the air viscosity, changing with the altitude z. The value of $\rho(z)$ and $\mu_{air}(z)$ are taken from the International Standard Atmosphere (ISA) tables. Sample values of the ISA table are here shown:

International Standard Atmosphere (ISA) table		
$\boldsymbol{z\ [m]}$	$\boldsymbol{\rho[kg/m^3]}$	$\boldsymbol{\mu_{air}[kg/(m\,s)]}$
0	1.225	0.178e-4
200	1.201	0.178e-4
400	1.178	0.177e-4
600	1.155	0.177e-4
800	1.133	0.176e-4
1000	1.111	0.175e-4
1200	1.089	0.175e-4
1400	1.068	0.174e-4
1600	1.047	0.173e-4
1800	1.026	0.173e-4
2000	1.006	0.172e-4

Tab. 4.1: Air density ρ and viscosity μ_{air} as function of the elevation from the ground z. Samples from the ISA table.

The computed value of the Reynolds number along a rope of $d = 11\ mm$, length of $1000\ m$ and polar angle $\vartheta = \pi/4$ is here plotted:

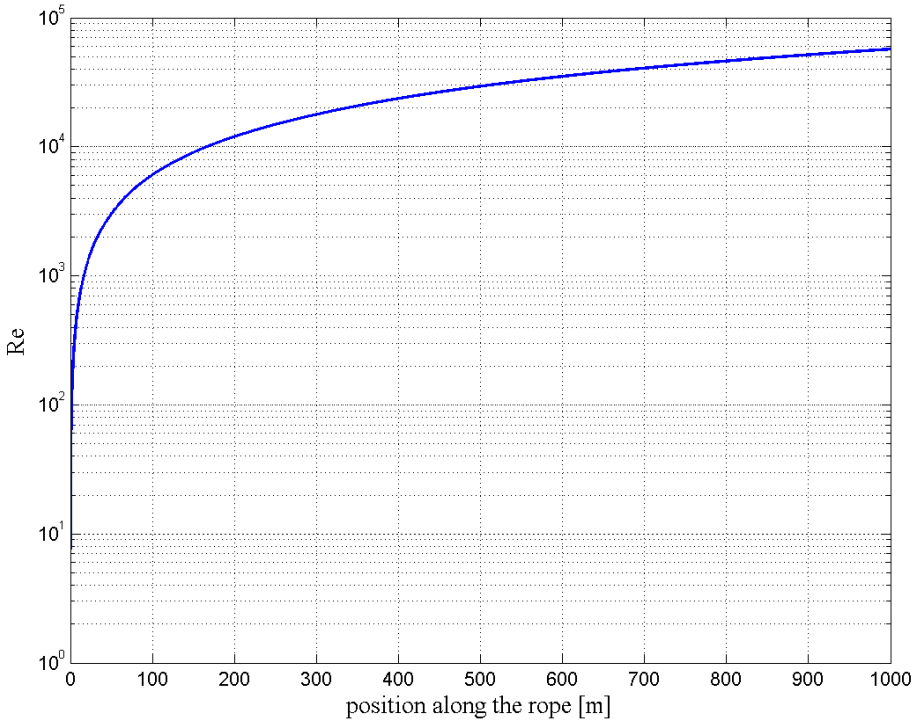

Fig. 4.2: Reynolds number Re along a 1000m long rope of diameter d=11mm. Semi logarithmic graph.

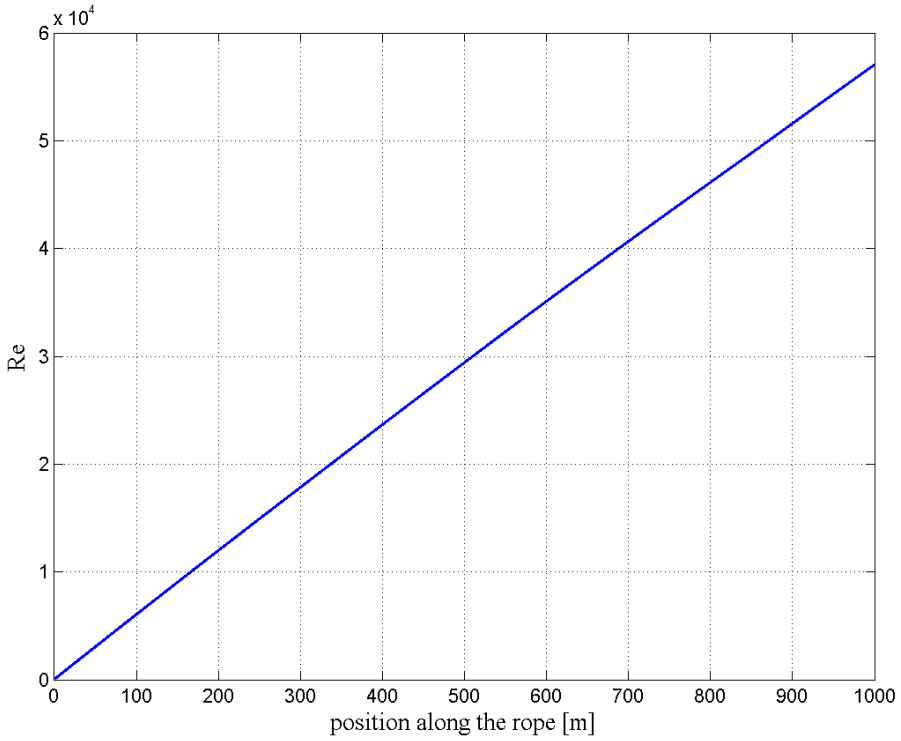

Fig. 4.3: Reynolds number Re along a 1000m long rope of diameter d=11mm.

Finally $C_{d,c}$ can be computed. In particular:

- for Re>40, the graphs available in the literature and resulting by experimental tests have been used

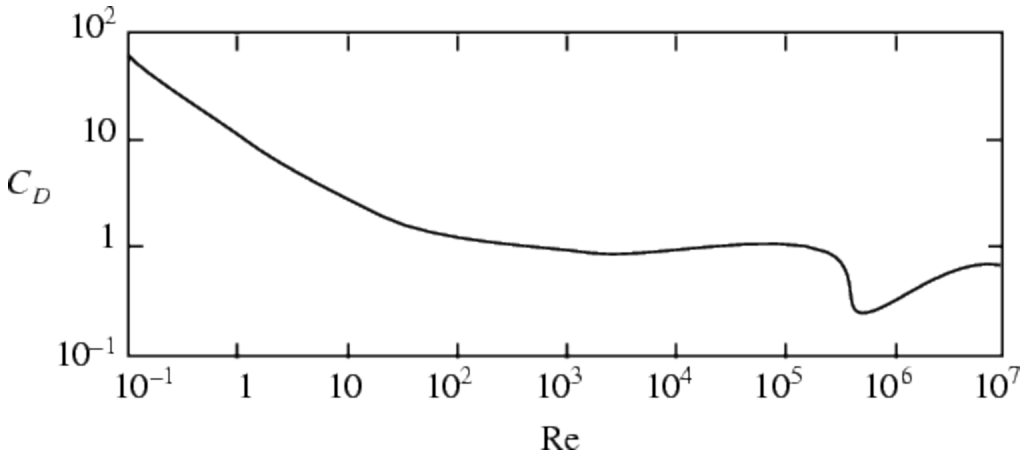

Fig. 4.4: Drag coefficient of an infinite circular cylinder C_D vs Reynolds number. Source [38].

- for Re<40, since the results given by the experiments may have small accuracy, the expression of $C_{d,c}$ derived in [39] is used:

$$1/2\ C_{d,c} = 2\left(\frac{\pi}{Re}\right)^{\frac{1}{2}} B \qquad (4.4)$$

where

$$B(Re) \approx 1.16 + 5.1 \cdot 10^{-3} Re - 1.9 \cdot 10^{-5}\ Re^2 \qquad (4.5)$$

The resulting value of $C_{d,c}(s)$ found along the rope is

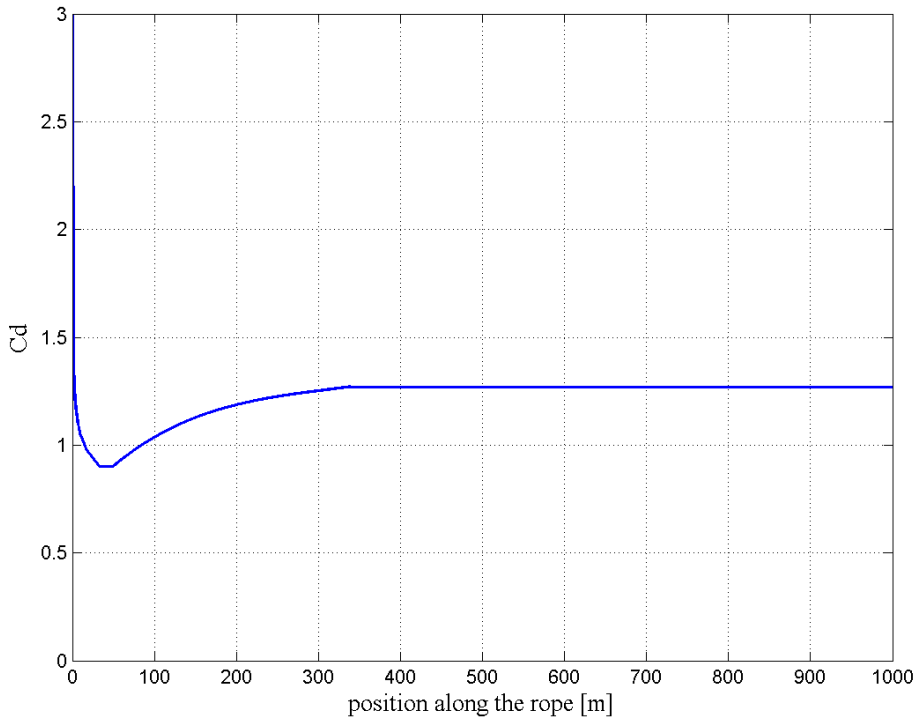

Fig. 4.5: Computed cable drag coefficient $C_{d,c}$ along a 1000m long straight rope of diameter d=11mm.

Zooming on the first $15\ m$ of the rope, it can be noticed that, because the flow of the air becomes laminar instead of turbulent, the value of $C_{d,c}$ increases.

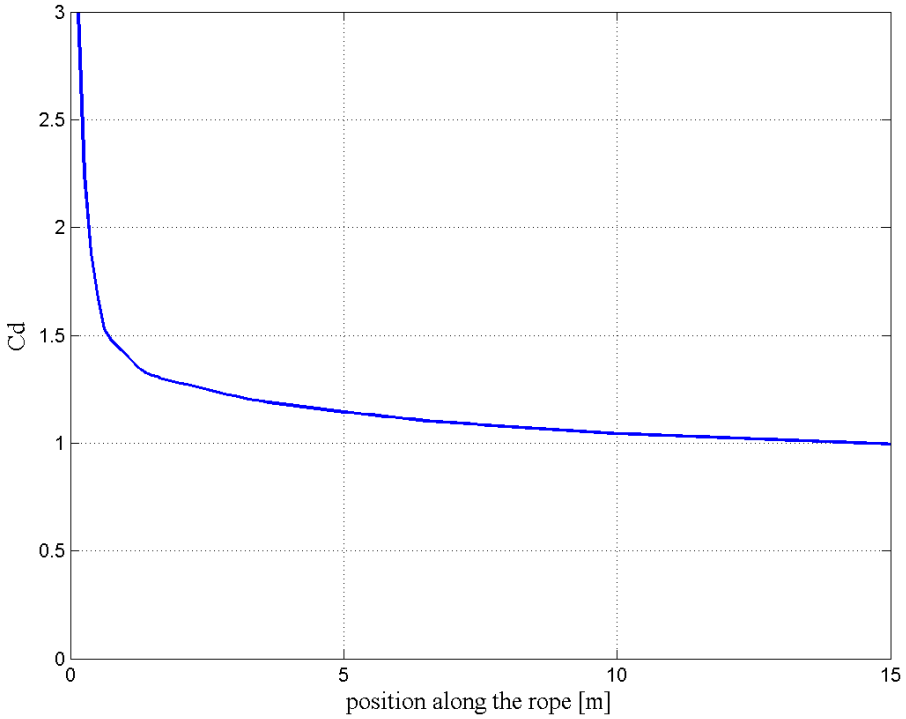

Fig. 4.6: Computed cable drag coefficient $C_{d,c}$ along a 1000m long straight rope of diameter d=11mm. Zoom on the first 15 meters.

It should be highlighted, however, that even though the highest $C_{d,c}$ is found at the beginning of the line, in that part of the domain the effective wind velocity is much smaller than in the highest part of the line. Therefore, since the cable drag force is proportional to the square of the velocity, it is expected that the majority of the air resistance will be given by the highest part of the cable. Moreover, this region in which the $C_{d,c}$ of the cable assumes high values is actually very small. This expected behavior is confirmed from the next graph, which shows the formation of the overall aerodynamic resistance along the line.

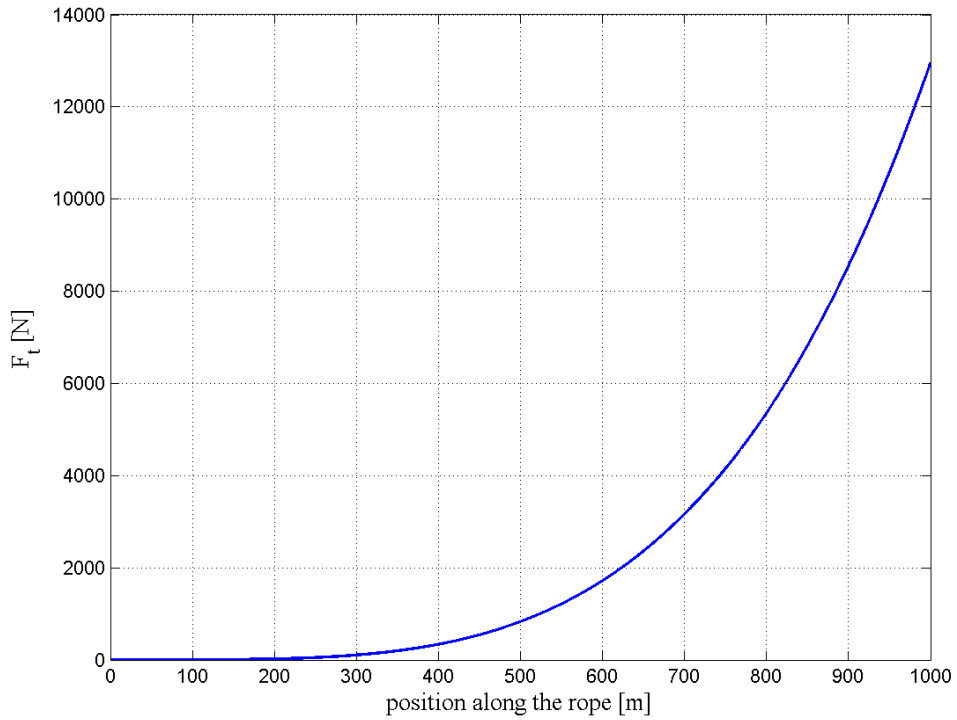

Fig. 4.7: Total drag force F_t formation along a 1000m long straight rope of diameter d=11mm.

With this analysis therefore, the total drag force for a $1000\ m$ long cable of $d = 11\ mm$ is:

$$F_t = 12949\ N$$

Using instead the formula derived in [30], which means using

$$F_t = \frac{\rho\ C_{d,c}\ A_c}{8} V_n^2 \qquad (4.6)$$

would have led to an aerodynamic drag force of $13227\ N$. In particular, as air density ρ has been used its average value between $0\ m$ and $707\ m$ of altitude (elevation covered from a $1000m$ long cable with inclination of 45°), so $1.1835\ kg/m^3$, while for the cable drag coefficient the value of $C_{d,c} = 1.27$ has been considered along the entire rope. It is found therefore that the results of the two calculations fit quite well, and the slightly lower value found in the present analysis is given from the evaluation of a local drag coefficient along the line.

Finally, it is possible to make a parametric analysis of the drag force acting on ropes of different lengths, again considering the line with $\vartheta = \pi/4$ and having $d = 11\ mm$.

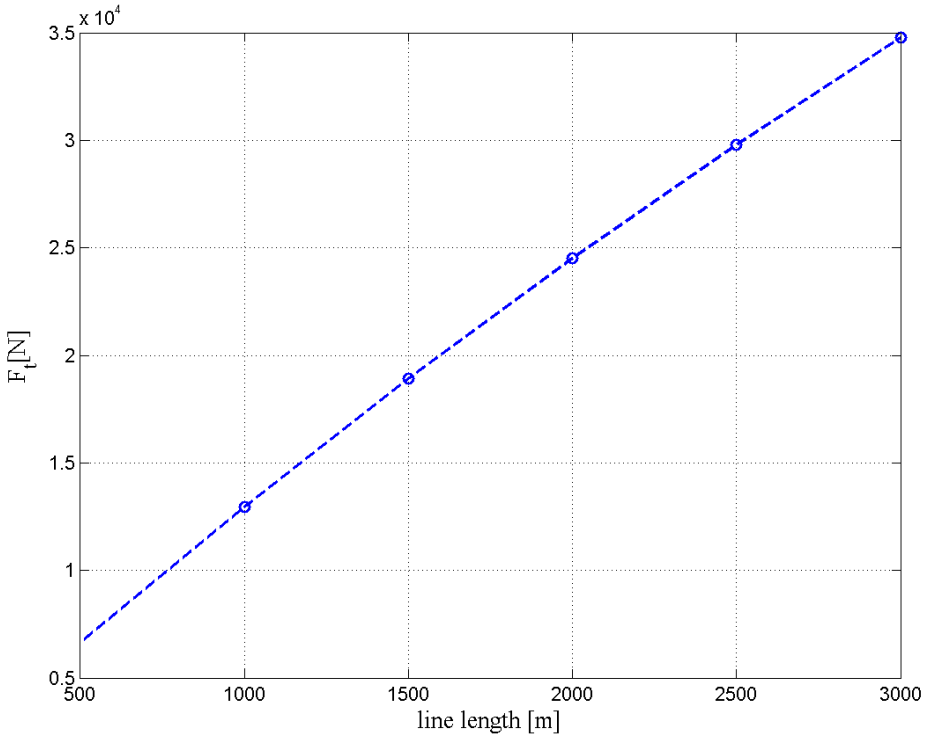

Fig. 4.8: Aerodynamic drag force of one straight cable of d=11 mm for different cable lengths as the kite flies at constant velocity $V_k = 80m/s$

4.2 Flexible ropes

In this section, the major contribution of this thesis is presented: the dynamic study of the tether. The need of this kind of analysis has arisen due to experimental observations during the operations of a KiteGen system. In particular, it has been noticed that the rope configuration during the flight strongly differs from that of a straight line. It has been seen, instead, that the rope tends to follow the kite motion mainly with its highest part, while the main part of the rope tends to stay quieter approximately close to axis of the trajectory. This different behavior may have huge impact on the evaluation of the aerodynamic drag force generated from the cables and therefore on the power output of the system.

In this analysis, therefore, the position of the rope during the flight is not preassigned, as well as the velocity of each element of the rope, but it will be found solving a dynamic system accounting for the main forces acting on the rope during the flight. Moreover, in this analysis, some more realistic conditions will be added: the unrolling of cables from the drum and the trajectory performed by the kite.

Applying the Newton's second law to the rope, considering the weight force, the aerodynamic drag force and the tension variation along the rope, the following vector equation per unit length is found:

$$\mu\,\bar{a} = \frac{d\bar{T}}{ds} + \bar{w} + \bar{f_t} \qquad (4.7)$$

where $\mu\left[\frac{kg}{m}\right]$ is the linear density of the rope, $\bar{a}$ is its acceleration, s is the curvilinear abscissa identifying a specific position along the rope, $\bar{w}$ is the weight of the tether per unit length, $\bar{f_t}$ is the aerodynamic resistance of tether per unit length and $\bar{T}$ is the variable tension along the tether. In particular, the vector tension $\bar{T}$ is expressed as $\bar{\tau}$, where T is the intensity of the tension and $\bar{\tau}$ the tangential unit vector along the line element.

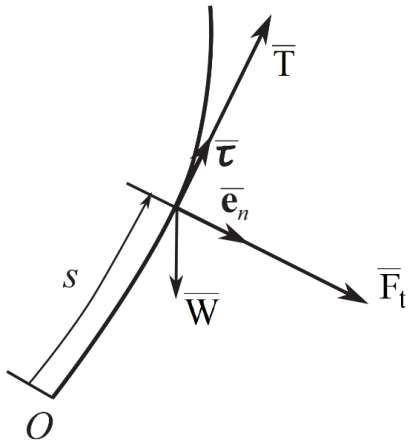

Fig. 4.9: A portion of the rope with the force considered in the dynamic system: $\bar{W}$ is the gravity force, $\bar{F_t}$ is the aerodynamic drag force of the cable, $\bar{T}$ is the tension, O identifies the beginning of the rope and s the position along the rope. Picture based on picture from [40].

The unit vector $\bar{\tau}$ is now needed since the cable is not considered anymore straight and therefore $\bar{\tau}(s) \neq \bar{e}_r$. In particular, the components of $\bar{\tau}$ in the (x, y, z) coordinate system are:

$$\bar{\tau} = \left(\frac{\partial x}{\partial s} \quad \frac{\partial y}{\partial s} \quad \frac{\partial z}{\partial s}\right) \qquad (4.8)$$

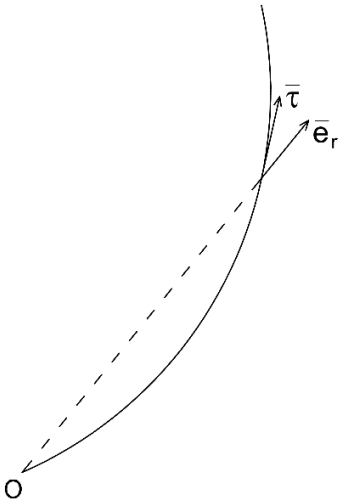

Fig. 4.10: Difference between the unit vectors $\bar{\tau}$ and $\bar{e}_r$.

Following [40], the tether aerodynamic resistance of a discretized piece of the cable Δs is computed considering the component of the effective velocity that is normal to the tether

surface $\bar{V}_n$. In particular, $\bar{V}_n$ is function of the considered position along the rope, i.e. $\bar{V}_n = \bar{V}_n(s)$. Therefore:

$$\bar{F}_{t,\Delta s}(s) = \frac{1}{2}\,\rho(z)\; d_c\; \Delta s\; C_{d,c}(Re)\; |\bar{V}_n(s)|\; \bar{V}_n(s) \qquad (4.9)$$

where, as already done in the previous analysis, $\rho(z)$ is the air density, function of the altitude z, d_c is the constant line diameter and $C_{d,c}$ is the normal drag coefficient of a cylinder, evaluated as function of the variable Reynolds number along the line $Re = Re(s)$. Specifically, the Reynolds number has been computed using the velocity $|\bar{V}_n(s)|$ and a value of the air viscosity μ_{air} function of the altitude z:

$$Re(s) = \frac{\rho(z)\; V_n(s)\, d_c}{\mu_{air}(z)} \qquad (4.10)$$

The vector $\bar{V}_n(s)$ can be found as:

$$\bar{V}_n(s) = V_e(s)\cos\big(\Delta\beta(s)\big)\; \bar{e}_n \qquad (4.11)$$

where $\bar{e}_n$ in this case can be found considering that it has to belong to the plane $(\bar{x}_w, \bar{\tau})$ and has to be normal to $\bar{\tau}$, while $\Delta\beta(s)$ is the angle, function of the position along the rope s, between the direction of $\bar{\tau}$ and the direction normal to $\bar{V}_e$. Therefore, it can be found as done for the angle $\Delta\alpha$ in (2.19):

$$\Delta\beta = \arcsin\left(\frac{\bar{\tau}\;\cdot\;\bar{V}_e}{|\bar{V}_e|}\right) \qquad (4.12)$$

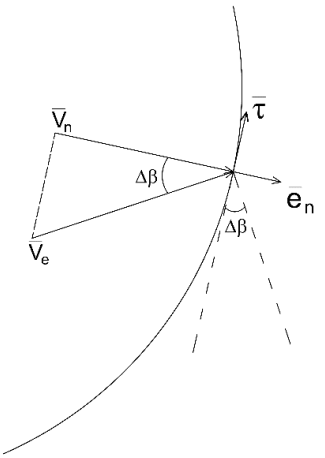

Fig. 4.11: Graphical representation of the angle $\Delta\beta$.

It is now possible to express the vector equation (4.7) in the global coordinate system (x, y, z):

$$\begin{cases} \mu \dfrac{\partial^2 x}{\partial t^2} = \dfrac{\partial}{\partial s}\left(T \dfrac{\partial x}{\partial s}\right) - \dfrac{1}{2}\rho\, d_c\, C_{d,c} \sqrt{V_{n,x}^2 + V_{n,y}^2 + V_{n,z}^2} \cdot \left(V_{n,x}\right) & (4.13) \\ \mu \dfrac{\partial^2 y}{\partial t^2} = \dfrac{\partial}{\partial s}\left(T \dfrac{\partial y}{\partial s}\right) - \dfrac{1}{2}\rho\, d_c\, C_{d,c} \sqrt{V_{n,x}^2 + V_{n,y}^2 + V_{n,z}^2} \cdot \left(V_{n,y}\right) & (4.14) \\ \mu \dfrac{\partial^2 z}{\partial t^2} = \dfrac{\partial}{\partial s}\left(T \dfrac{\partial z}{\partial s}\right) - \mu g - \dfrac{1}{2}\rho\, d_c\, C_{d,c} \sqrt{V_{n,x}^2 + V_{n,y}^2 + V_{n,z}^2} \cdot \left(V_{n,z}\right) & (4.15) \\ \left(\dfrac{\partial x}{\partial s}\right)^2 + \left(\dfrac{\partial y}{\partial s}\right)^2 + \left(\dfrac{\partial z}{\partial s}\right)^2 = 1 & (4.16) \end{cases}$$

with t representing the time and $(V_{n,x}, V_{n,y}, V_{n,z})$ the projections of $\bar{V}_n$ on the (x, y, z) axes. The fourth equation gives instead the dependence of x, y and z to the curvilinear abscissa s. The system of equations previously introduced, describes the system kite-tether as the cable is pulled from the drum by the kite at velocity V_L computed using the already introduced equation

$$F_k = \frac{1}{2}\rho A C_l E^2 \left(1 + \frac{1}{E^2}\right)^{3/2} \left(|\bar{V}_w| \sin(\vartheta(t)) \cos(\phi(t)) - V_L\right)^2 \qquad (4.17)$$

in such a way to keep a constant tension of $150\ kN$ per rope at the generator. The magnitude of the wind velocity $|\bar{V}_w|$ has been evaluated following the average wind profile of De Bilt defined in Chapter 3. Ones again, the kite aerodynamic efficiency E has been used in such a way to explore a wide range of rope lengths. The computed value of the aerodynamic resistance of the two cables will then be used to evaluate a global system aerodynamic efficiency G_e defined as:

$$G_e = \frac{L}{D_k + 2\, F_t} \qquad (4.18)$$

where L is the lift force generated from the kite, D_k is the kite aerodynamic drag and F_t is the aerodynamic drag of one cable. This new global coefficient will finally be used in place of E in order to compute the power output of the global system. It should be highlighted that actually, to the purpose of evaluating the cable aerodynamic resistance, the magnitude of the reel-out velocity $\bar{V}_L$ is of no importance since $\bar{F}_t$ is evaluated using $\bar{V}_n$.

During the simulations, the kite is performing an eight-shaped trajectory with average polar angle $\vartheta = 45°$ and width of roughly $190\ m$, flying at constant transversal velocity $V_k = 80\ m/s$.

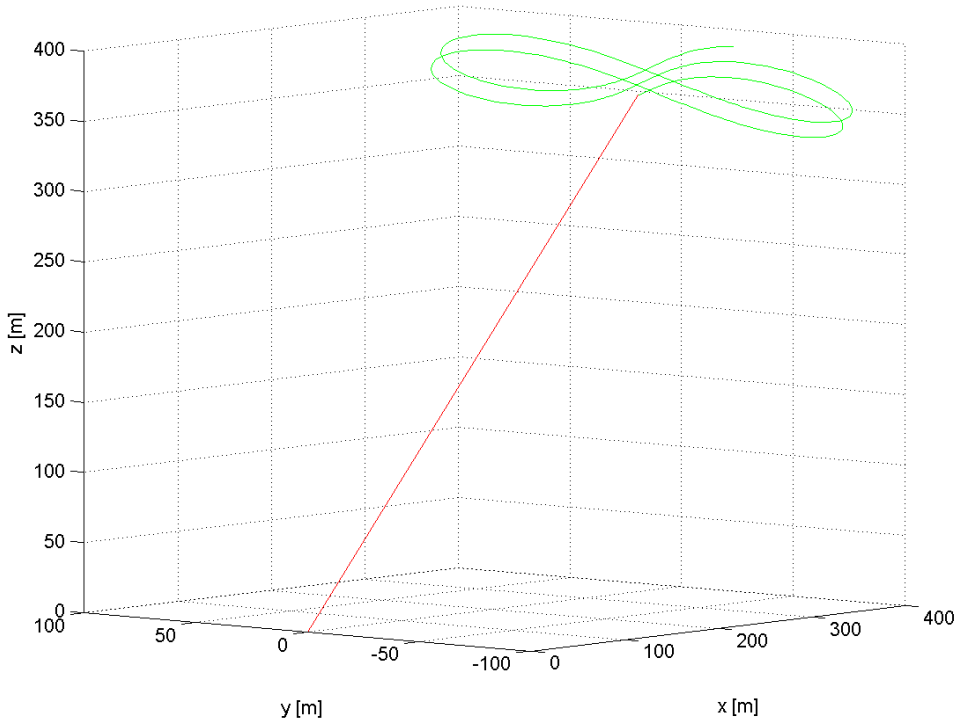

Fig. 4.12: In green: a small portion of the trajectory performed by the kite during the flight during the simulated flight. In red: initial configuration of the rope.

The system described has as unknowns $x(s,t), y(s,t), z(s,t)$ and $T(s)$ and is therefore a problem to be solved both in space and in time. In order to solve it, *boundary conditions* and *initial conditions* are required.

Regarding the initial configuration of the system, it is assumed that the rope at the beginning has length $L_0 = 500\ m$. The *initial conditions* concerning the spatial coordinates and the corresponding velocities are set as:

$$\begin{cases} x(s,t_0) = s\sin\big(\vartheta(s,t_0)\big) \\ y(s,t_0) = 0 \\ z(s,t_0) = s\cos\big(\vartheta(s,t_0)\big) \end{cases} \qquad (4.19)$$

$$\begin{cases} \dfrac{\partial x}{\partial t}(s,t_0) = V_L(t_0)\sin\big(\vartheta(s,t_0)\big) + s\,\dot{\vartheta}(s,t_0)\cos\big(\vartheta(s,t_0)\big) \\ \dfrac{\partial y}{\partial t}(s,t_0) = s\,\dot{\phi}(s,t_0)\sin\big(\vartheta(s,t_0)\big) \\ \dfrac{\partial z}{\partial t}(s,t_0) = V_L(t_0)\cos\big(\vartheta(s,t_0)\big) - s\,\dot{\vartheta}(s,0)\sin\big(\vartheta(s,t_0)\big) \end{cases} \qquad (4.20)$$

where t_0 is the initial time, $V_L(t_0)$ is initial value of the reel out velocity set in order to have the tension on the cable in correspondence of the kite slightly higher than the value of the tension of the cable at the drum, $\vartheta(s,t_0)$ is the initial polar angle set equal to $45°$ for the whole rope, $\dot{\vartheta}(s,t_0)$ and $\dot{\phi}(s,t_0)$ are the initial angular velocities, obtainable from the fact that the trajectory of the kite is known. The initial configuration of the rope considers therefore simply a straight line laying on the (x,z) plane, i.e. $\phi(s,t_0) = 0$.

The *boundary conditions*, instead, consider that the first node of the rope stays at constant position $(x, y, z) = (0,0,0)$ and that the tension at the same node is kept at the constant value of $T_0 = 150\ kN$ per rope. The position of the last node of the rope coincides instead with the kite position during the flight. The value of $T_0 = 150\ kN$ per rope at the generator is chosen considering a design mean power output of the machine of $3MW$. For this purpose, it is considered that the maximum reel out velocity is approximately equal to $13.5\ m/s$ and therefore during the active phase the maximum power is of $4MW$.
The problem is solved by discretizing both space s and time t and approximating the derivatives with the finite difference approach. In particular, space is discretized using the Method of the Central Differences, while time is discretized using the Implicit Euler Method. Moreover, since the Euler Method is suitable for a first order derivative in time, three auxiliary variables are introduced:

$$\begin{aligned} X_v &= \frac{\partial x}{\partial t} \\ Y_v &= \frac{\partial y}{\partial t} \\ Z_v &= \frac{\partial z}{\partial t} \end{aligned} \qquad (4.21)$$

As example, it is shown how equation *(4.13)* becomes after the discretization.

$$\mu\ \frac{\partial^2 x}{\partial t^2} = \frac{\partial}{\partial s}\left(T\frac{\partial x}{\partial s}\right) - \frac{1}{2}\rho\ d_c\ C_{d,c}\sqrt{V_{n,x}^2 + V_{n,y}^2 + V_{n,z}^2}\cdot\left(V_{n,x}\right)$$

$$\mu\ \frac{\partial^2 x}{\partial t^2} = \frac{\partial T}{\partial s}\frac{\partial x}{\partial s} + T\frac{\partial^2 x}{\partial s^2} - \frac{1}{2}\rho\ d_c C_{d,c}\ \sqrt{V_{n,x}^2 + V_{n,y}^2 + V_{n,z}^2}\cdot\left(V_{n,x}\right)$$

$$\mu\ \frac{\partial X_v}{\partial t} = \frac{\partial T}{\partial s}\frac{\partial x}{\partial s} + T\frac{\partial^2 x}{\partial s^2} - \frac{1}{2}\rho\ d_c\ C_{d,c}\sqrt{V_{n,x}^2 + V_{n,y}^2 + V_{n,z}^2}\cdot\left(V_{n,x}\right)$$

$$\mu\ \frac{X_{v,i}^n - X_{v,i}^{n-1}}{\Delta t} = \left[\frac{T_{i+1} - T_{i-1}}{2\Delta s}\cdot\frac{x_{i+1} - x_{i-1}}{2\Delta s} + T_i\frac{x_{i+1} - 2x_i + x_{i-1}}{\Delta s^2} + \right.$$
$$\left. - \frac{1}{2}\rho\ d_c\ C_{d,c}\sqrt{V_{n,x,i}^2 + V_{n,y,i}^2 + V_{n,z,i}^2}\cdot\left(V_{n,x,i}\right)\right]^n$$

where the subscript i identifies the i^{th} node of the discretized rope, while the apices n and $(n-1)$ represent respectively the new time step and the old time step due to the discretization of the time. For each time step and for each of the four equations of the system, there are therefore m equations to solve, one for each node of the rope.
Then $X_v = \frac{\partial x}{\partial t}$ for the n^{th} time step becomes $X_{v,i}^n = \frac{x_i^n - x_i^{n-1}}{\Delta t}$, while for the aerodynamic resistance force the Frozen Coefficient Method is applied. This method may be used, like in this case, when there are some variables, here the velocities, that change slower than others, here the tension, and therefore that part of the equation can be evaluated at the $(n-1)^{th}$ time step instead of the n^{th} time step. In this way, the non-linear part of the equation becomes known. Considering for example equation *(4.13)* ones that the distribution of T over the rope is also known, it is possible to write the system of m equation in the matricial form:

$$\boldsymbol{A_m}\,\bar{\boldsymbol{x}}_{\boldsymbol{m}} = \bar{\boldsymbol{b}}_{\boldsymbol{m}}$$

where $\boldsymbol{A_m}$ is a sparse tridiagonal matrix having non zero elements only on the diagonal, on the super-diagonal and on the sub-diagonal, corresponding for each equation at the nodes x_{i-1}, x_i, x_{i+1}, $\bar{\boldsymbol{b}}_{\boldsymbol{m}}$ is the vector of the known terms (the ones evaluated at the $(n-1)^{th}$ time step) and $\bar{\boldsymbol{x}}_{\boldsymbol{m}}$ is the vector of the unknowns, i.e. the x components of the position of the m nodes of the rope. It is then possible to find:

$$\bar{\boldsymbol{x}}_m = \boldsymbol{A_m} \backslash \bar{\boldsymbol{b}}_m$$

However, the distribution of T is not known since it is one of the results of the simulation and therefore an iterative method is needed. In particular, the *Gauss-Seidel method* is used. The algorithm used may be summarized as follows:

1. for equations *(4.13)* and *(4.14)* a guess distribution of T at the time n is assumed. For example, for the first iteration of the first time step it is assumed that T varies linearly from $T_0 = 150\ kN$ to $T_1 = 1.1 \cdot T_0$, where T_1 is the unknown value of the tension in correspondence of the kite. For the first iteration of the following time steps, instead, it is assumed as guess value the distribution of T at the previous time step;
2. with this T distribution, the values of x and y of each node at the n^{th} time step are calculated from eq. *(4.13)* and *(4.14)*;
3. from eq. *(4.16)* the values of z of each node at the n^{th} time step are calculated;
4. knowing the computed x, y and z distributions it is possible, from equation *(4.15)*, to compute a new distribution of T;
5. a *relaxed solution* of the found T is computed;
6. a curve which approximates the values of the relaxed solution and passes through the value T_0 is then computed;
7. come back to the step 2 using the approximation curve as T distribution until the convergence (with a tolerance on the relative error of 10^{-5}) is reached.

The Successive Over-Relaxation (SOR) method, used at the 5^{th} step of the algorithm, is a variant of the Gauss-Seidel Method in which at each step the solution used at the iteration $j+1$, let us call it x_{j+1}^{SOR}, is not directly the computed solution at the previous step, $f(x_j^{SOR})$, but:

$$x_{j+1}^{SOR} = (1-\omega)x_j^{SOR} + \omega\, f(x_j^{SOR}) \qquad (4.22)$$

where ω is a positive real number. If $\omega > 1$ the method speeds up the convergence, while if $\omega < 1$ the method helps to establish convergence. In this case it was chosen to use an $\omega < 1$. The choice of adding the 6^{th} step to the algorithm, instead, was done in order to give at the new iteration a smooth distribution of T.
The difference between the computed solution, the over-relaxed solution and its data fitting curve is here plotted for the first iteration, after 35 iterations and after 50 iterations. As it

may be noticed, the procedure allows to move towards the convergence of the solution, that after 50 iterations the three curves practically coincide.

(a)

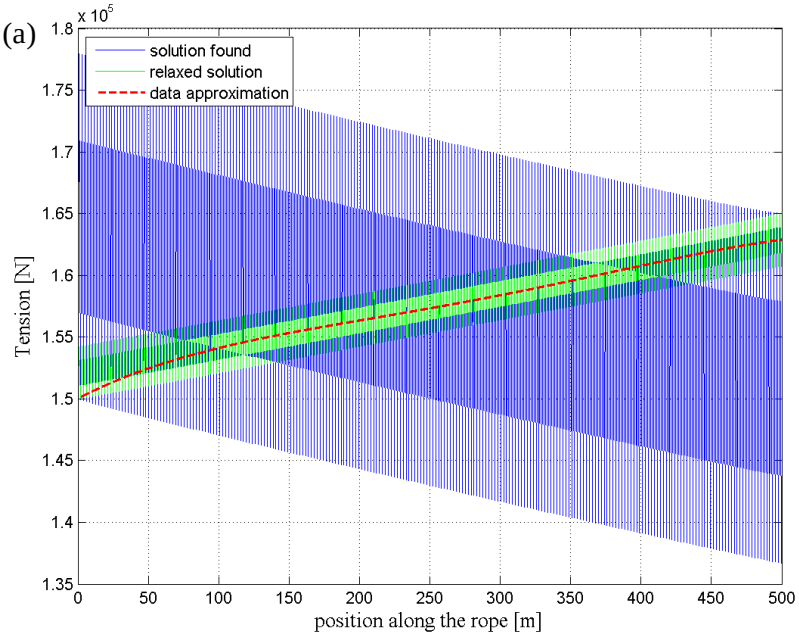

(b)

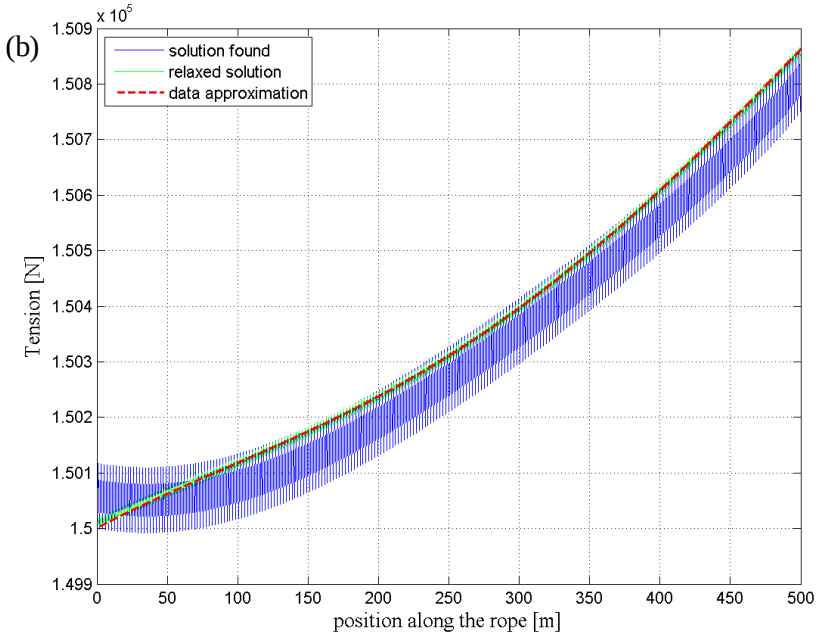

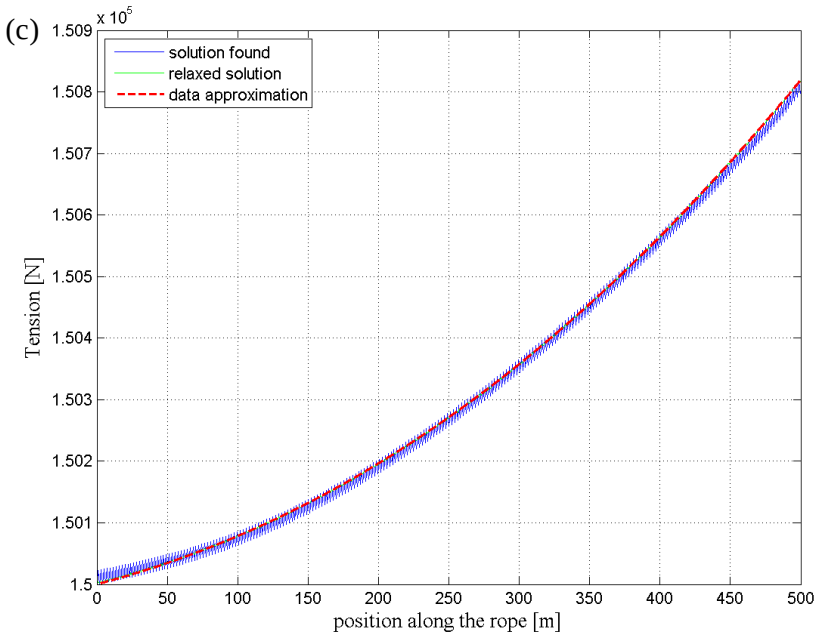

Fig. 4.13: comparison between the computed solution (in blue), the relaxed solution (in light green) and the approximation curve (in dashed red) at the first iteration (a), at the 35^{th} iteration (b) and at the 50^{th} iteration (c) of the algorithm used to find the tension along the rope at the first time step.

Furthermore, it is important to underline that the convergence is always checked on the computed solution of T coming from equation *(4.15)* (and not on the relaxed solution or neither on its approximation curve) and that this is the distribution of T stored as result at the end of the iterative method. Finally, the relative error used at the 7^{th} step of the algorithm is the highest between the relative errors of the four computed results, i.e. the distributions of x, y, z and T.

Using this approach, a tension distribution with this shape is found:

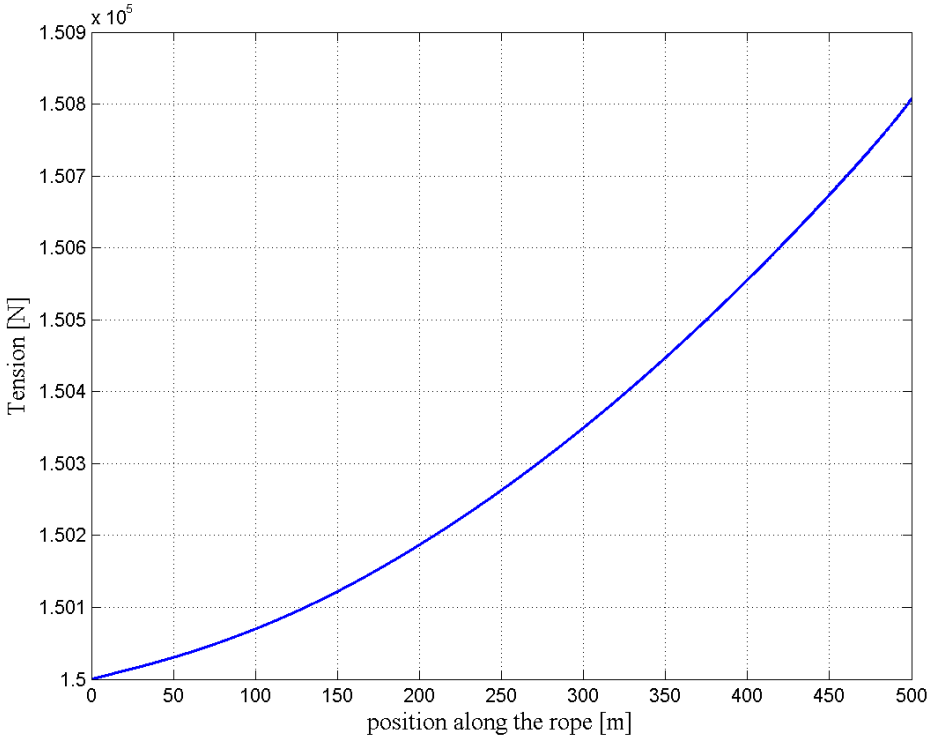

Fig. 4.14: tension distribution along a 500m long inelastic rope with d=11mm.

At this point a convergence study was performed in order to establish how small the quantities Δs and Δt should be. In particular, at each integration step the quantity Δt was chosen accordingly to the value of the reel-out velocity V_L, in such a way make born a constant finite numbers of nodes as the cable is unrolling from the drum. Therefore, since V_L will increase with time, this means that at each new integration step Δt becomes smaller and smaller. Checking, then, the convergence at the initial time, i.e. when the rope is $500m$ long, means checking it at the most conservative situation because, as the algorithm goes on, the convergence can only be improved.

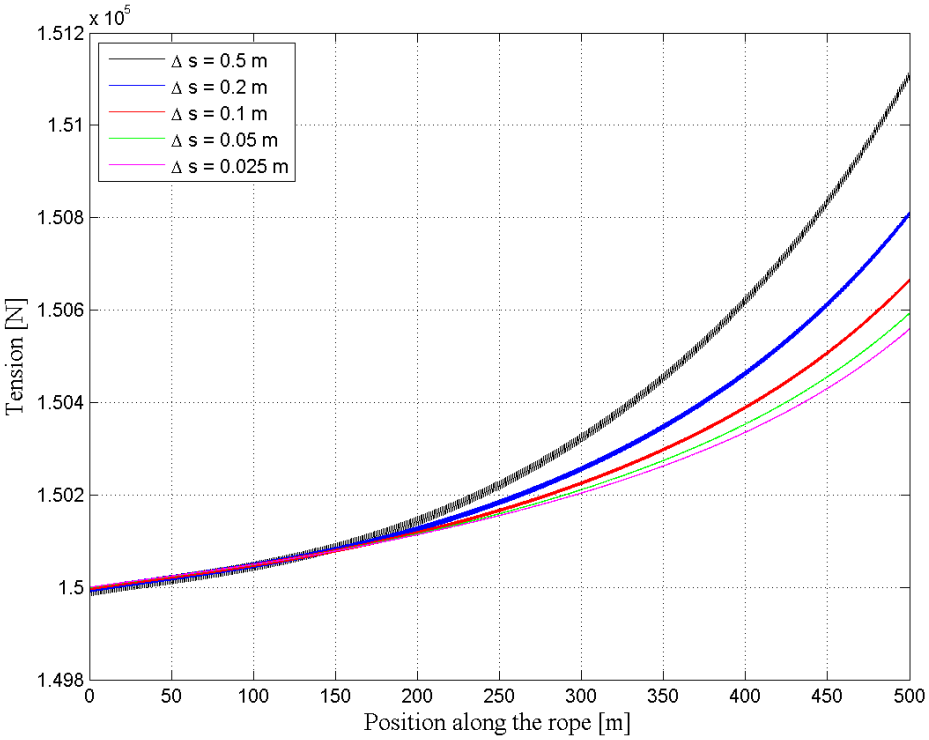

Fig. 4.15: Tension distribution computed along a $500m$ *long rope with:* $\Delta s = 0.5m$ *and* $\Delta t = 0.439$ *sec (in black);* $\Delta s = 0.2m$ *and* $\Delta t = 0.171$ *sec (in blue);* $\Delta s = 0.1m$ *and* $\Delta t = 0.085$ *sec (in red);* $\Delta s = 0.05m$ *and* $\Delta t = 0.042$ *sec (in green);* $\Delta s = 0.025m$ *and* $\Delta t = 0.021$ *sec (in magenta).*

Looking at Fig. 4.15, and considering the computational time needed to perform the simulation, it was decided that the solution found with $\Delta s = 0.05m$ was accurate enough. Once that the method was established, it was decided to perform the simulation for a longer time, in order to evaluate the variation with the length of the cable of the tension distribution, line position, line velocity distribution and aerodynamic resistance of the cable itself. In the following, the results computed for some characteristic lengths of the cable and kite position along the trajectory will be shown. In particular, the more interesting situations to consider are when the kite is at the end of the "straight" part of its trajectory (the longest side of the eight) and when the kite has just done its change of direction. The cable lengths for which the results are shown, instead, are of $1000m$ and $2000m$.

4.2.1 Results for a 1000m long cable

Whit an approximately $1000m$ long rope, it is possible to notice that the rope configuration slightly starts to differ from that of a straight line. In particular, as expected, the lowest part of the line tends to stay closer to the trajectory axis. This means that the polar angle ϑ of the lowest part of the line tends to the average value of $45°$, while the azimuth angle ϕ of the same portion of the cable tends to stay closer to the average value of $0°$. This behavior, however, given the trajectory dimensions and line length, is still not so dramatic.
In the following, it is shown the cable position (from different points of view) assumed in some characteristic points of the trajectory, the corresponding velocity distribution of the cable and therefore also the computed value of the Reynolds number and of the cable drag coefficient along the rope.

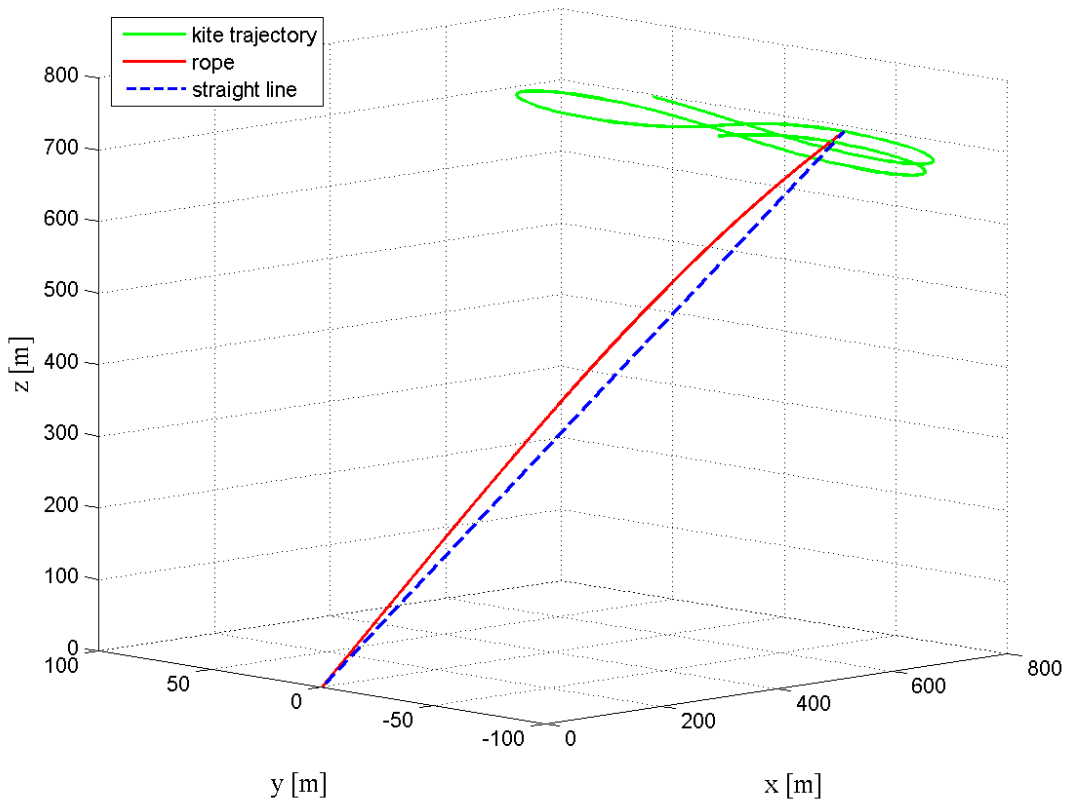

Fig. 4.16: Position assumed by a flexible rope (in red) and by a straight rope (in dashed blue) of length of $1000m$ *when the kite has almost completed the longest side of its trajectory.*

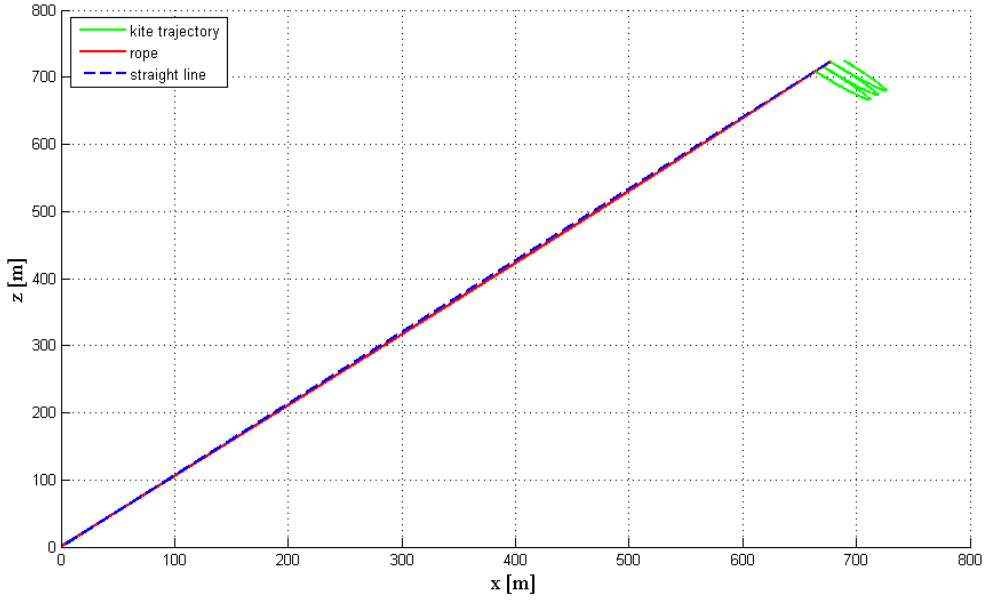

Fig. 4.17: Position assumed by the flexible rope (in red) and by a straight rope (in dashed blue) of length of $1000m$ *when the kite has almost completed the longest side of its trajectory. Side view.*

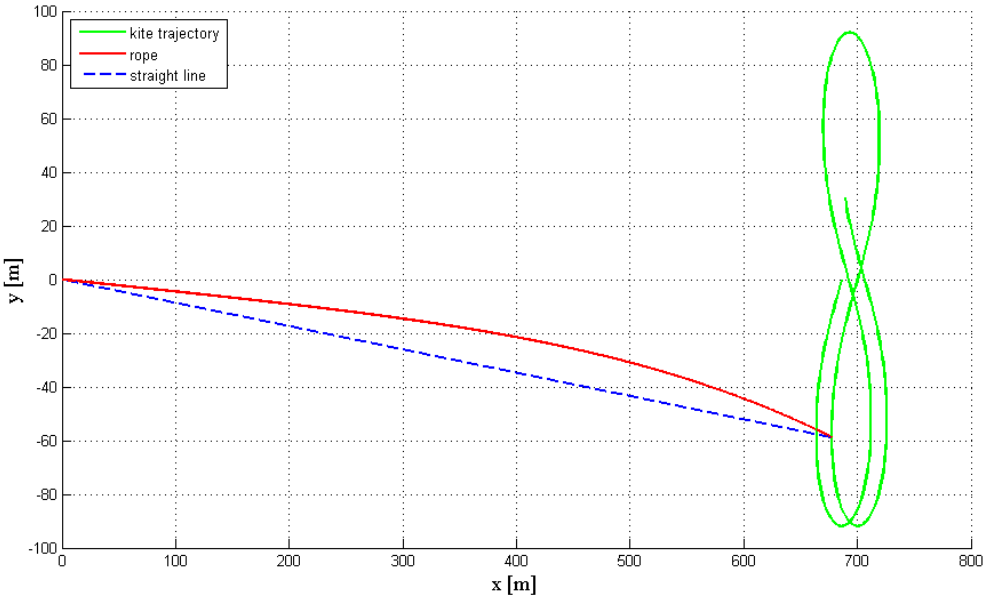

Fig. 4.18: Position assumed by the flexible rope (in red) and by a straight rope (in blue) of length of $1000m$ *when the kite has almost completed the longest side of its trajectory. Top view.*

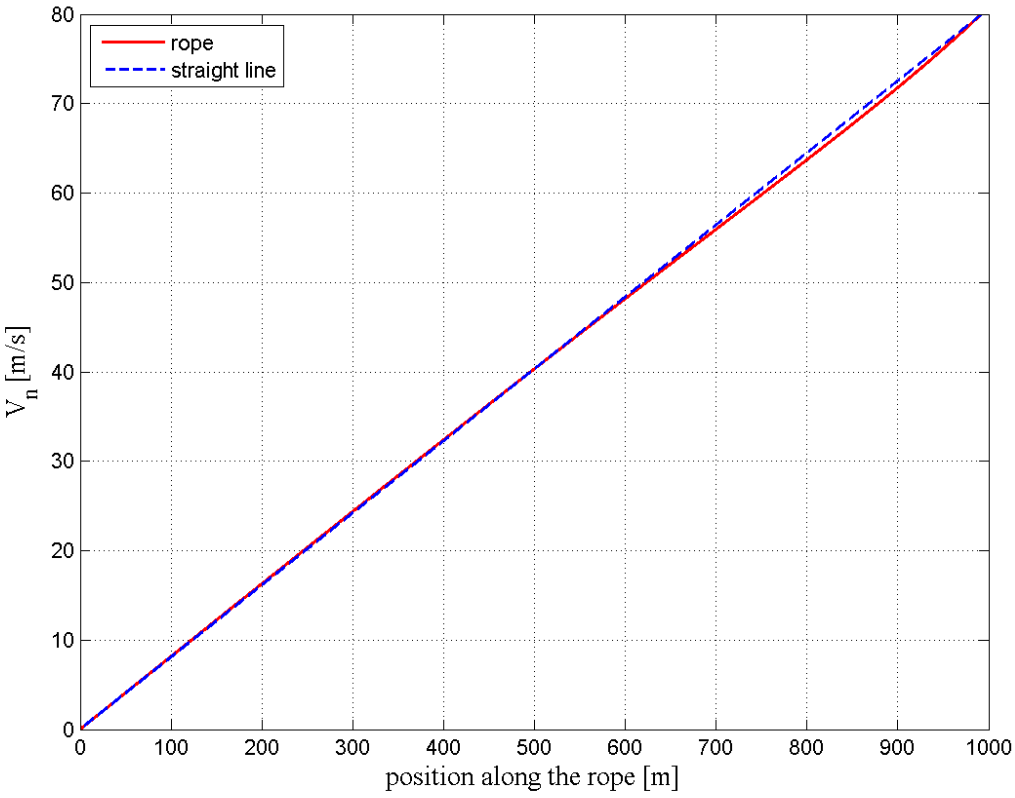

Fig. 4.19: Velocity computed along a flexible rope (in red) and a straight rope (in dashed blue) of length of $1000m$ *when the kite has almost completed the longest side of its trajectory.*

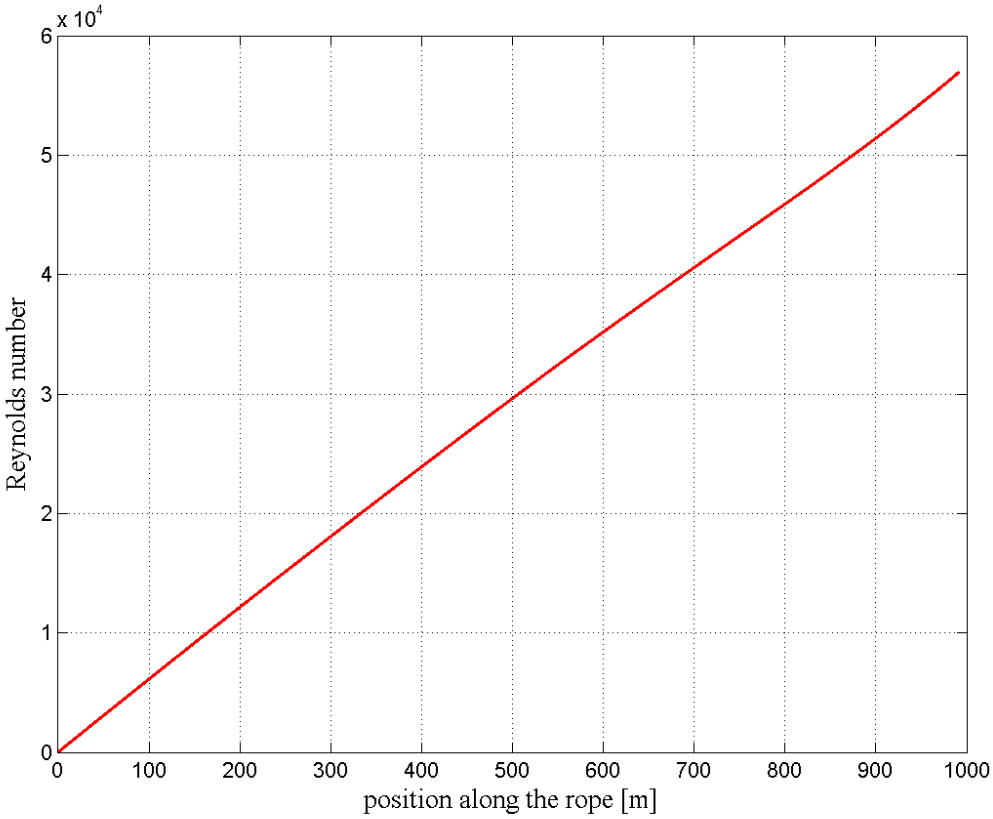

Fig. 4.20: Reynolds number along a flexible rope of length of $1000m$ *when the kite has almost completed the longest side of its trajectory.*

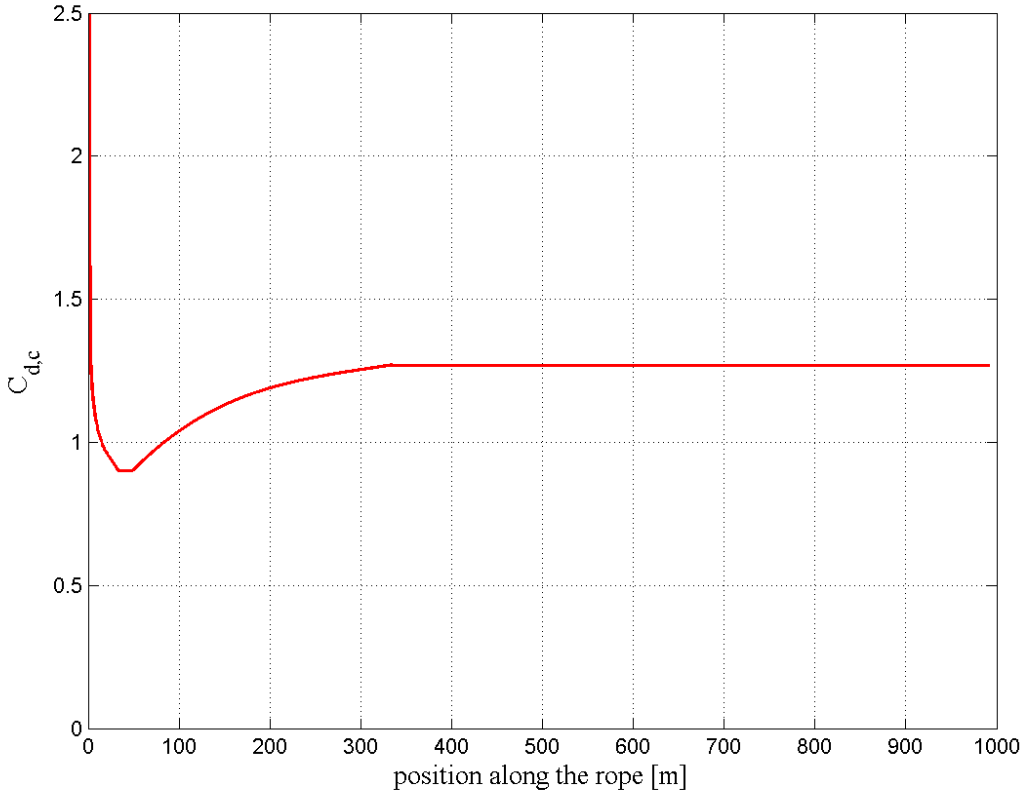

Fig. 4.21: Cable drag coefficient along a flexible rope of length of 1000 m when the kite has almost completed the longest side of its trajectory.

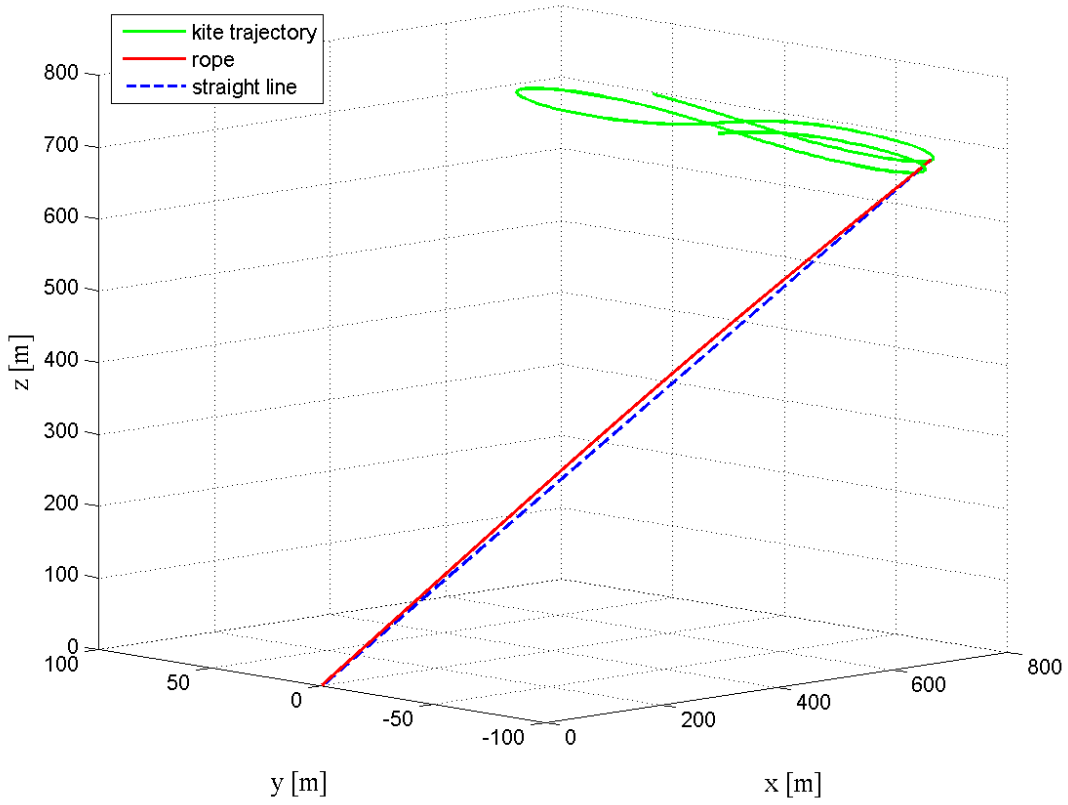

Fig. 4.22: Position assumed by a flexible rope (in red) and by a straight rope (in dashed blue) of length of 1000m when the kite is changing its flight direction.

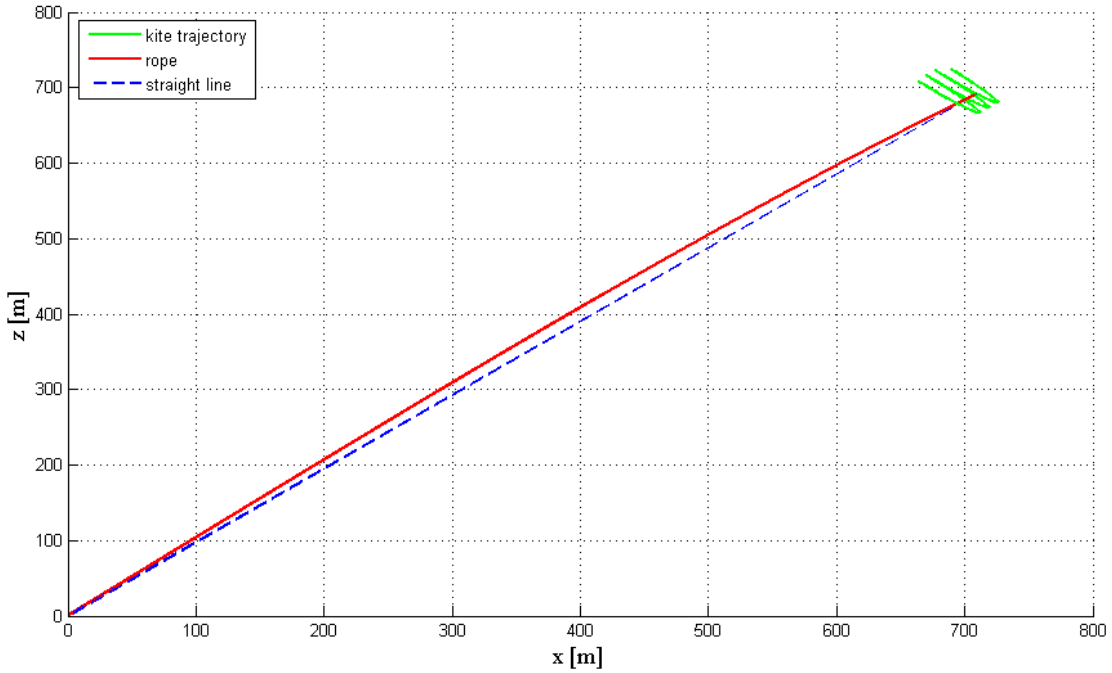

Fig. 4.23: Position assumed by a flexible rope (in red) and by a straight rope (in dashed blue) of length of 1000m when the kite is changing its flight direction. Side view.

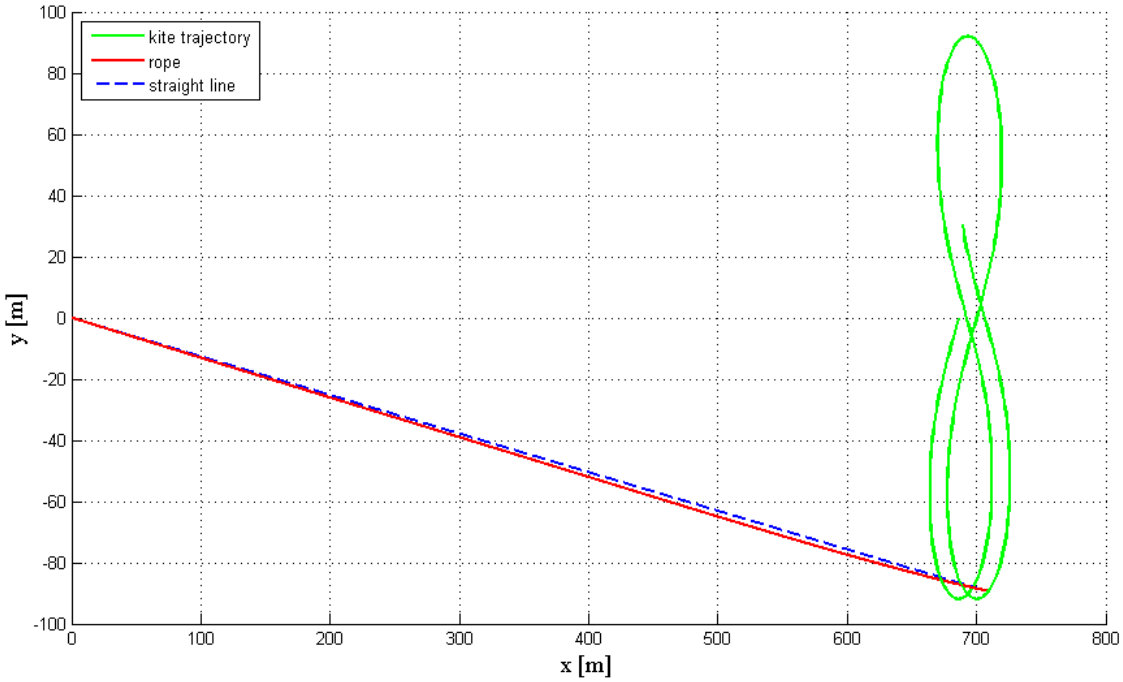

Fig. 4.24: Position assumed by a flexible rope (in red) and by a straight rope (in blue) of length of 1000m when the kite is changing its flight direction. Top view.

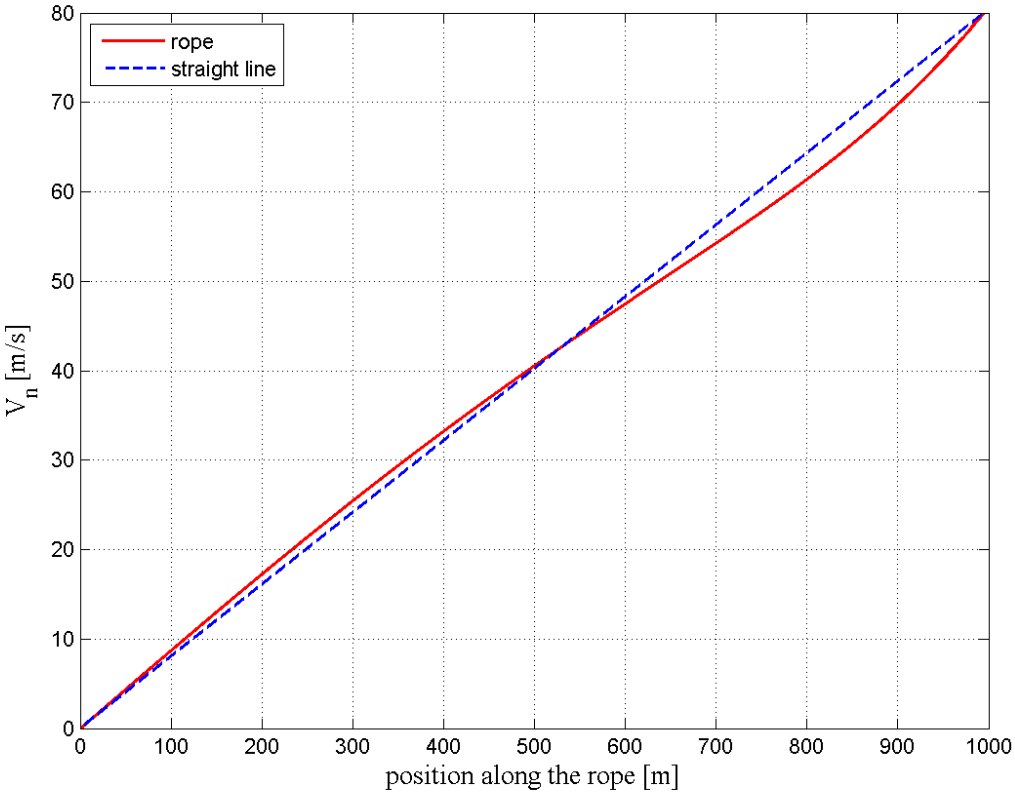

Fig. 4.25: Velocity computed along a flexible rope (in red) and a straight rope (in dashed blue) of length of 1000m when the kite is changing its flight direction.

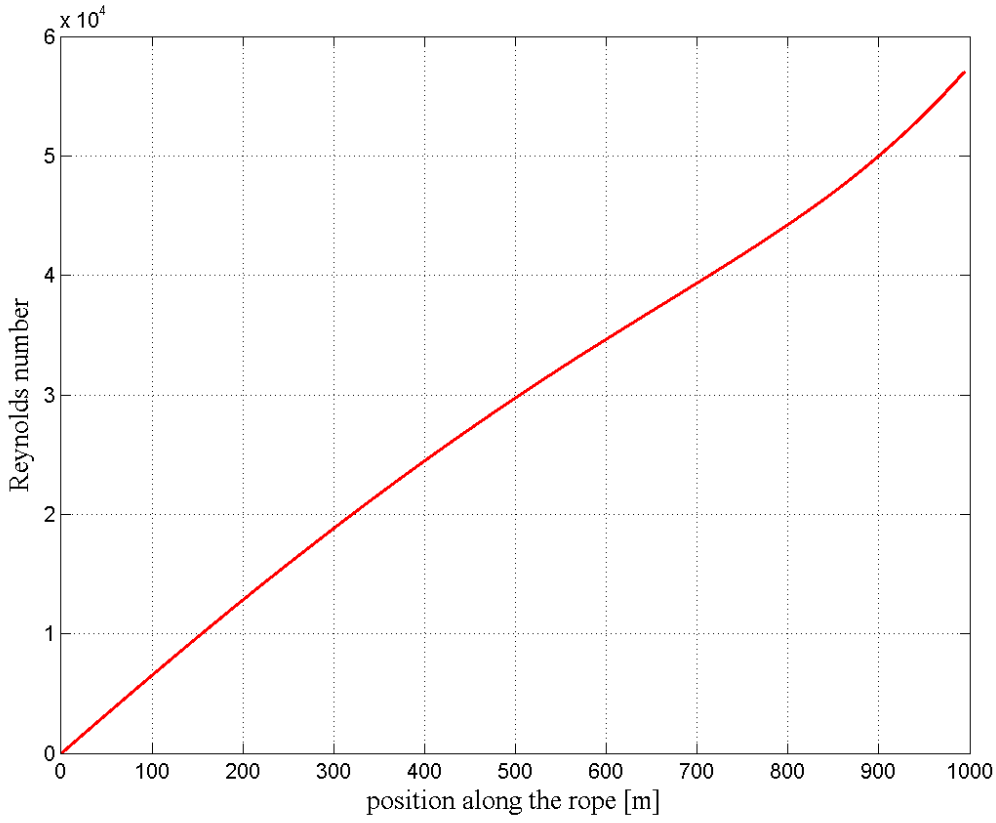

Fig. 4.26: Reynolds number computed along a flexible rope (in red) of length of 1000m when the kite is changing its flight direction.

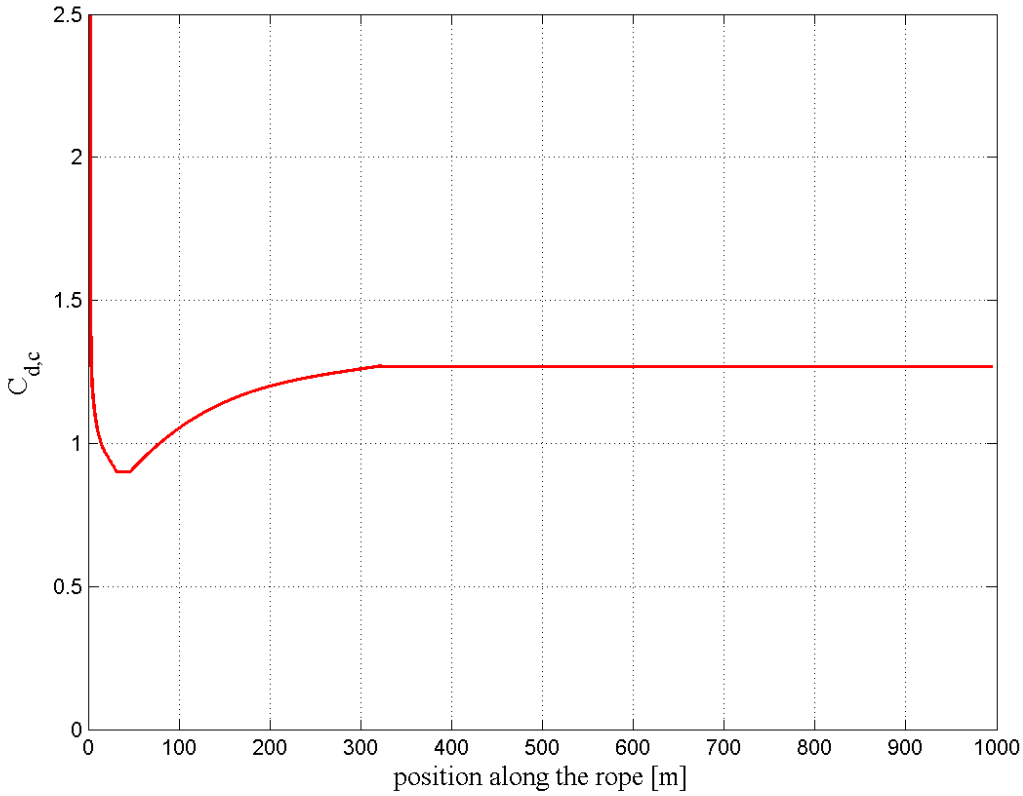

Fig. 4.27: Cable drag coefficient computed along a flexible rope (in red) of length of 1000m when the kite is changing its flight direction.

Concerning the tension distribution, it is found that with an approximately $1000m$ long rope, in order to have a constant tension of $150\ kN$ per rope at the generator, it is necessary to have at the kite a traction force just slightly higher, since the dissipation of force given by the external forces acting on the rope is not so relevant.

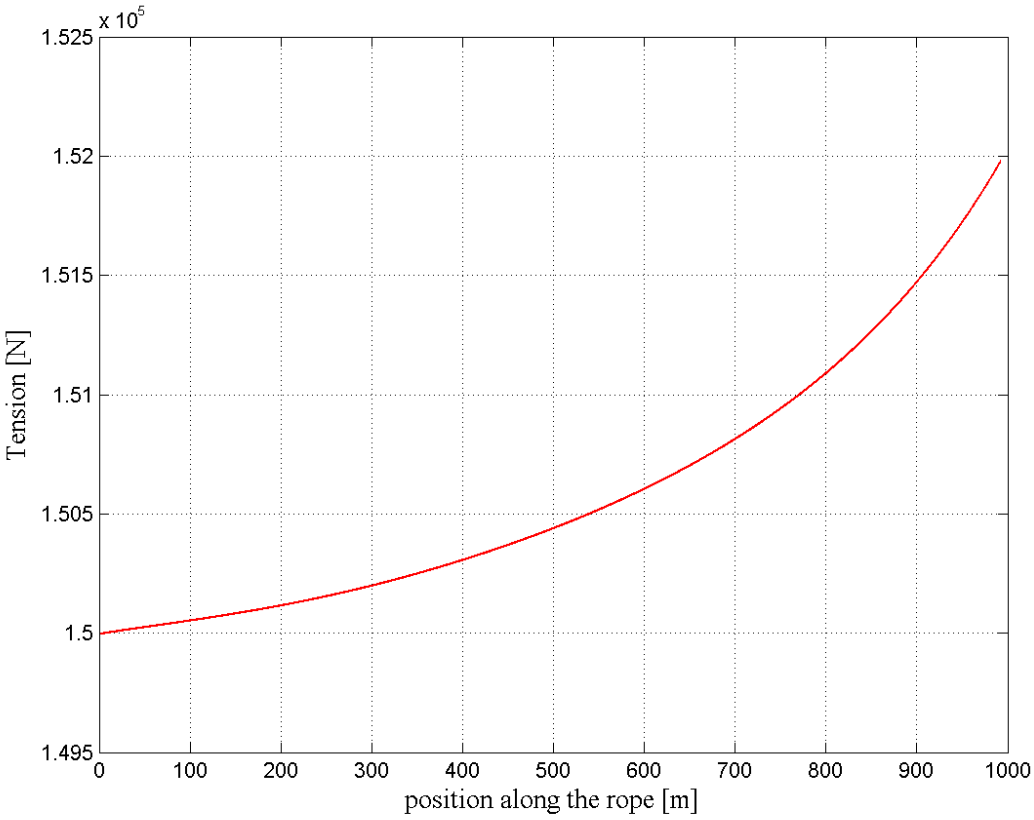

Fig. 4.28: Typical tension distribution computed along a flexible rope (in red) of length of 1000m during the kite flight.

4.2.2 Results for a 2000m long cable

With a $2000m$ long cable, the predicted behavior is fully developed and the rope dynamics strongly differ from those of a straight line.

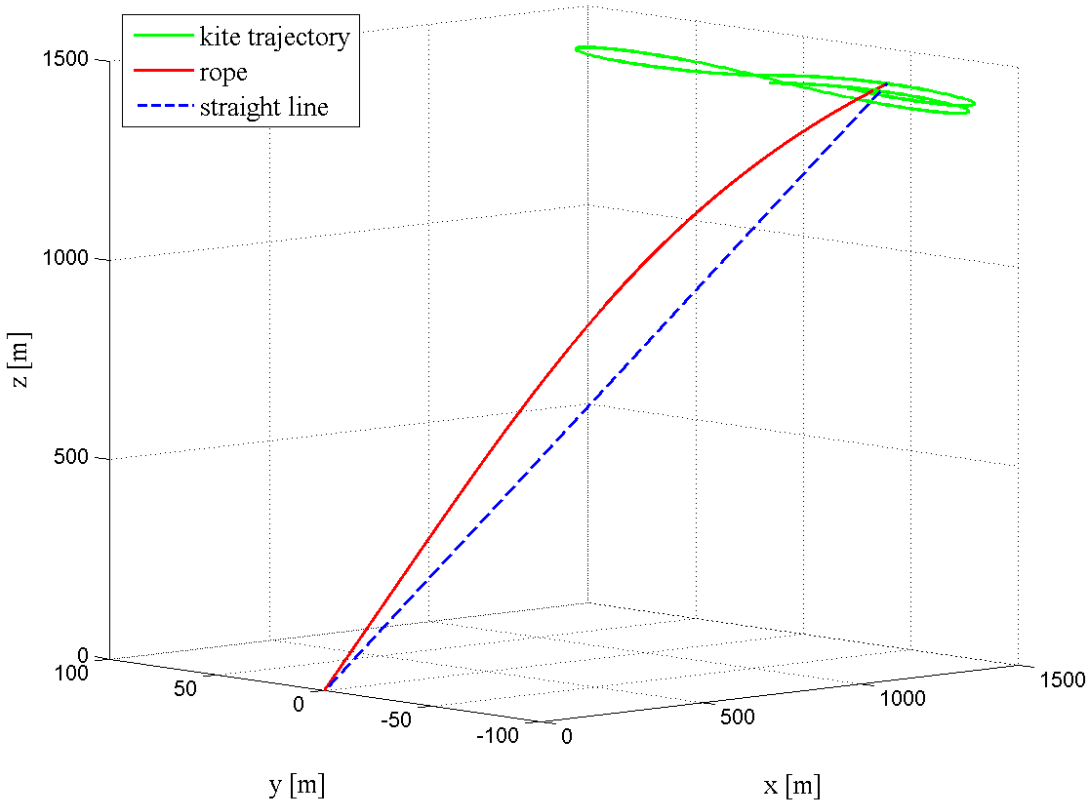

Fig. 4.29: Position assumed by the flexible rope (in red) and by a straight rope (in dashed blue) of length of 2000m when the kite has almost completed the longest side of its trajectory.

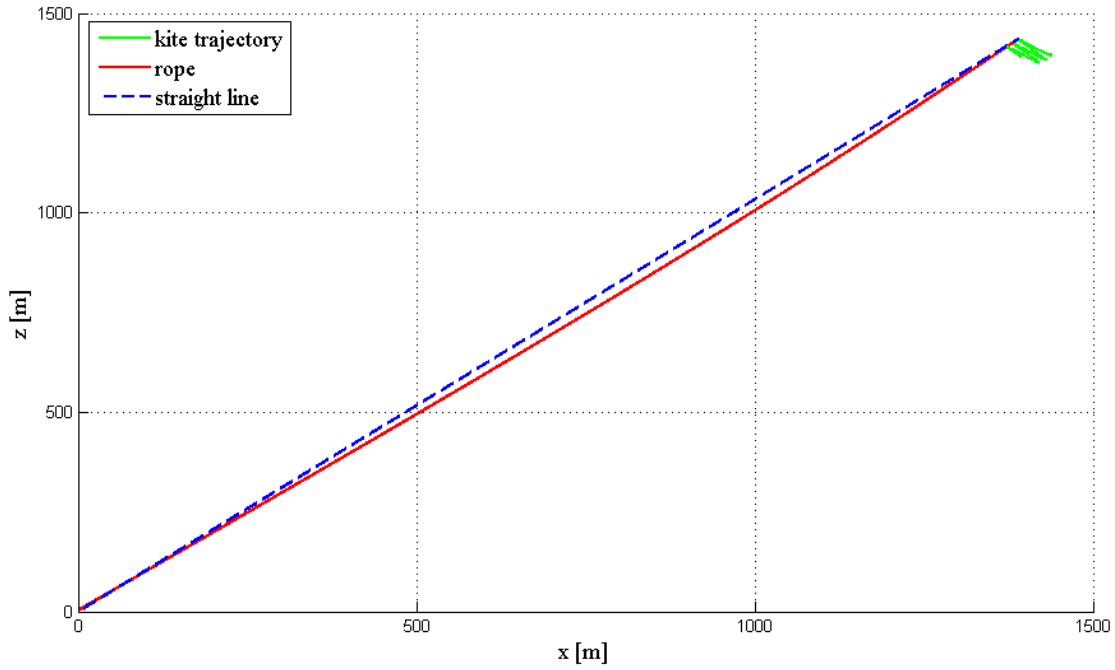

Fig. 4.30: Position assumed by the flexible rope (in red) and by a straight rope (in dashed blue) of length of 2000m when the kite has almost completed the longest part of its trajectory. Side view.

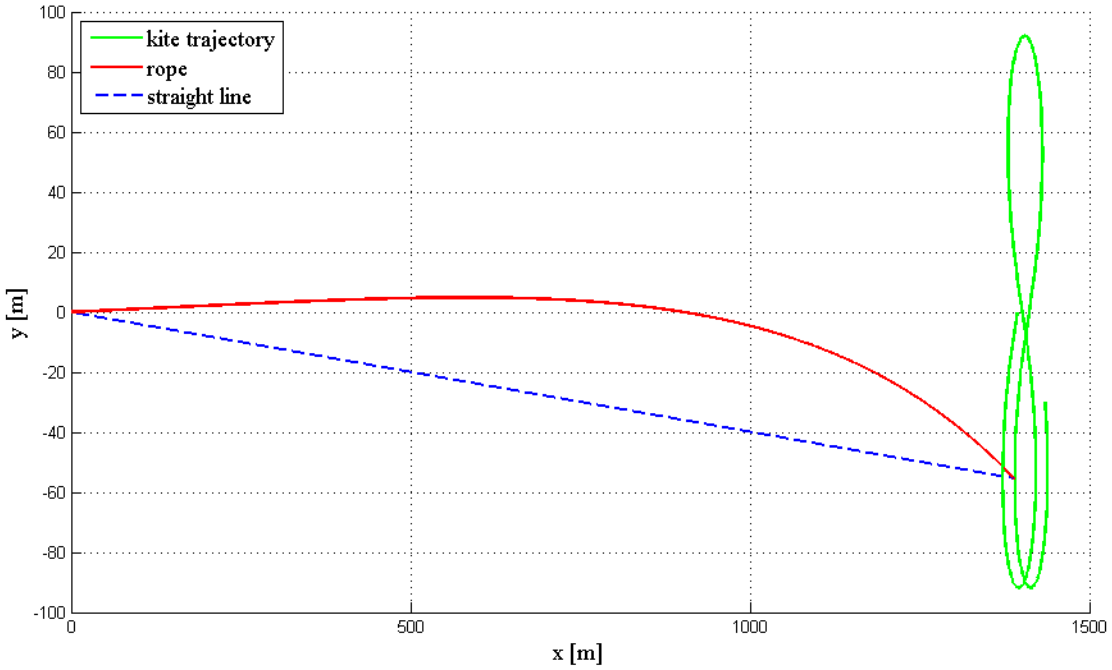

Fig. 4.31: Position assumed by the flexible rope (in red) and by a straight rope (in dashed blue) of length of 2000m when the kite has almost completed the longest part side of its trajectory. Top view.

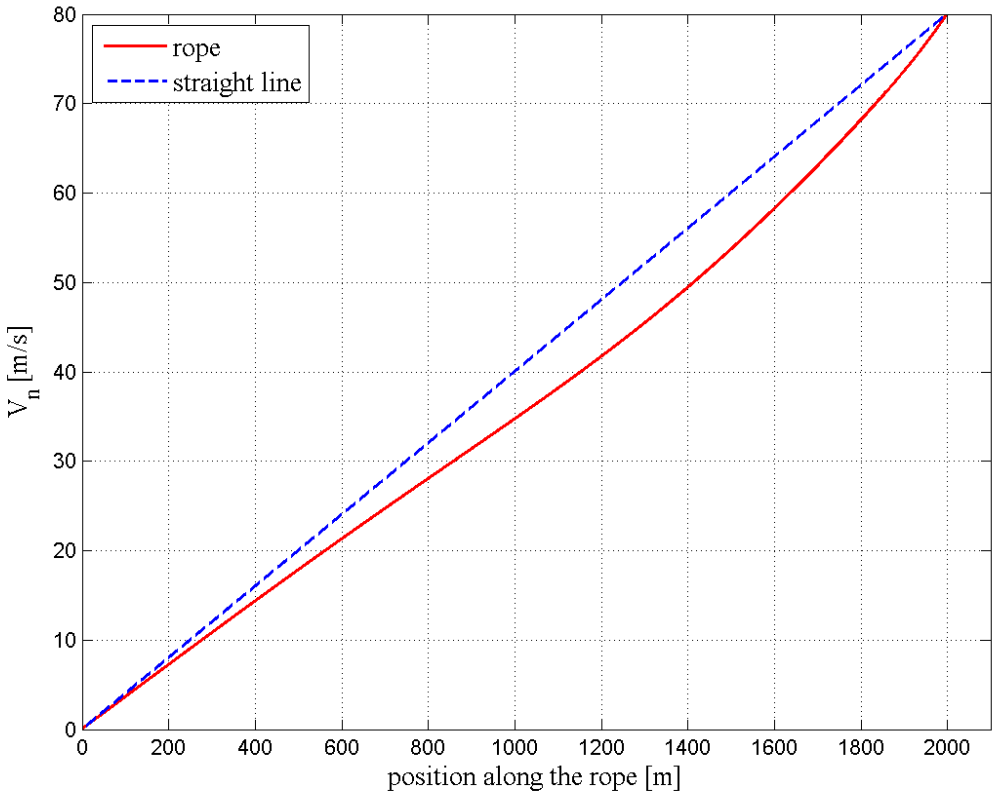

Fig. 4.32: Velocity computed along a flexible rope (in red) and a straight rope (in dashed blue) of length of 2000m when the kite has almost completed the longest side of its trajectory.

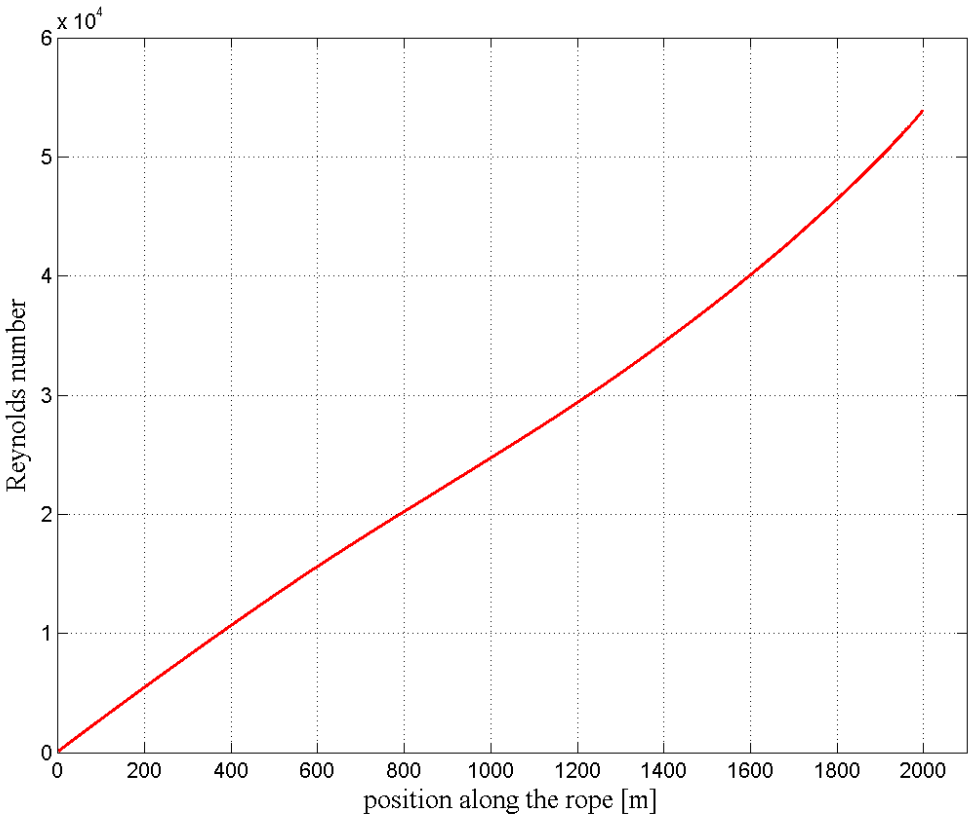

Fig. 4.33: Reynolds number computed along a flexible rope of length of 2000m when the kite has almost completed the longest side of its trajectory.

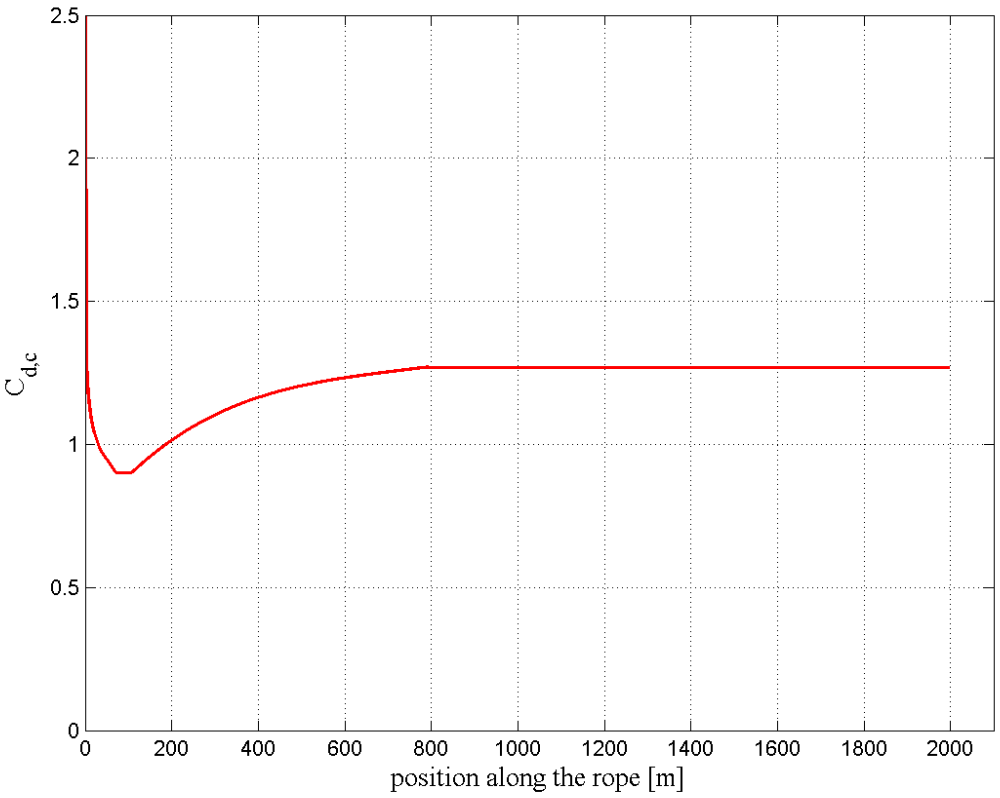

Fig. 4.34: Cable drag coefficient computed along a flexible rope of length of 2000m when the kite has almost completed the longest part side of its trajectory.

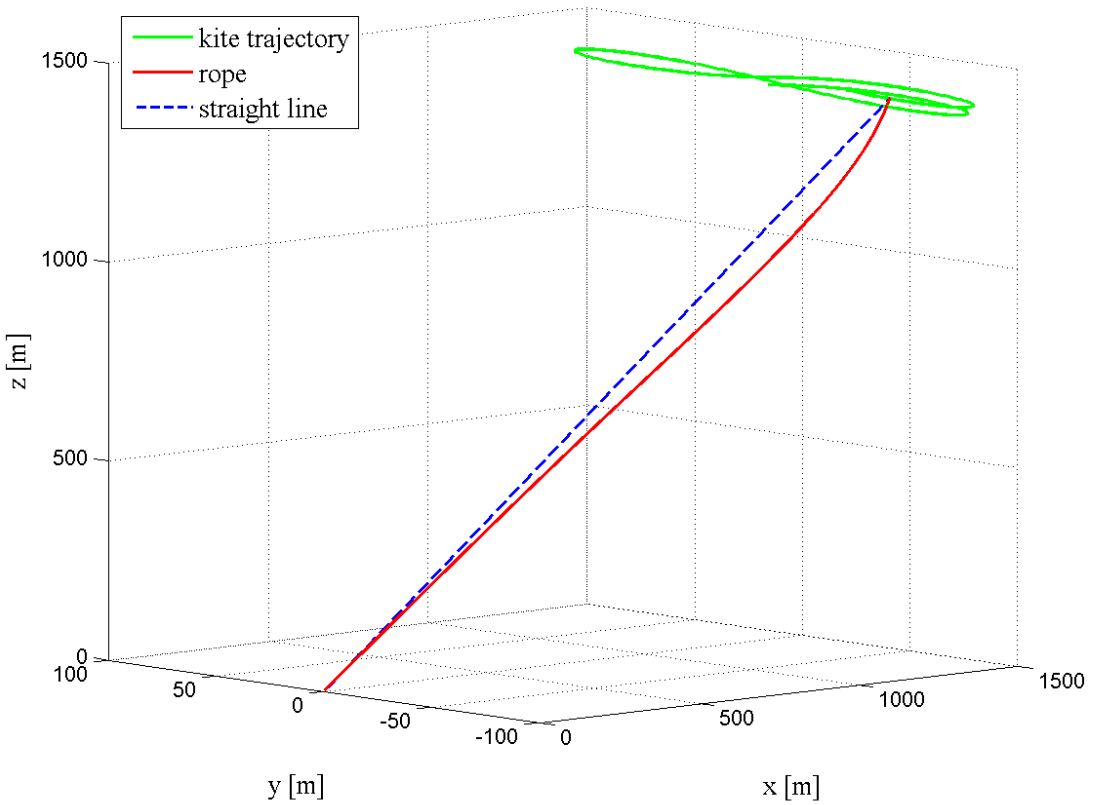

Fig. 4.35: Position assumed by a flexible rope (in red) and by a straight rope (in blue) of length of 2000m when the kite is changing its flight direction.

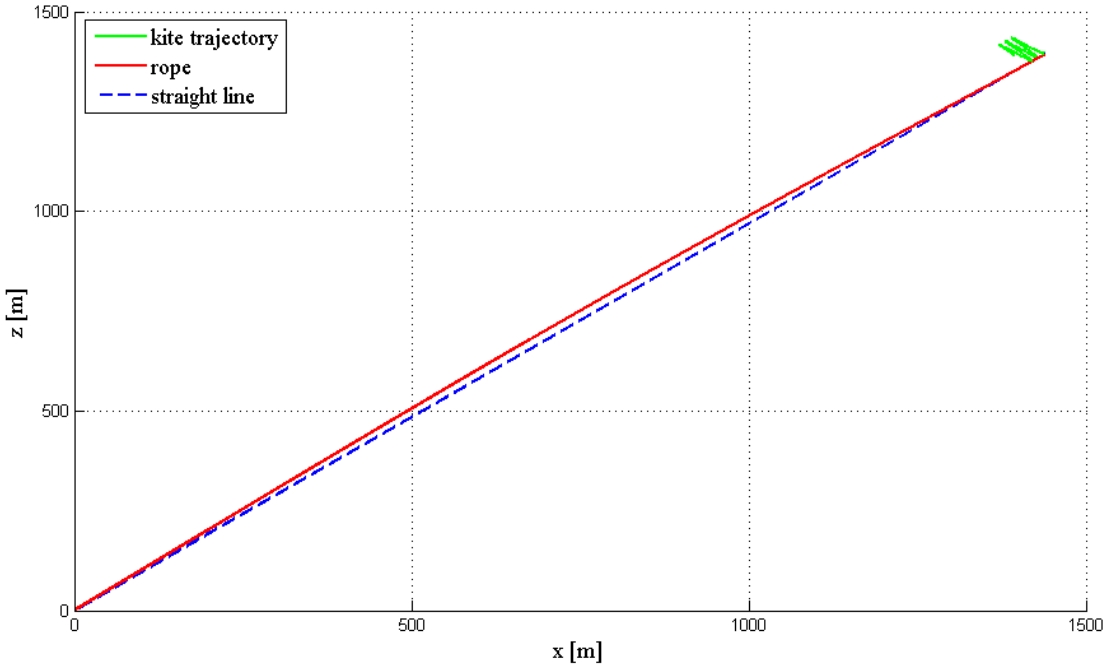

Fig. 4.36: Position assumed by a flexible rope (in red) and by a straight rope (in blue) of length of 2000m when the kite is changing its flight direction. Side view.

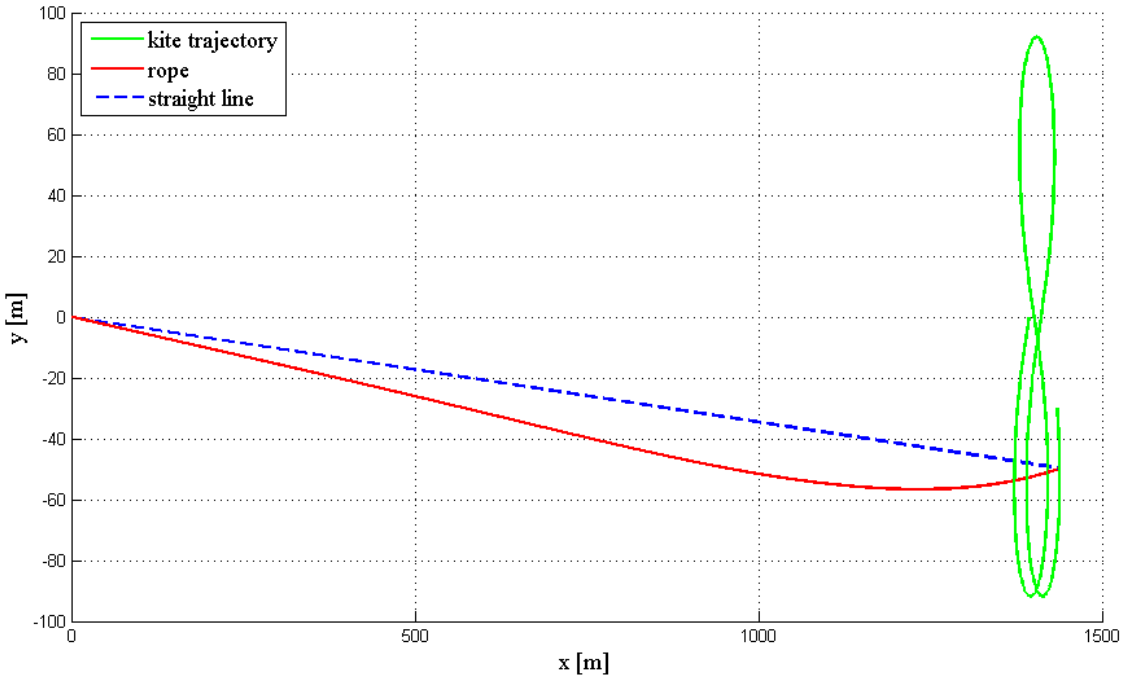

Fig. 4.37: Position assumed by a flexible rope (in red) and by a straight rope (in blue) of length of 2000m when the kite is changing its flight direction. Top view.

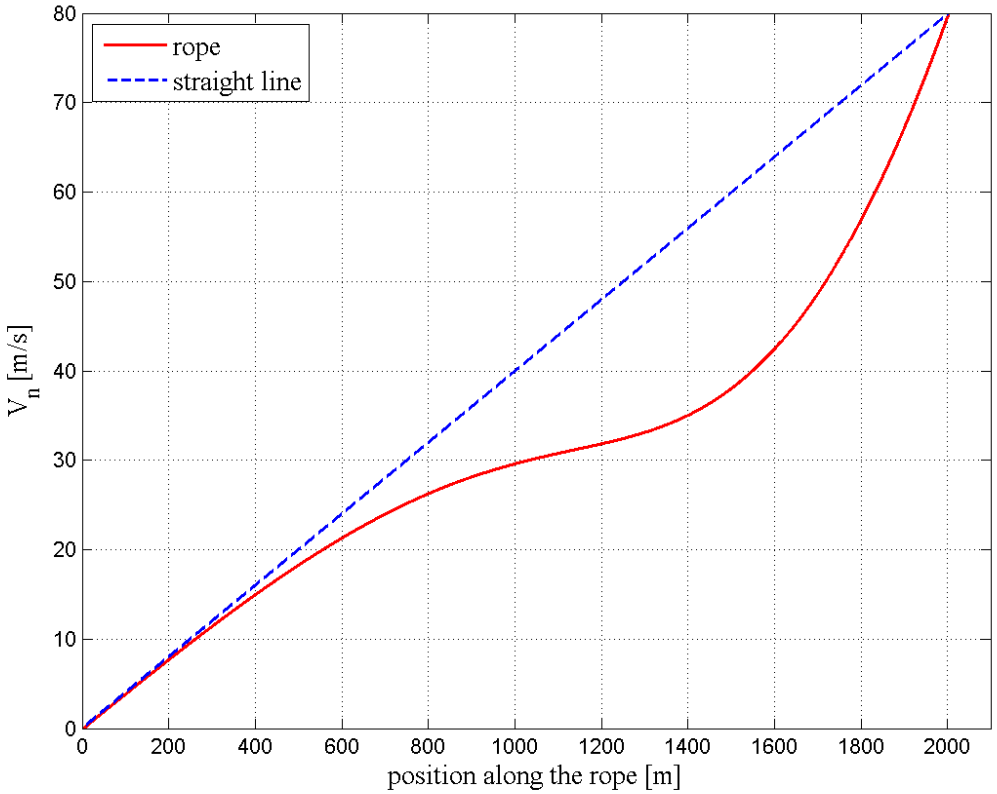

Fig. 4.38: Velocity computed along a flexible rope (in red) and a straight rope (in blue) of length of 2000m when the kite is changing its flight direction.

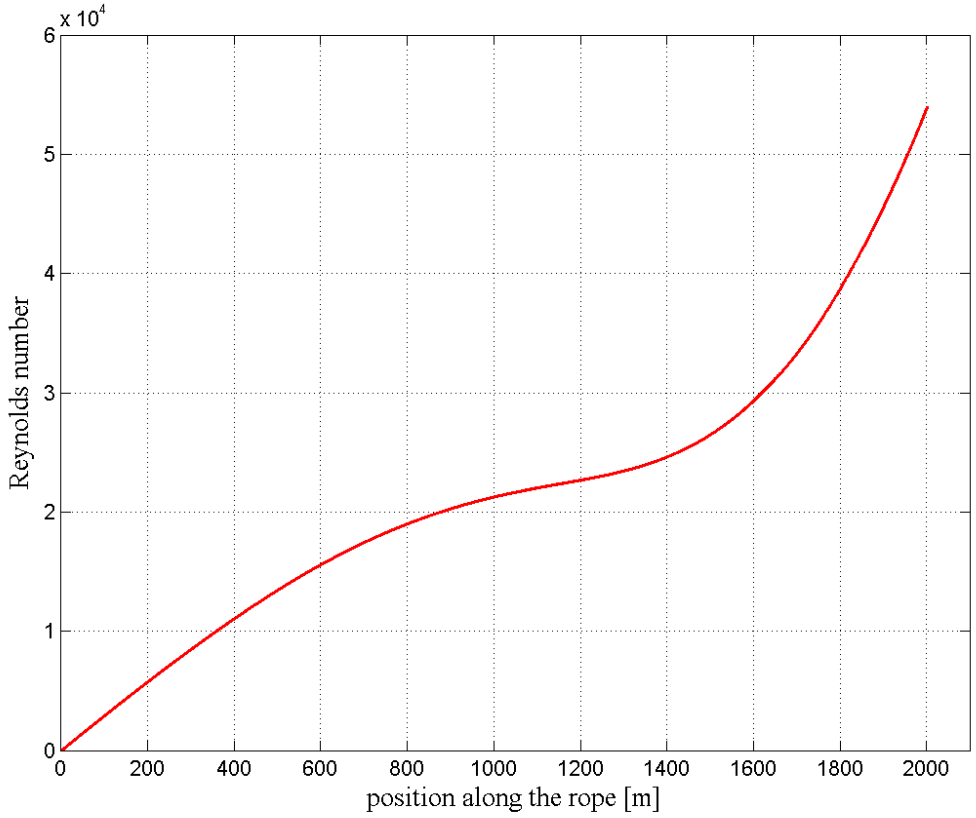

Fig. 4.39: Reynolds number computed along a flexible rope of length of 2000m when the kite is changing its flight direction.

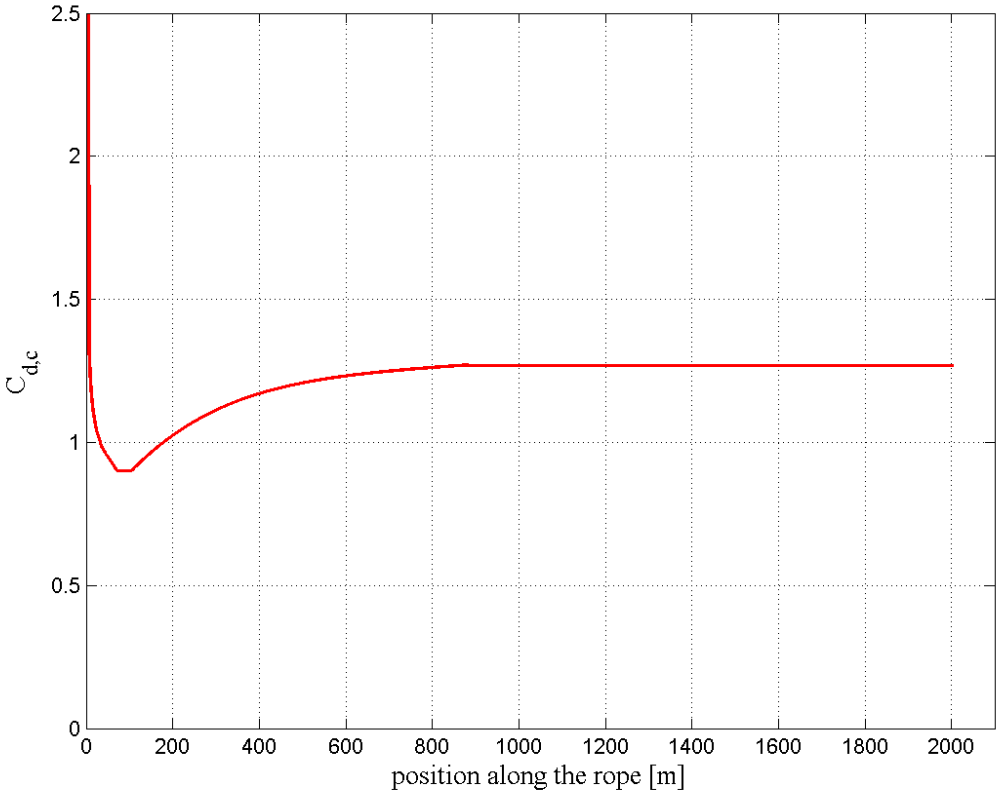

Fig. 4.40: Cable drag coefficient computed along a flexible rope of length of 2000m when the kite is changing its flight direction

The tension increase along the rope is instead given from the next graph.

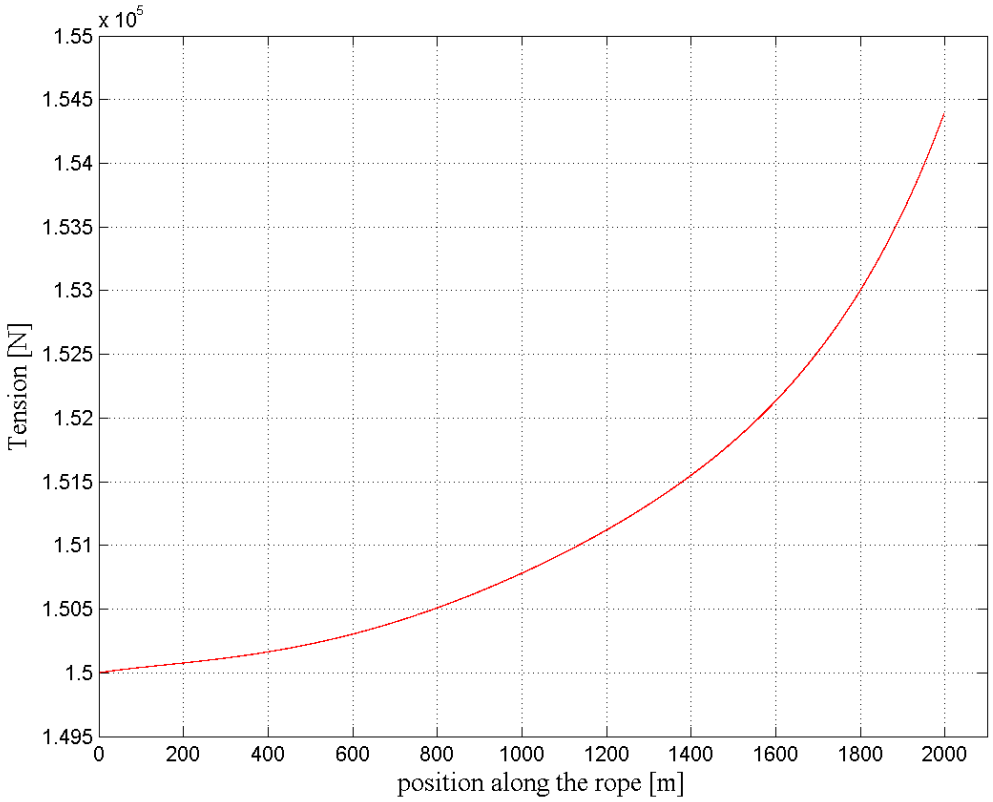

Fig. 4.41: Typical tension distribution computed along a flexible rope (in red) of length of 2000m during the kite flight.

4.2.3 Maximum value of the tension for different cable lengths

Ones that the system has been solved for different cable lengths, it is possible to evaluated the trend of how strong the traction force generated from the kite on each rope needs to be in order to have constant traction force at the generator of $150kN$ per rope. It is found that the trend is not linear and tends to an asymptote. Moreover, the chosen cable is still able to handle the load applied, even though probably the security coefficient is too low since the breaking load for a cable done of SK99 Dyneema® fibers of $d = 11mm$ is indeed of $165kN$.

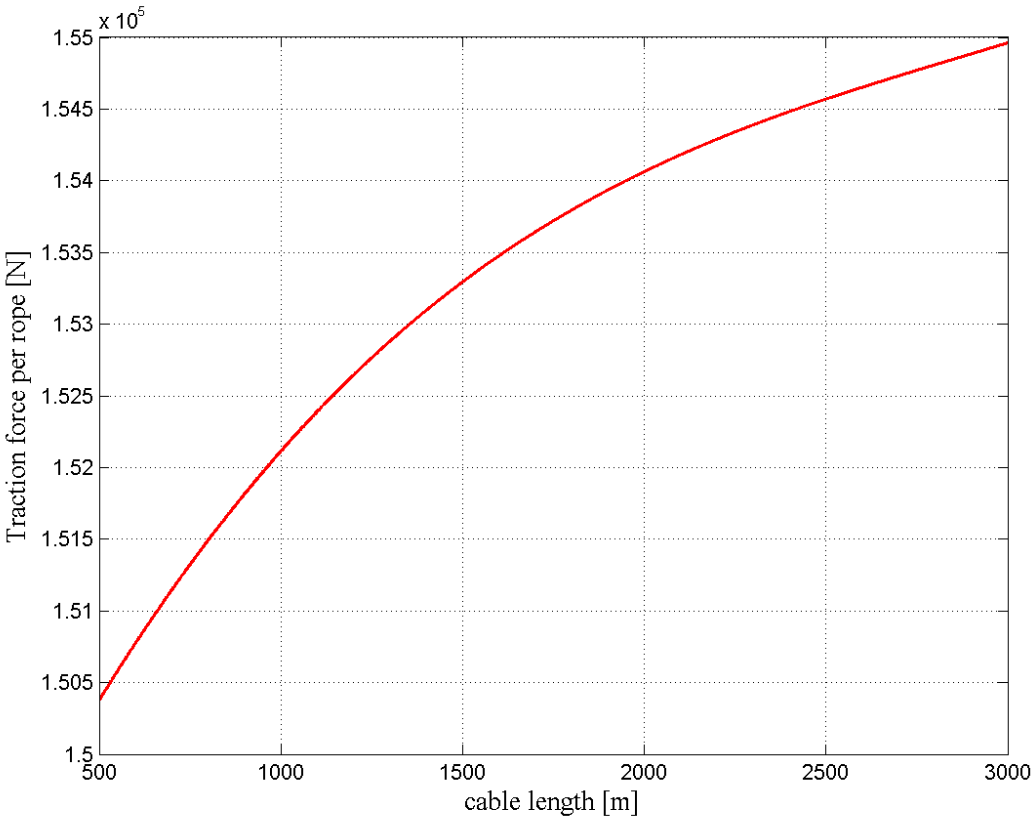

Fig. 4.42: Traction force exerted from the kite on each rope for different cable lengths in order to have at the drum constant traction force of $150kN$ *per rope.*

4.2.4 Aerodynamic drag of the lines for different lengths

It is possible to compare the trend of the cable aerodynamic resistance computed with the straight rope configuration and with the flexible rope configuration.

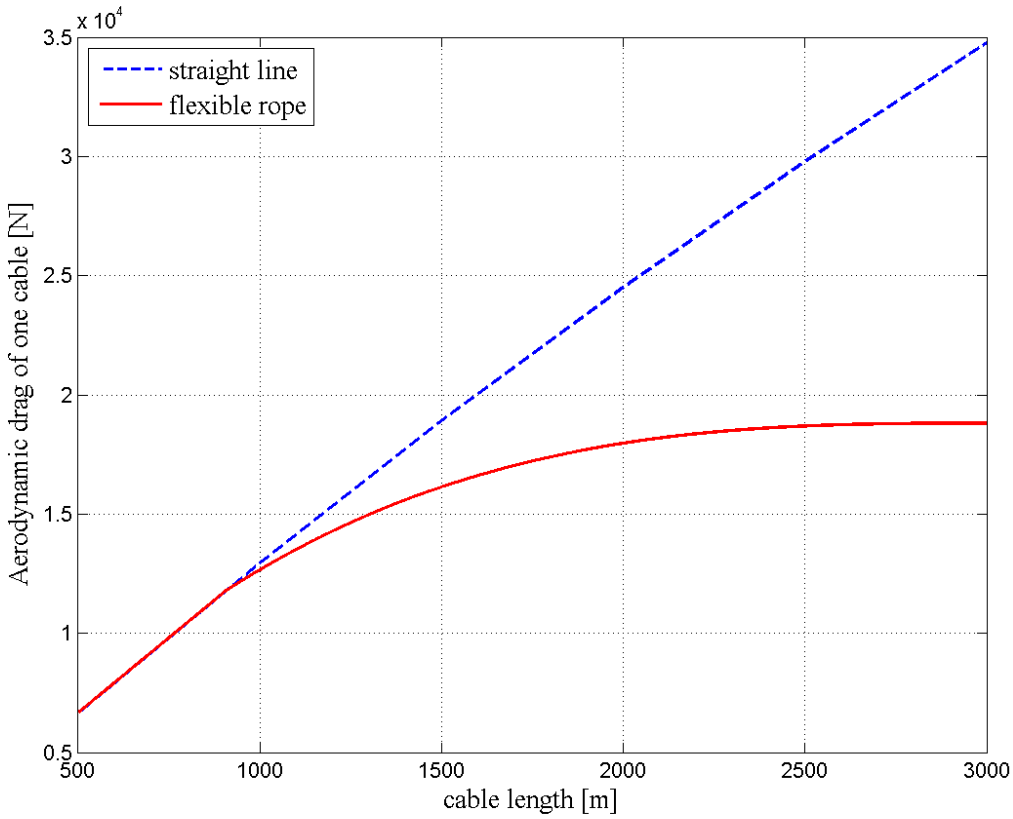

Fig. 4.43: Aerodynamic drag force computed for a straight line (in dashed blue) and for a flexible rope (in red) vs cable length with polar angle $\vartheta = 45°$.

From the previous graph it can be noticed that when the rope is not too long, the two different approaches give the same value of the aerodynamic drag force. However, when the cable length reaches approximately 1000 meters, the two curves strongly differ and in particular it seems that the assumption of the straight line strongly overestimates the value of the cable aerodynamic resistance. This, as it will be seen in the following, may have important implications on the operational conditions of a KiteGen system.

5. Global system power curves and Annual Energy Production

Ones that the aerodynamic resistance F_t of one cable has been evaluated, it is useful to define a global system aerodynamic efficiency G_e defined as:

$$G_e = \frac{L}{D_k + 2\,F_t} \qquad (5.1)$$

where L is the lift force generated from the effective wind on the kite, D_k is the aerodynamic drag force generated from the kite as it moves in the air and F_t is the aerodynamic resistance of one cable as it moves in the air. Since this particular kind of system has two ropes, in the definition of G_e, the magnitude of the overall drag given by the cables is $2\,F_t$. Finally, as done for F_t, also the variation of the air density ρ with altitude z will be considered in the evaluation of L and D_k and therefore in the calculation of G_e.

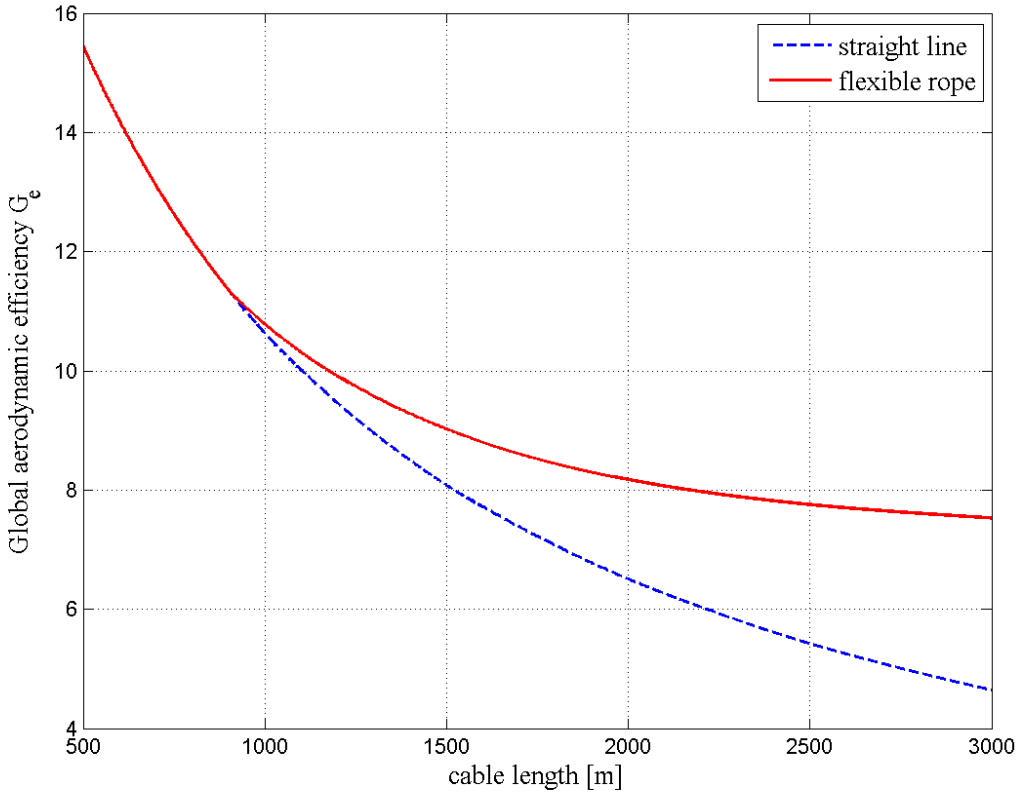

Fig. 5.1: Global aerodynamic efficiency G_e computed for a straight line (in dashed blue) and for a flexible rope (in red) vs cable length with polar angle $\vartheta = 45°$.

It is interesting now to evaluate if working at increasing altitudes allows one to maximize the energy production or if at a certain altitude there is an optimal point of highest energy production. Operating at higher altitude, indeed, from one side allows to harvest stronger and more constant wind, but from the other side lowers the global aerodynamic efficiency G_e. The altitude giving the optimal working point, however, is strongly dependent on the considered location.

In order to make this analysis, it is first needed to evaluate the new power curves considering G_e in place of the kite aerodynamic efficiency E, then to change again these curves in order to consider also the recovery phase and finally it is possible to obtain the annual energy production considering the wind probability functions of a specific location. These functions give the probability of occurrence of the wind at a certain intensity, for a specific altitude range, and have been evaluated using the RAOB (rawinsonde) database of NOAA. Each probability function is evaluated considering a variation of elevation $\Delta z = 300m$ starting from the altitude of $200m$ up to $2300m$. The value of Δz has been chosen equal to $300m$ since it is expected that the active phase of a KiteGen machine will last for a time long enough to unroll the cable for approximately $450m$. The global elevation range explored ($200m \div 2300m$) has been chosen, instead, in such a way to have cable length approximately varying from $500m$ to $3000m$, which is the maximum length considered in the dynamic analysis. In the next table are summarized for each elevation range the value of the mean cable length and of the mean global efficiency G_e (both for the case of straight lines and flexible ropes).

$z\ [m]$	Mean cable length [m]	G_e straight lines	G_e flexible ropes
$200 \div 500$	500	15.38	15.38
$500 \div 800$	919	11.14	11.16
$800 \div 1100$	1343	8.68	9.36
$1100 \div 1400$	1768	7.09	8.42
$1400 \div 1700$	2192	5.99	7.90
$1700 \div 2000$	2616	5.16	7.61
$2000 \div 2300$	3000	4.58	7.43

Tab. 5.1: Mean cable length and global aerodynamic efficiency G_e (evaluated for straight lines and for flexible ropes) as function of the elevation z.

5.1 Global system characteristic curves

From the previous table it is clear that the shape of the characteristic curves is function of the considered cable length. Furthermore, the longer are the cables and the more the characteristic curves evaluated with the straight lines approach will differ from those evaluated with flexible lines. It should also be highlighted that, if the dimensions of the trajectory performed by the kite are kept constant for each cable length considered, the value of mean azimuth angle ϕ will decrease. In particular, its average value with the cable lengths already considered are shown in the next table.

Mean cable length [m]	Mean ϕ [°]
500	7.52
919	4.16
1343	2.86
1768	2.17
2192	1.75
2616	1.47
3000	1.28

Tab. 5.2: Mean azimuth angle during the kite flight

The evolution of the characteristic curves as function of the lines length can be found in the annex. In the following, the specific case of a KiteGen system with two ropes of $3000m$ is shown, while, for the remaining cases, the characteristic wind velocities (i.e. cut-in wind speed, full-force wind speed and full-power wind speed) are provided in the next table.

Mean cable length [m]	Straight lines			Flexible ropes		
	V_{cut-in} $[m/s]$	$V_{full-force}$ $[m/s]$	$V_{full-power}$ $[m/s]$	V_{cut-in} $[m/s]$	$V_{full-force}$ $[m/s]$	$V_{full-power}$ $[m/s]$
500	2.86	5.99	25.03	2.86	5.99	25.03
919	2.86	8.30	27.23	2.86	8.28	27.21
1343	2.86	10.72	29.62	2.86	9.96	28.86
1768	2.86	13.23	32.13	2.86	11.20	30.10
2192	2.86	15.80	34.69	2.86	12.09	30.97
2616	2.86	18.44	37.33	2.86	12.71	31.60
3000	2.86	20.95	39.84	2.86	13.20	32.08

Tab. 5.3: Characteristic velocities of a KiteGen system for different cable lengths. Comparison between straight lines approach and flexible ropes approach.

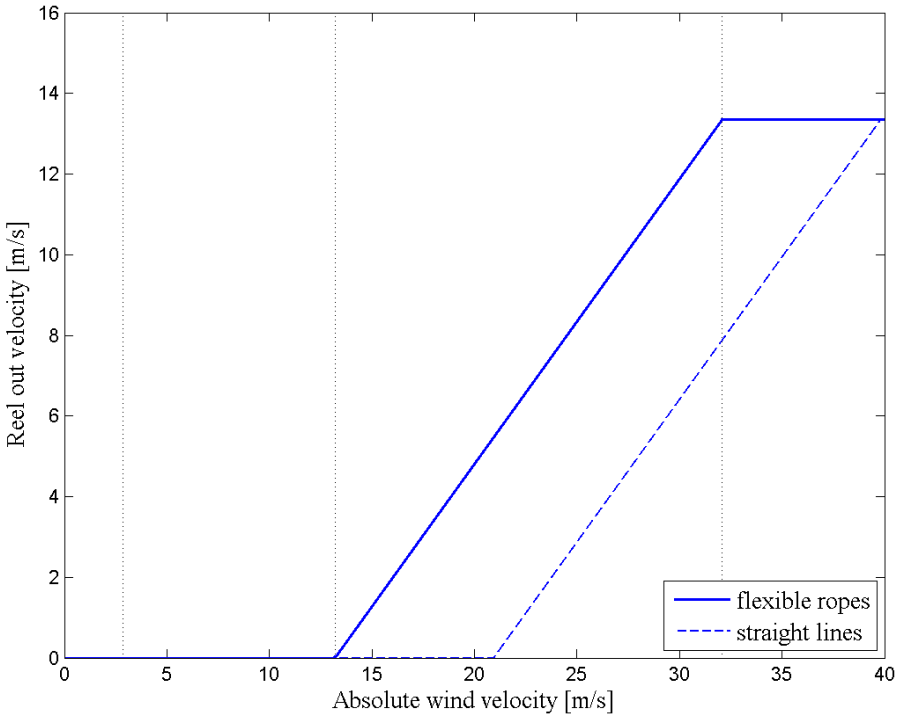

Fig. 5.2: Reel-out velocity vs absolute wind velocity for a KiteGen system with two $3000m$ long flexible ropes (continuous curve) and with two $3000m$ long straight lines (dashed curve)

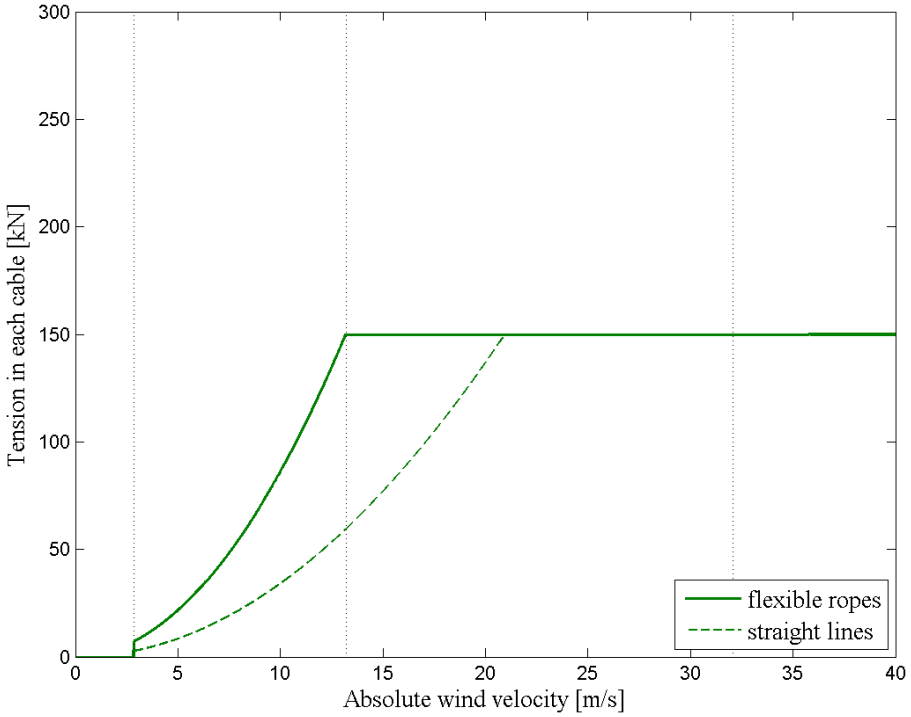

Fig. 5.3: Traction force acting on one rope vs absolute wind velocity for a KiteGen system with two 3000m long flexible ropes (continuous curve) and with two 3000m long straight lines (dashed curve)

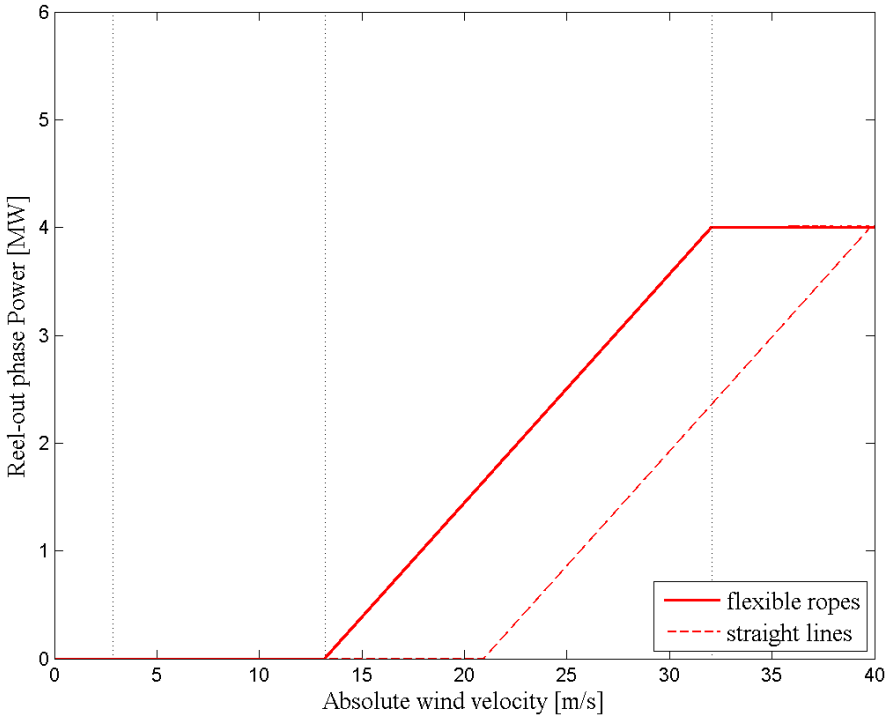

Fig. 5.4: Generated power during the active phase vs absolute wind velocity for a KiteGen system with two 3000m long flexible ropes (continuous curve) and with two 3000m long straight lines (dashed curve)

5.2 Recovery phase

As already mentioned, the generated power during the active phase has been chosen following the KiteGen Research indications in such a way to have nominal mean generated power of $3MW$. The difference between the power generated during the reel-out phase and the mean power is given from the power spent during the passive phase and from the lack of production during the same phase. In particular, the power needed for the recovery of the kite is actually really small, since it is considered the application of the so-called side slip maneuver, already explained in Section 2.1.2. The main contribution to the reduction of the net power is therefore given from the lack of production during the passive phase, but also in this case it is possible to minimize this effect thanks to the reel-in velocity of the drums of roughly $15 \div 20\ m/s$ which allow to perform this operation very quickly.

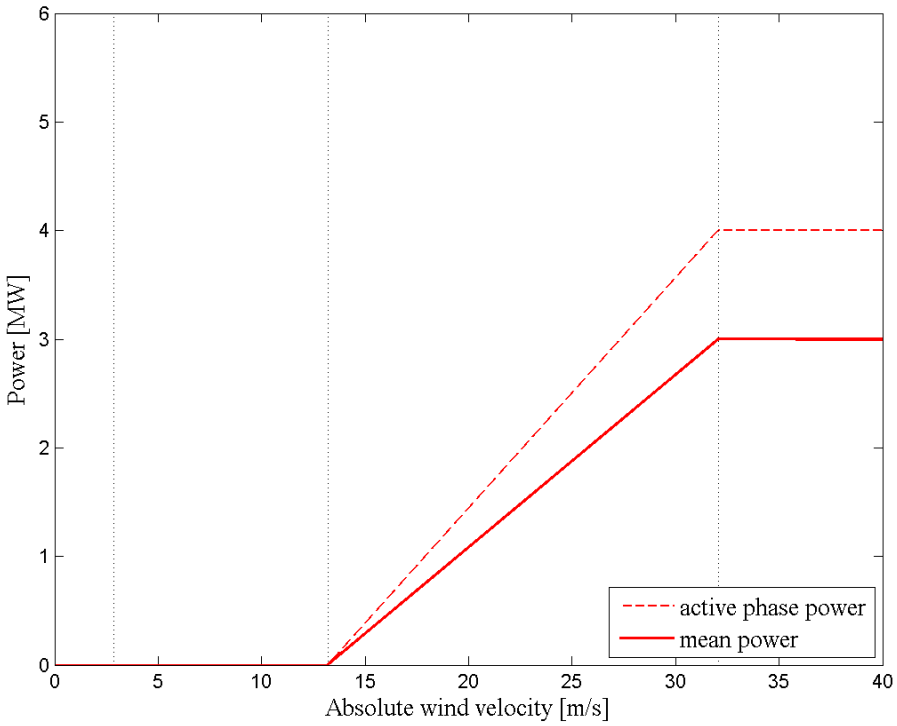

Fig. 5.5: Difference between the active phase power curve and the mean power curve for a KiteGen system operating with two 3000 m long flexible ropes

5.3 Annual Energy Production

It is now possible, thanks to the wind probability functions derived from the RAOB database of NOAA and shown in Appendix A, to compute the Annual Energy Production (AEP) obtainable with the 3MW KiteGen system for the location of De Bilt, in the Netherlands.
If $f(V_{w,i} < V_w < V_{w,i+1})$ is the probability that the wind speed V_w lies between $V_{w,i}$ and $V_{w,i+1}$, and $P(V_{w,i})$ is the power generated from the machine when wind at the intensity of $V_{w,i}$ is flowing, then the AEP can be evaluated as:

$$AEP = \sum_{i=1}^{N-1} \frac{1}{2} \left(P(V_{w,i}) + P(V_{w,i+1}) \right) \cdot f\left(V_{w,i} < V_w < V_{w,i+1} \right) \cdot 8760 \qquad (5.2)$$

where N is the number of nodes in which the wind speed is discretized and 8760 is the number of hours in one year. It should be highlighted that the function $P(V_w)$ is evaluated considering power curves like the one in Fig. 5.5, therefore already accounting for the passive phase.

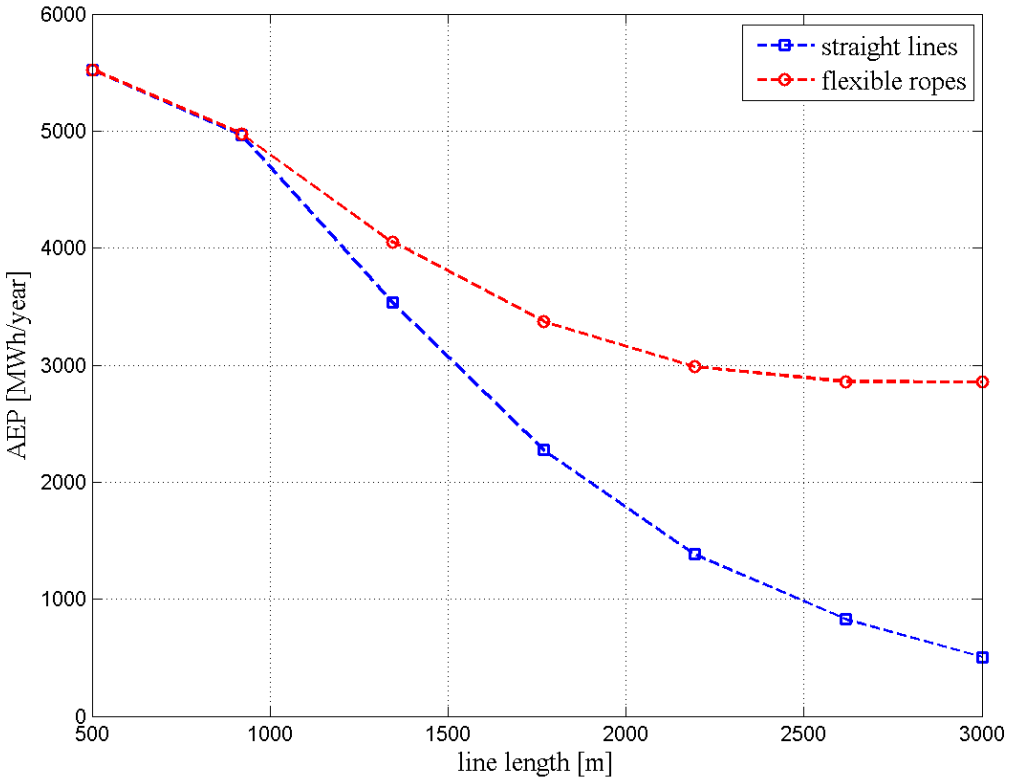

Fig. 5.6: Annual Energy Production (AEP) for the 3MW KiteGen system assuming the cables as straight lines (in blue squares) and flexible ropes (in red circles)

6. Conclusions

The aim of this work was to evaluate the aerodynamic drag force generated by the cables connecting a kite to the ground station of a KiteGen system. In particular, the accuracy of the most used approximation in this field, which considers the cables as straight lines, was investigated. This need has emerged due to experimental observations during the flight of a power kite. It has been noticed, indeed, that the ropes configuration strongly differs from that of two straight lines and, in particular, the ropes tend to follow the kite movement mainly with their highest portion, while the remaining part of the ropes tends to stay quieter closer to the axis of the kite trajectory.

In order to find the configuration assumed by the ropes during the kite flight, a dynamic system was set. This system consisted in the Newton's law of motion applied on the ropes. In particular, the main forces acting on that system were considered: the aerodynamic drag force, the gravity and the variable tension along the cables. The system was numerically solved considering as boundary condition the movement at constant transversal velocity of the kite on a realistic eight-shaped trajectory while the cables are unrolled from the drums. The found solution clearly indicate a discordance between the cables configuration and the positions of two ideal straight lines. This behavior has a huge impact on the estimation of the aerodynamic drag of the cables.

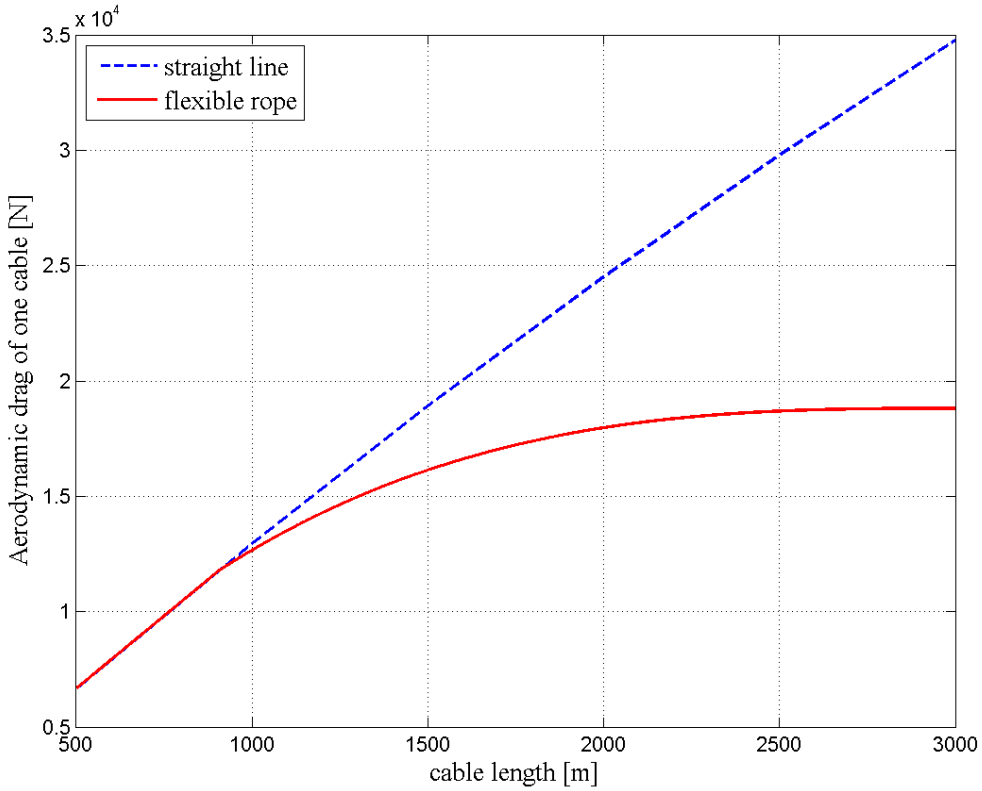

Fig. 6.1: Aerodynamic drag force computed for a straight line (in dashed blue) and for a flexible rope (in red) vs cable length with polar angle $\vartheta = 45°$.

The drag force of the cables is a key aspect to be considered in the estimation of a global system aerodynamic coefficient G_e, whose value affect the shape of the power curves. In general, the longer are the ropes and the higher will be the value of the cable aerodynamic drag force F_t and, as a consequence, the smaller will be G_e, since it is defined as:

$$G_e = \frac{L}{D_k + 2\,F_t} \qquad (6.1)$$

A smaller value of G_e implies the movements rightwards of the power curves introduced in Section 2.4 and therefore the need of stronger winds to produce a certain amount of power. On the other side, having longer ropes allows one to operate at higher altitude, where stronger winds are available, as highlighted in Chapter 3. A correct estimation of F_t is therefore essential in order to have a realistic value of G_e and to evaluate the optimal cables length which allow to maximize the energy production.

With Fig. 5.6, it has been shown that with the present analysis, the maximum energy production for the specific site of De Bilt, in The Netherlands, is reached with $500m$ long cables, a length for which both the approaches used give the same value of the cables drag force. Nevertheless, starting from roughly $900m$, the difference in the estimation of AEP with the two approaches becomes significantly evident.

It has been highlighted, therefore, the need of a deeper study on the dynamics of the kite lines since there are still some physical phenomena which have been ignored in this work and a possible overestimation of the power output reduction due to the cables drag risks to underestimate the capability of this promising technology. Hence, for future works, the main phenomena to be added to the present analysis are the elasticity of the ropes, the finite velocity of propagation of the pulses that the kite movement sends to the ropes and internal damping. Moreover, also the possibility of adopting special cables with reduced drag coefficient should be considered.

Appendix A

In the following the wind probability density functions at different elevation ranges for the site of De Bilt are shown.

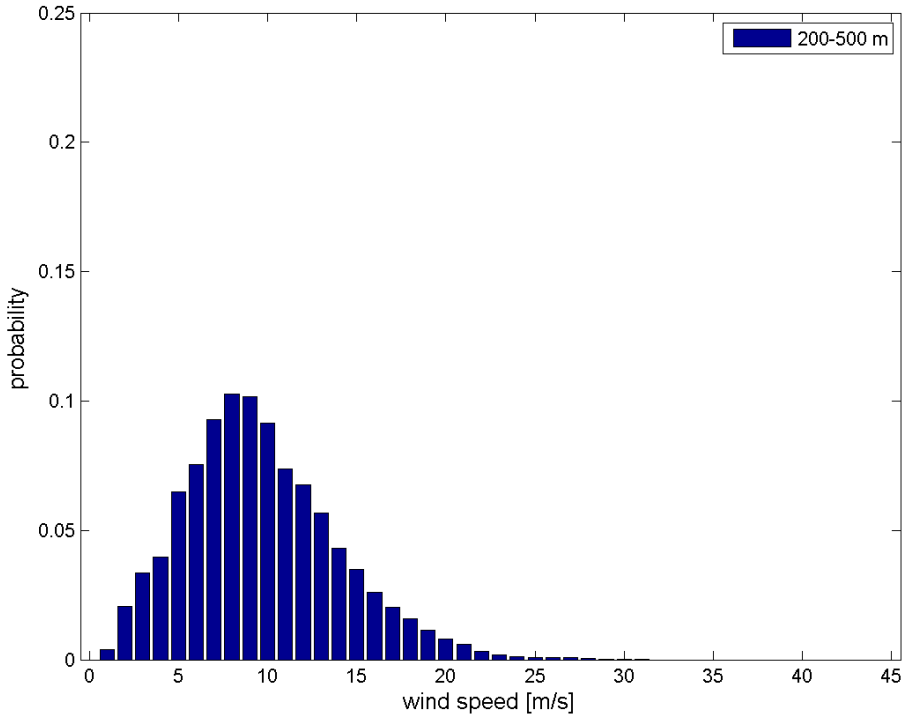

Fig. A. 1: Wind probability density function between 200m and 500m of elevation for the site of De Bilt.

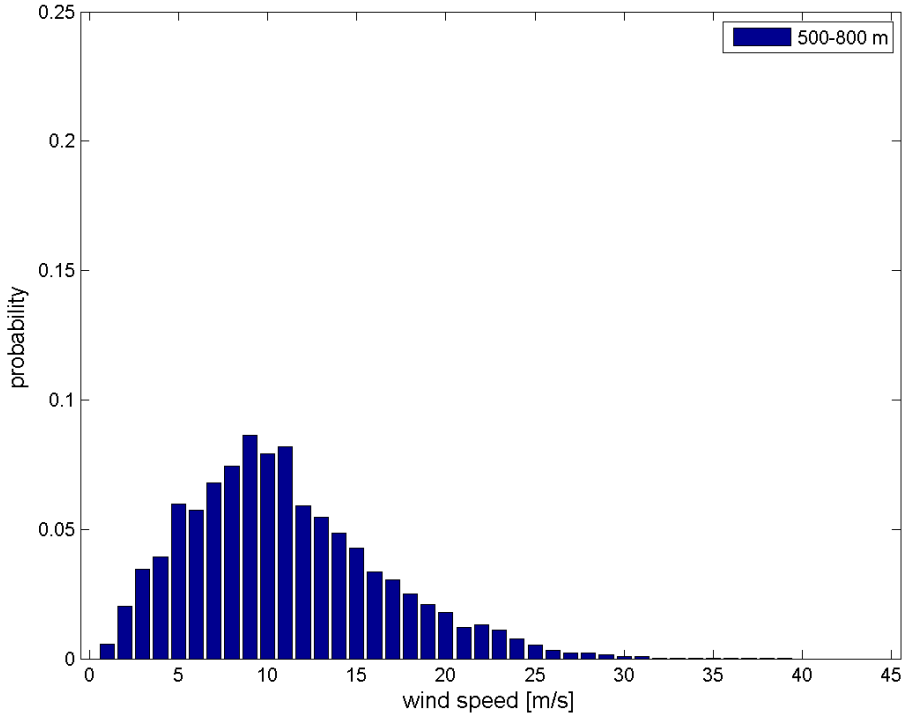

Fig. A. 2: Wind probability density function between 500m and 800m of elevation for the site of De Bilt.

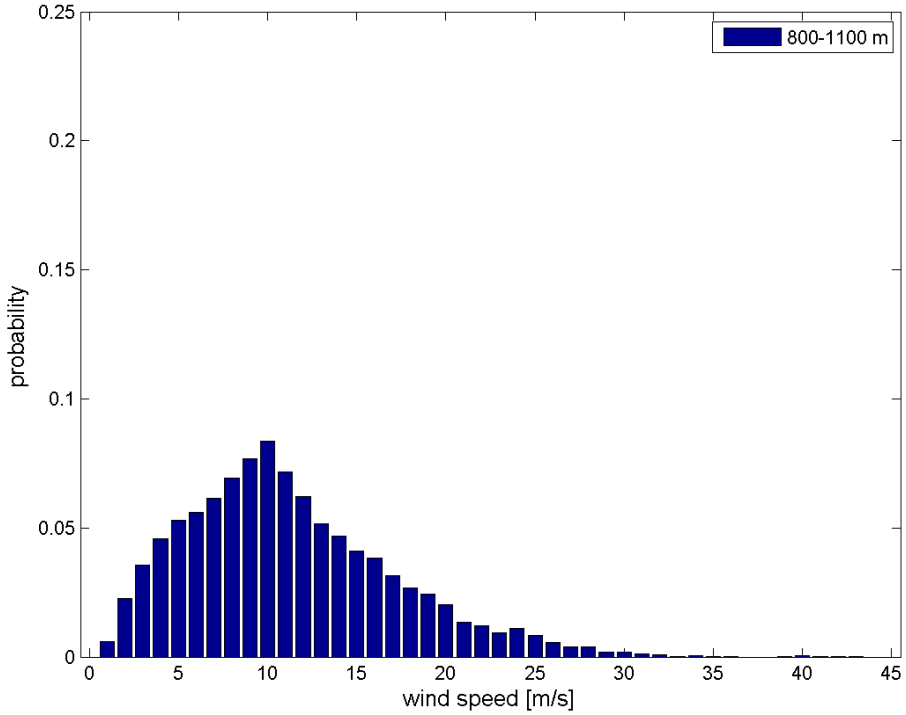

Fig. A. 3: Wind probability density function between 800m and 1100m of elevation for the site of De Bilt.

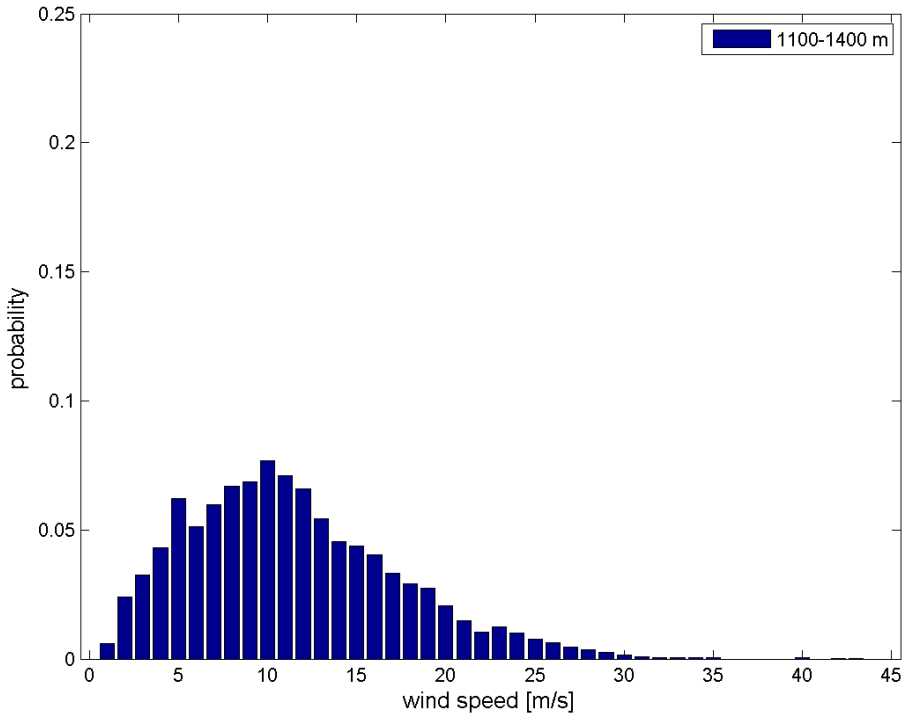

Fig. A. 4: Wind probability density function between 1100m and 1400m of elevation for the site of De Bilt.

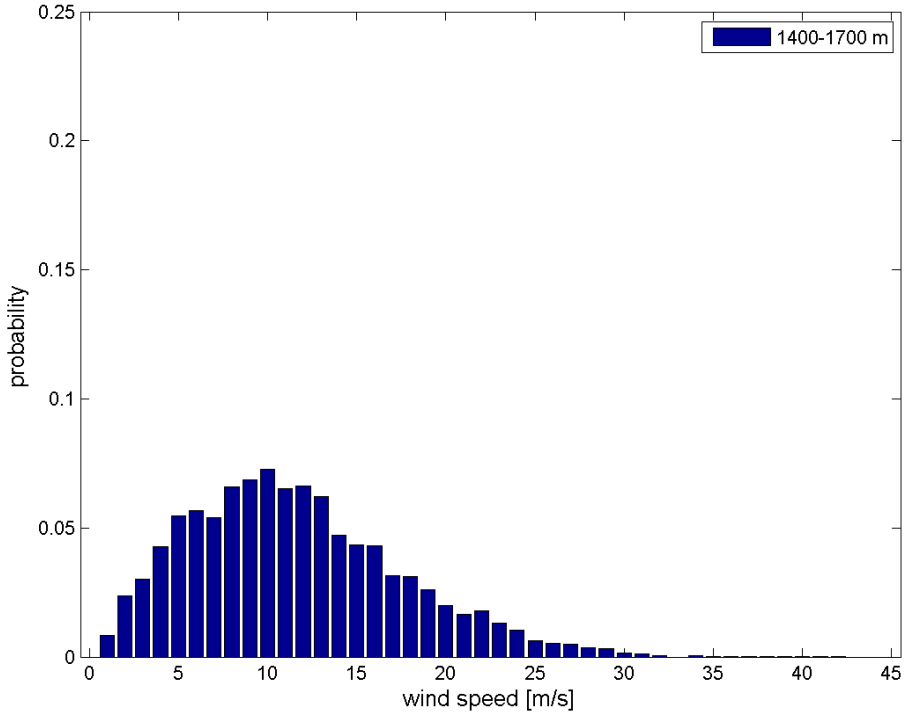

Fig. A. 5: Wind probability density function between 1400m and 1700m of elevation for the site of De Bilt.

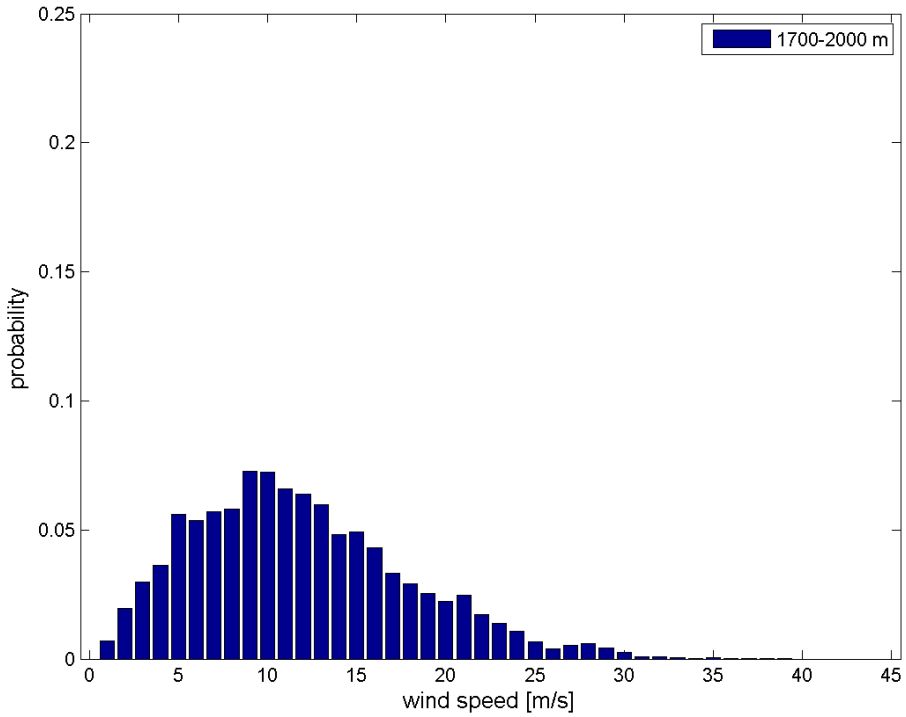

Fig. A. 6: Wind probability density function between 1700m and 2000m of elevation for the site of De Bilt.

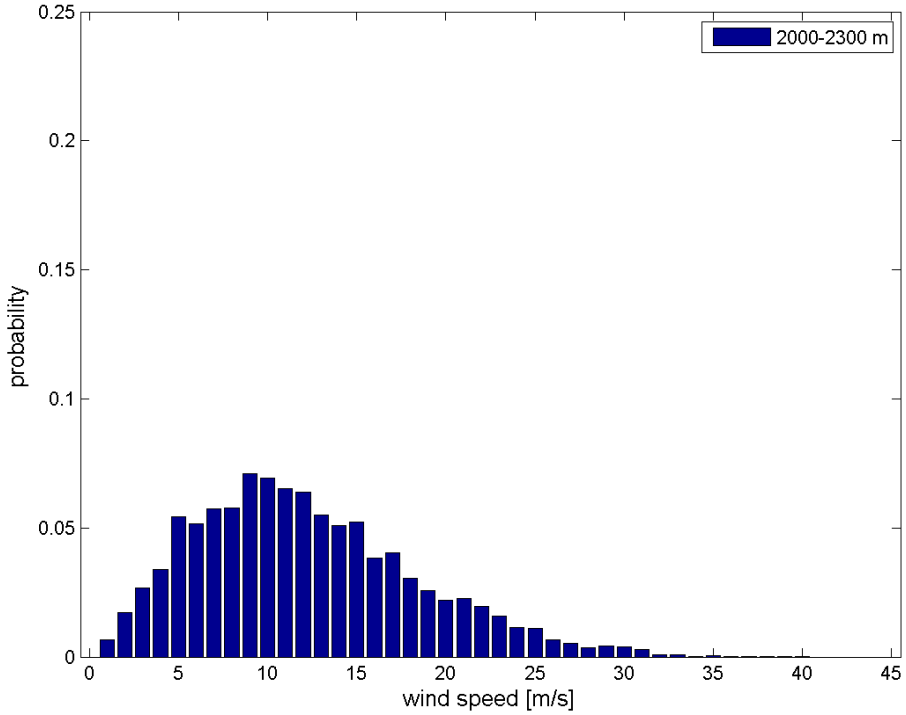

Fig. A. 7: Wind probability density function between 2000m and 2300m of elevation for the site of De Bilt.

Appendix B

Characteristic curves of a KiteGen system evaluated for different cable lengths. For each cable length it is shown the reel-out velocity curve, the traction force curve, the active power curve and the mean power curve. In particular, the mean power curves refer to the flexible ropes configuration.

Cables length: 500m

In the case of two $500m$ long cables, there is no difference between the characteristic curves evaluated with straight lines and with flexible ropes. Therefore in the following plots the two curves coincide.

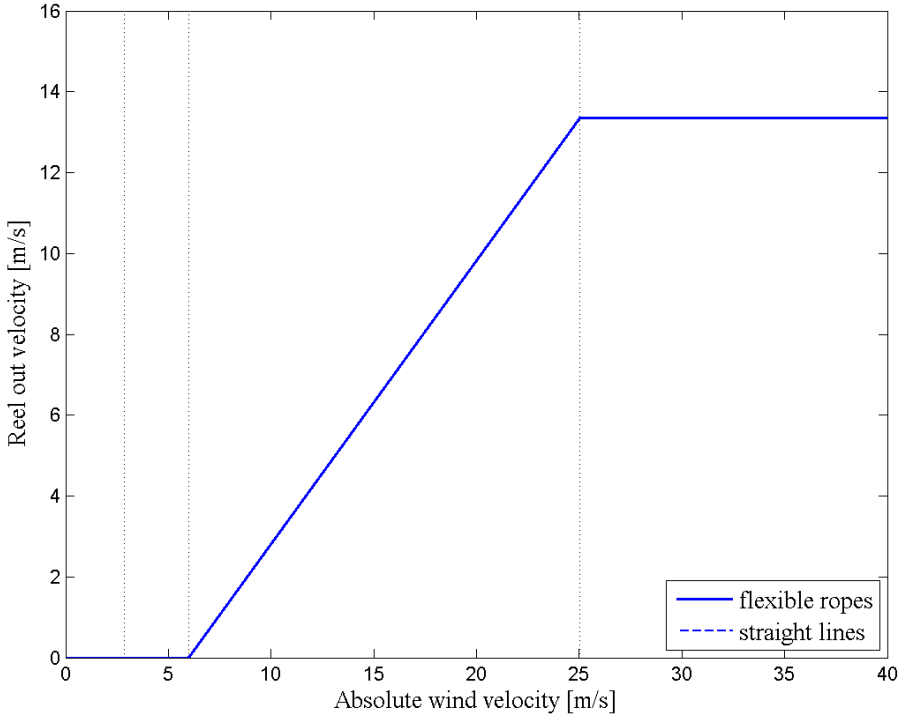

Fig. B. 1: Reel-out velocity vs absolute wind speed of a KiteGen system operating with two $500m$ *long cables. Comparison between straight lines approach and flexible lines approach.*

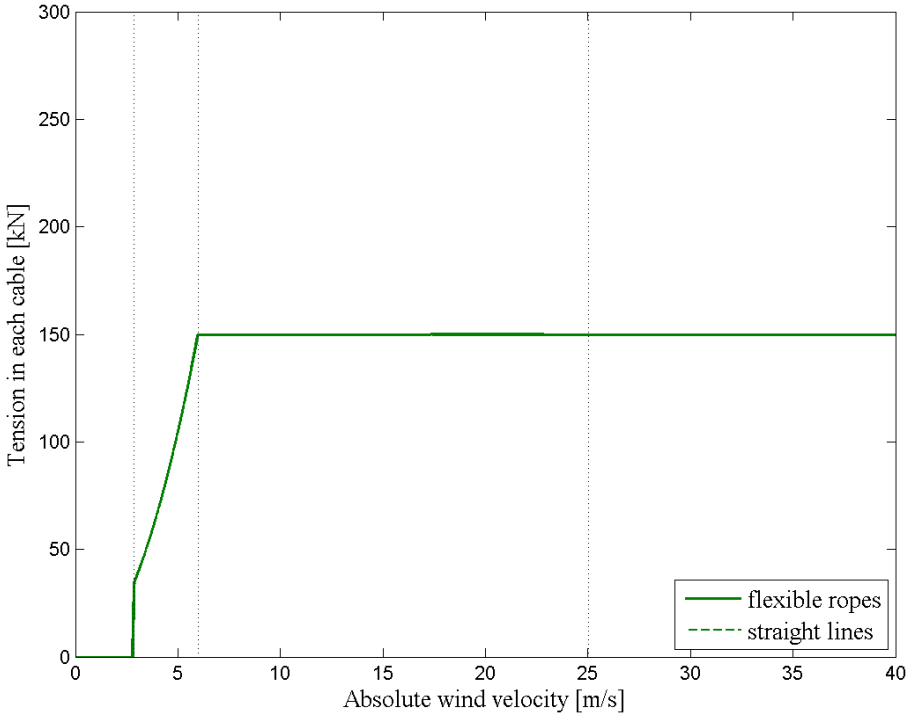

Fig. B. 2: Traction force on each line vs absolute wind speed of a KiteGen system operating with two 500m long cables. Comparison between straight lines approach and flexible lines approach.

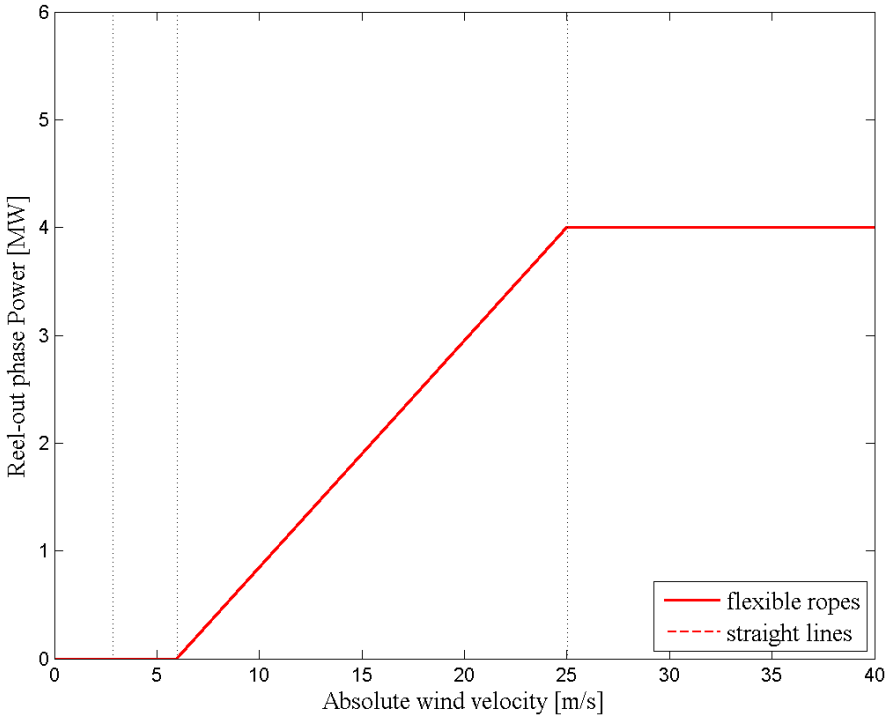

Fig. B. 3: Reel-out phase power vs absolute wind speed of a KiteGen system operating with two 500m long cables. Comparison between straight lines approach and flexible lines approach.

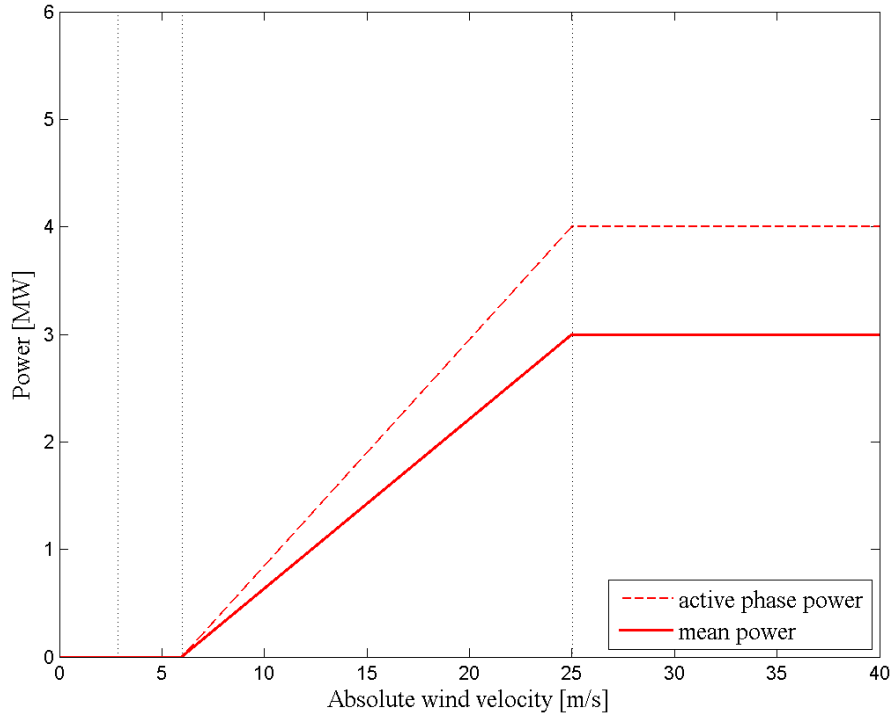

Fig. B. 4: Comparison between the power produced during the active phase and the mean power output of a KiteGen system with two 500m long flexible ropes.

Cables length: 919 m

In the case of two $919m$ long cables, there is no difference between the characteristic curves evaluated with straight lines and with flexible ropes. Therefore in the following plots the two curves coincide.

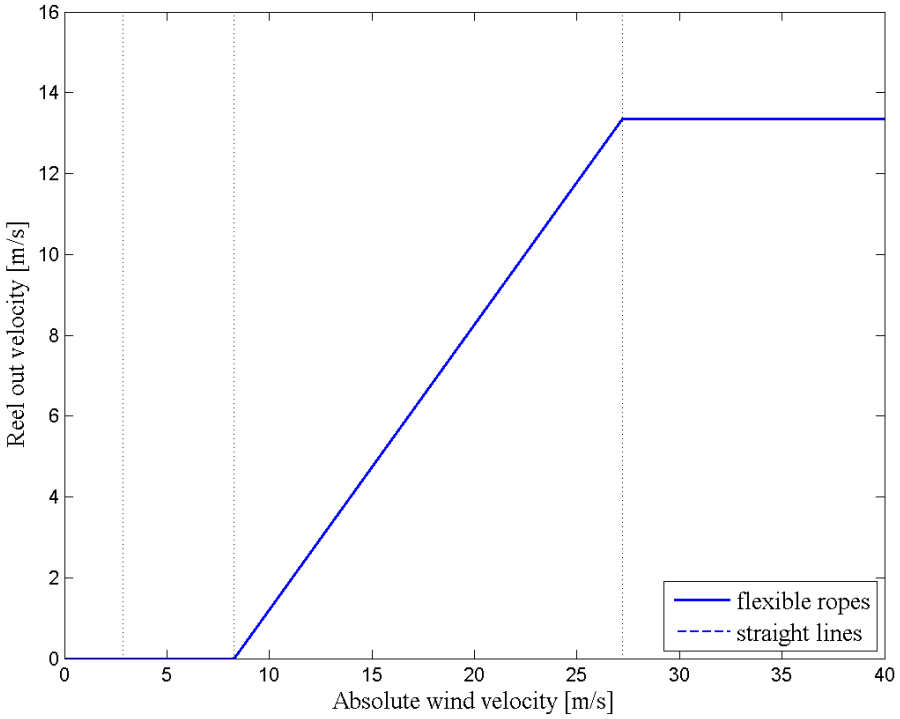

Fig. B. 5: Reel-out velocity vs absolute wind speed of a KiteGen system operating with two 919m long cables. Comparison between straight lines approach and flexible lines approach.

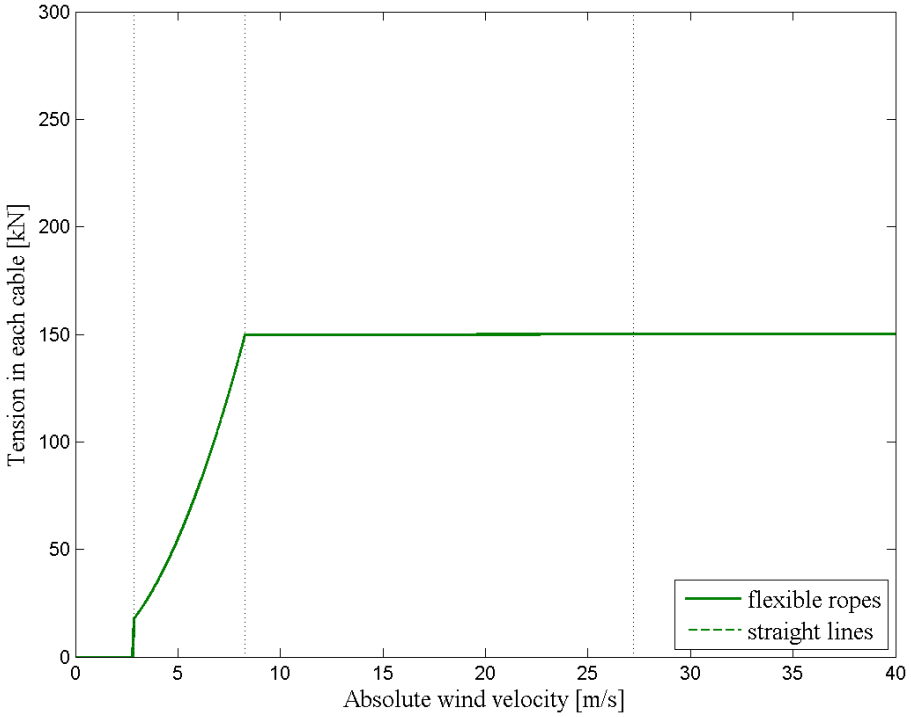

Fig. B. 6: Traction force on each line vs absolute wind speed of a KiteGen system operating with two 919m long cables. Comparison between straight lines approach and flexible lines approach.

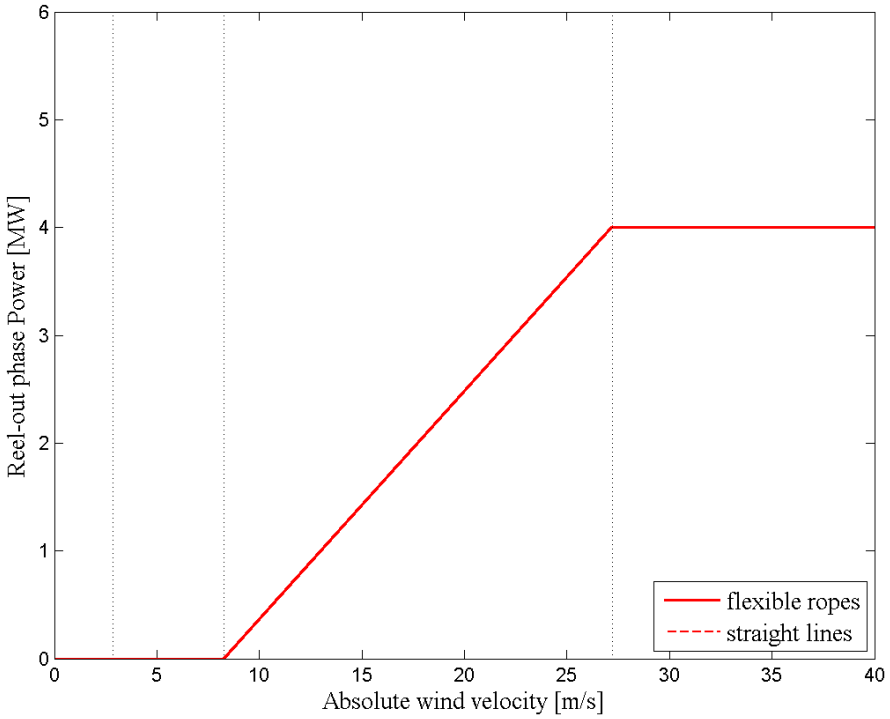

Fig. B. 7: Reel-out phase power vs absolute wind speed of a KiteGen system operating with two 919m long cables. Comparison between straight lines approach and flexible lines approach.

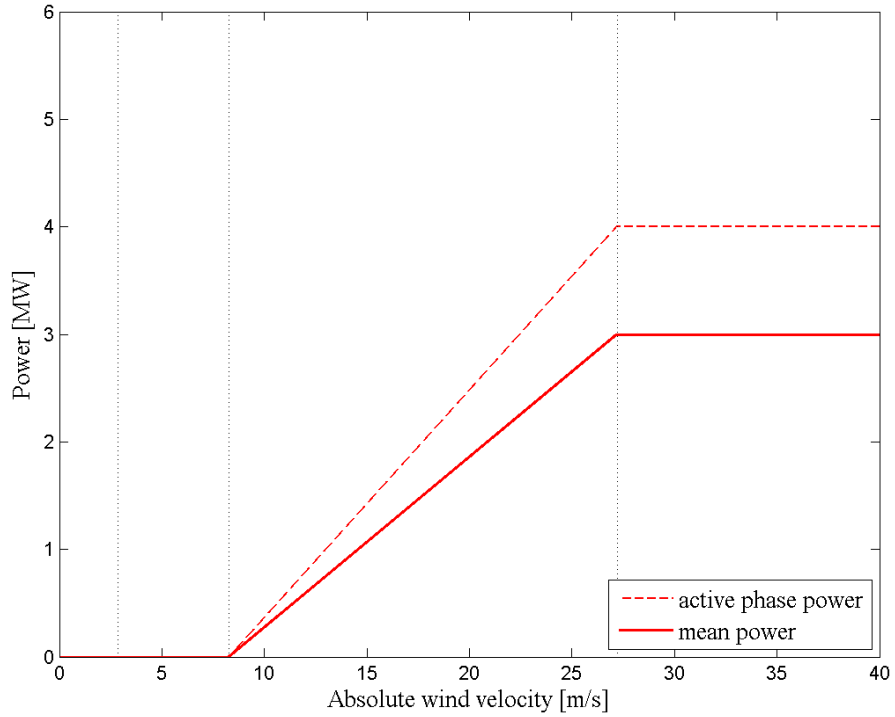

Fig. B. 8: Comparison between the power produced during the active phase and the mean power output of a KiteGen system with two 919m long flexible ropes.

Cables length:1343 m

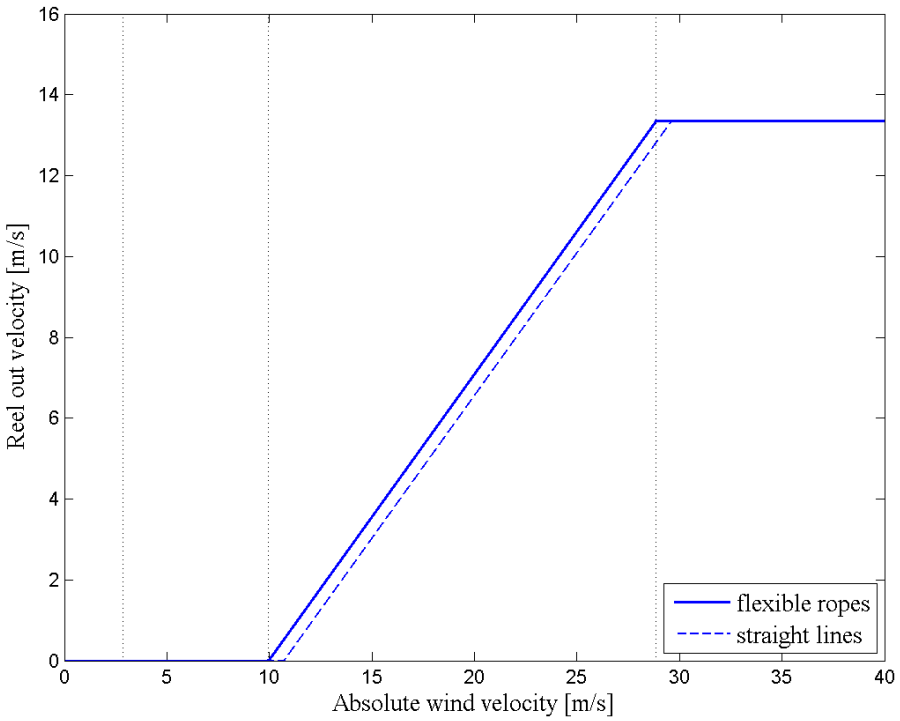

Fig. B. 9: Reel-out velocity vs absolute wind speed of a KiteGen system operating with two 1343m long cables. Comparison between straight lines approach and flexible lines approach.

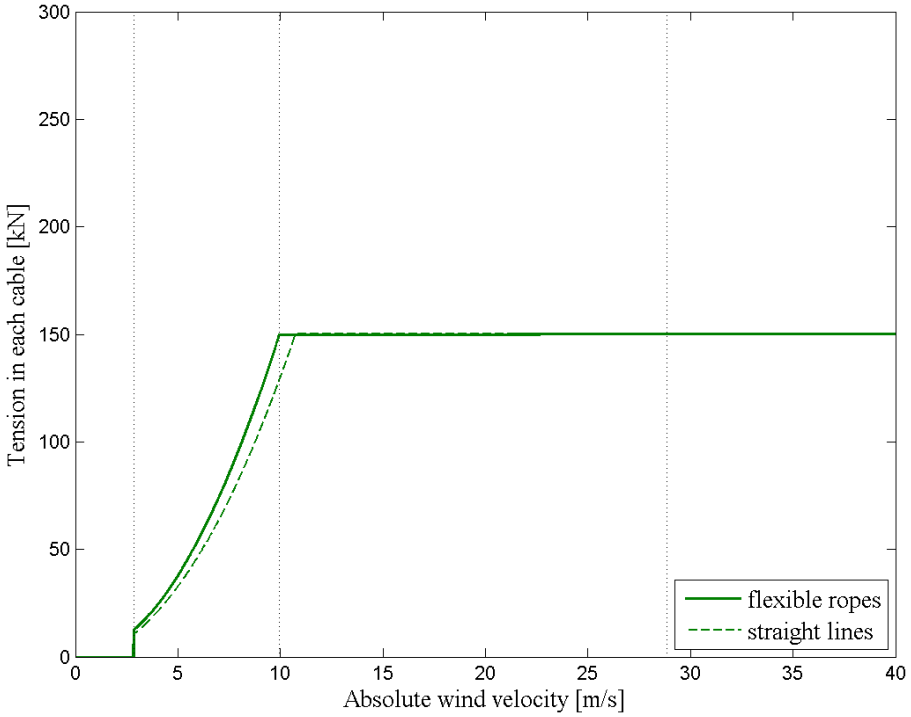

Fig. B. 10: Traction force on each line vs absolute wind speed of a KiteGen system operating with two 1343m long cables. Comparison between straight lines approach and flexible lines approach.

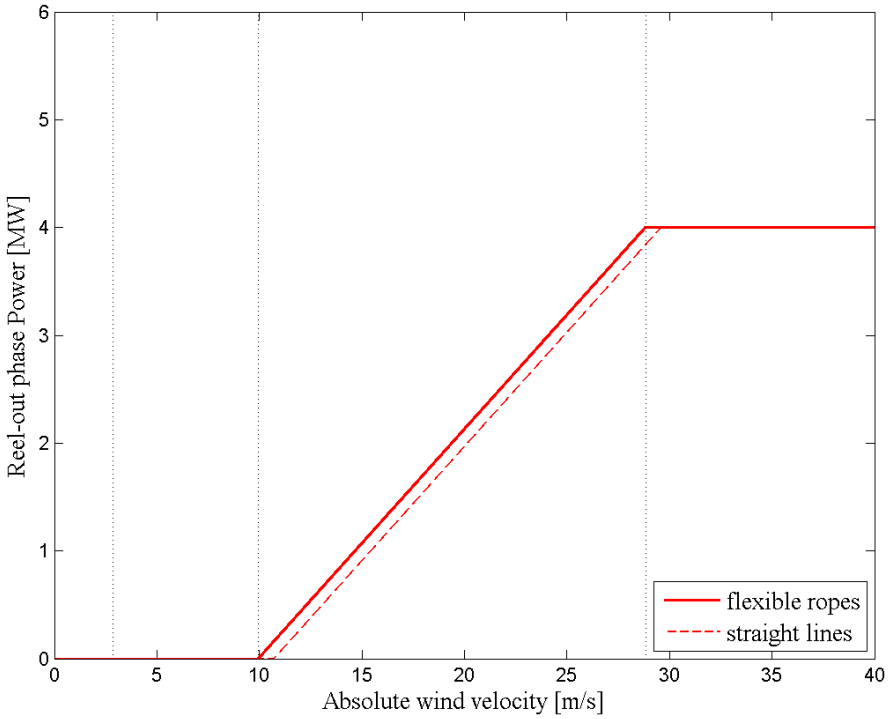

Fig. B. 11: Reel-out phase power vs absolute wind speed of a KiteGen system operating with two 1343m long cables. Comparison between straight lines approach and flexible lines approach.

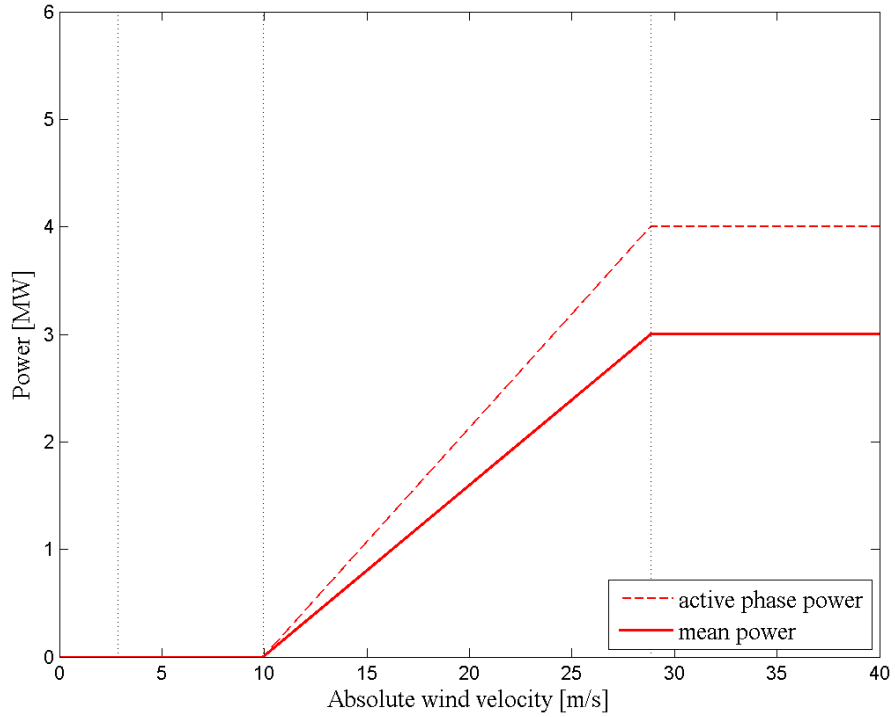

Fig. B. 12: Comparison between the power produced during the active phase and the mean power output of a KiteGen system with two 1343m long flexible ropes.

Cables length:1768 m

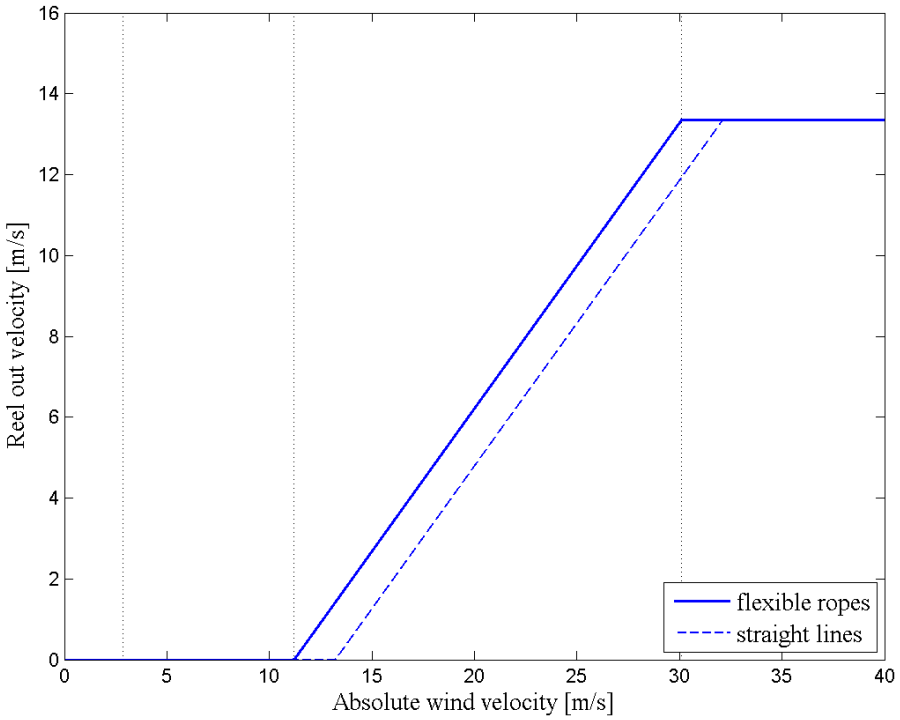

Fig. B. 13: Reel-out velocity vs absolute wind speed of a KiteGen system operating with two 1768m long cables. Comparison between straight lines approach and flexible lines approach.

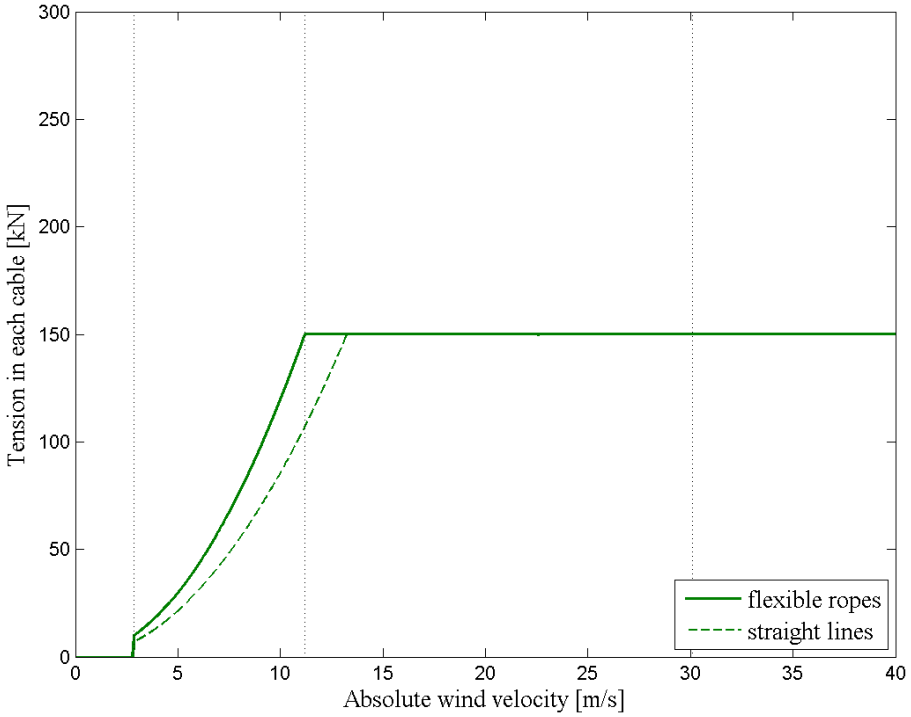

Fig. B. 14: Traction force on each line vs absolute wind speed of a KiteGen system operating with two 1768m long cables. Comparison between straight lines approach and flexible lines approach.

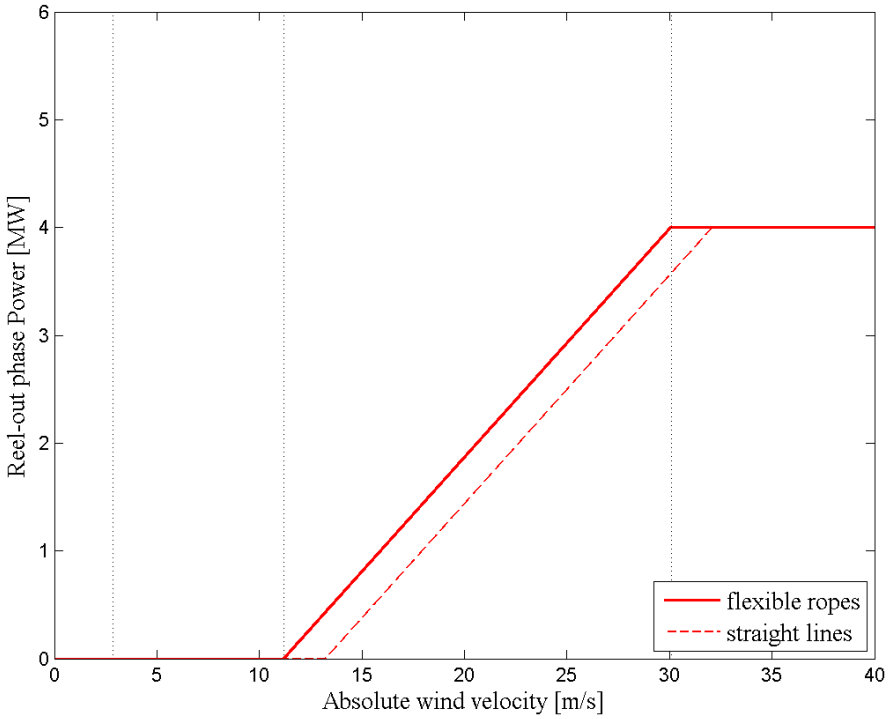

Fig. B. 15: Reel-out phase power vs absolute wind speed of a KiteGen system operating with two 1768m long cables. Comparison between straight lines approach and flexible lines approach.

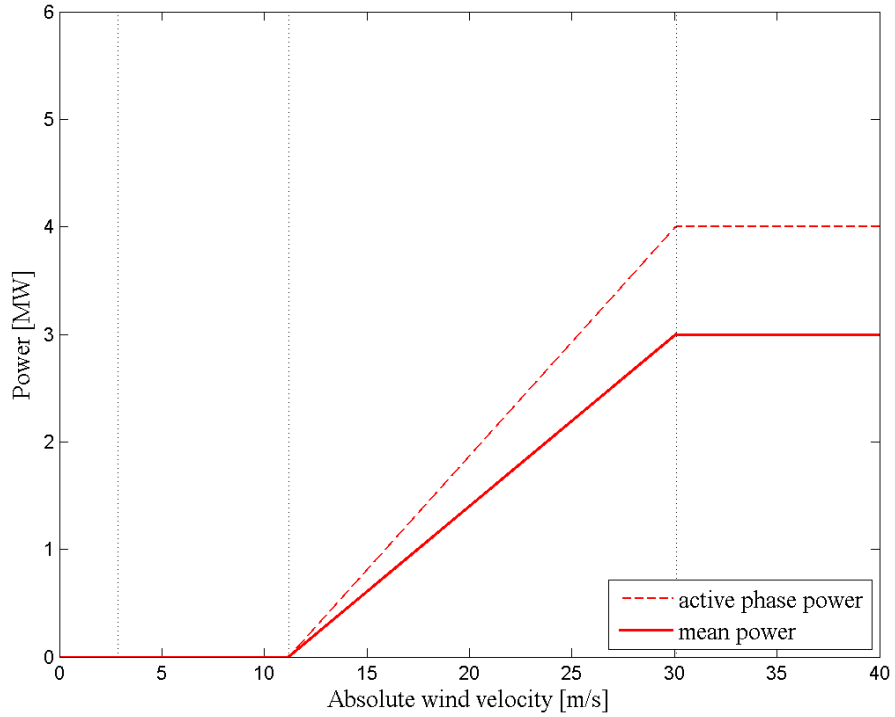

Fig. B. 16: Comparison between the power produced during the active phase and the mean power output of a KiteGen system with two 1768m long flexible ropes.

Cables length: 2192 m

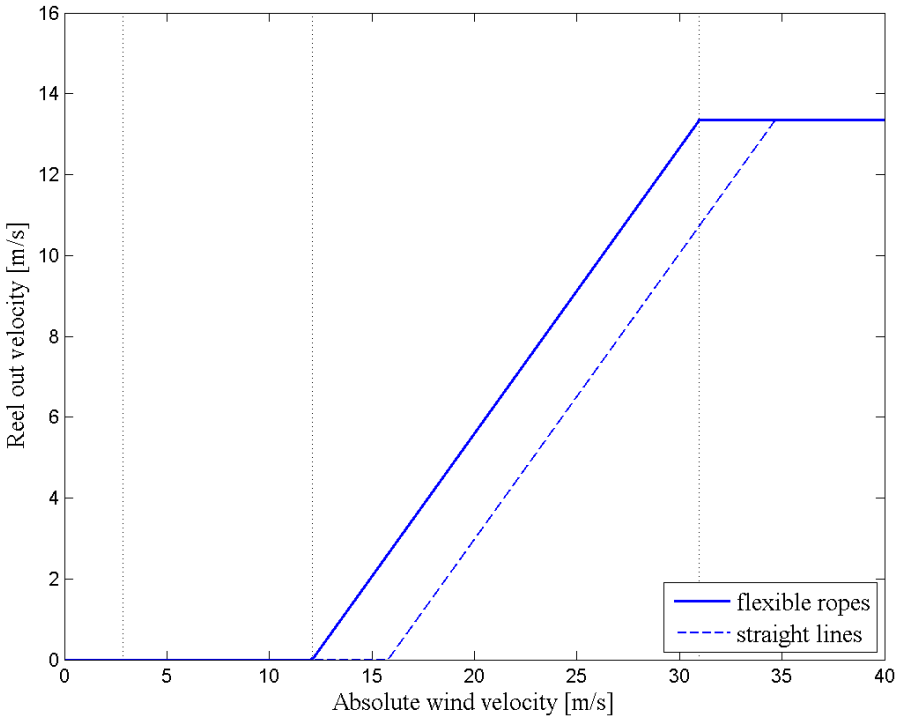

Fig. B. 17: Reel-out velocity vs absolute wind speed of a KiteGen system operating with two 2192m long cables. Comparison between straight lines approach and flexible lines approach.

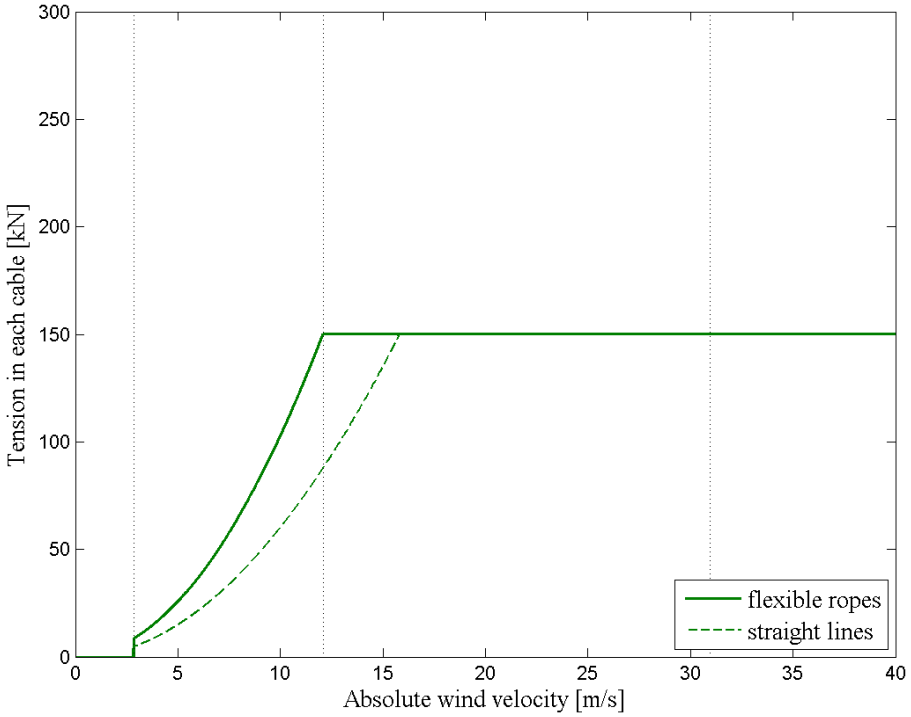

Fig. B. 18: Traction force on each line vs absolute wind speed of a KiteGen system operating with two 2192m long cables. Comparison between straight lines approach and flexible lines approach.

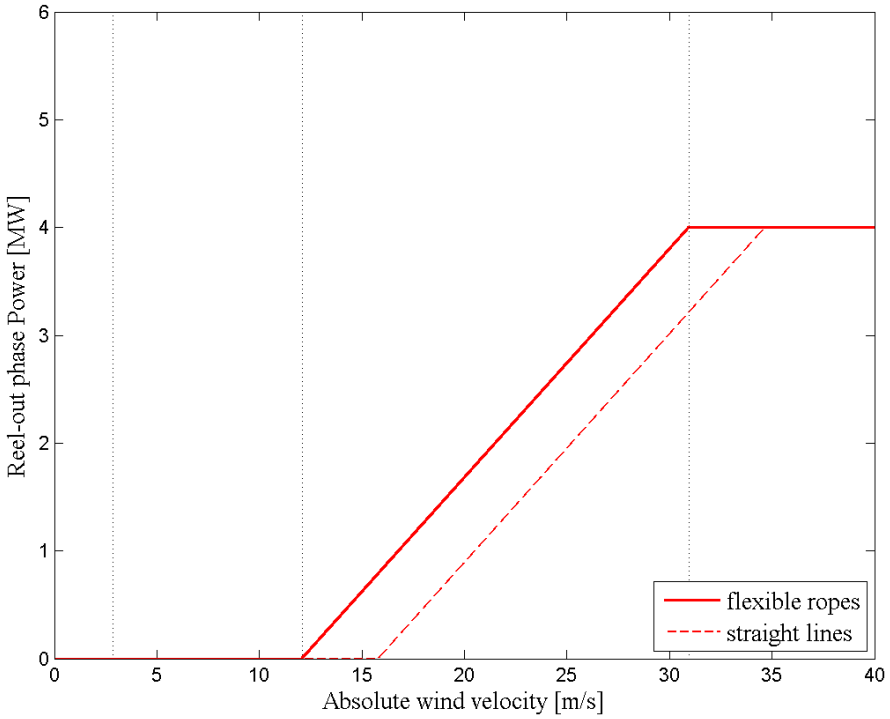

Fig. B. 19: Reel-out phase power vs absolute wind speed of a KiteGen system operating with two 2192m long cables. Comparison between straight lines approach and flexible lines approach.

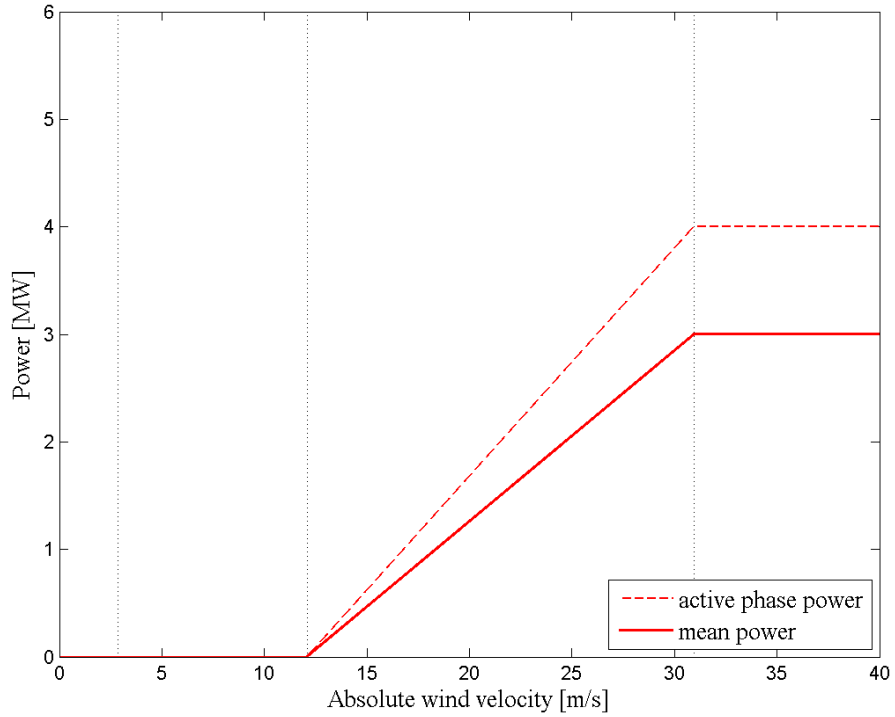

Fig. B. 20: Comparison between the power produced during the active phase and the mean power output of a KiteGen system with two 2192m long flexible ropes.

Cables length: 2616 m

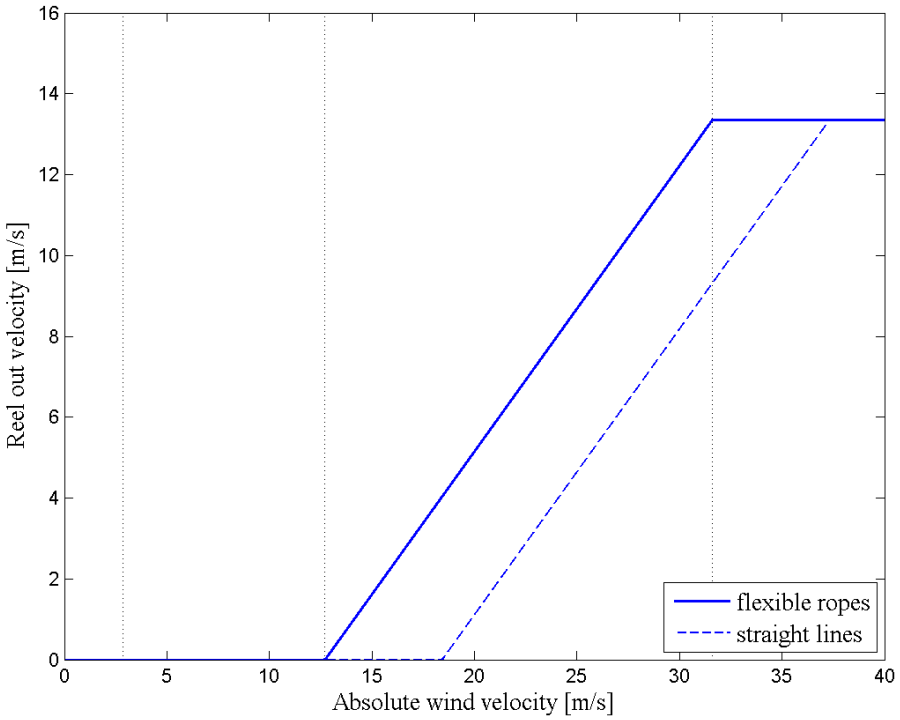

Fig. B. 21: Reel-out velocity vs absolute wind speed of a KiteGen system operating with two 2616m long cables. Comparison between straight lines approach and flexible lines approach.

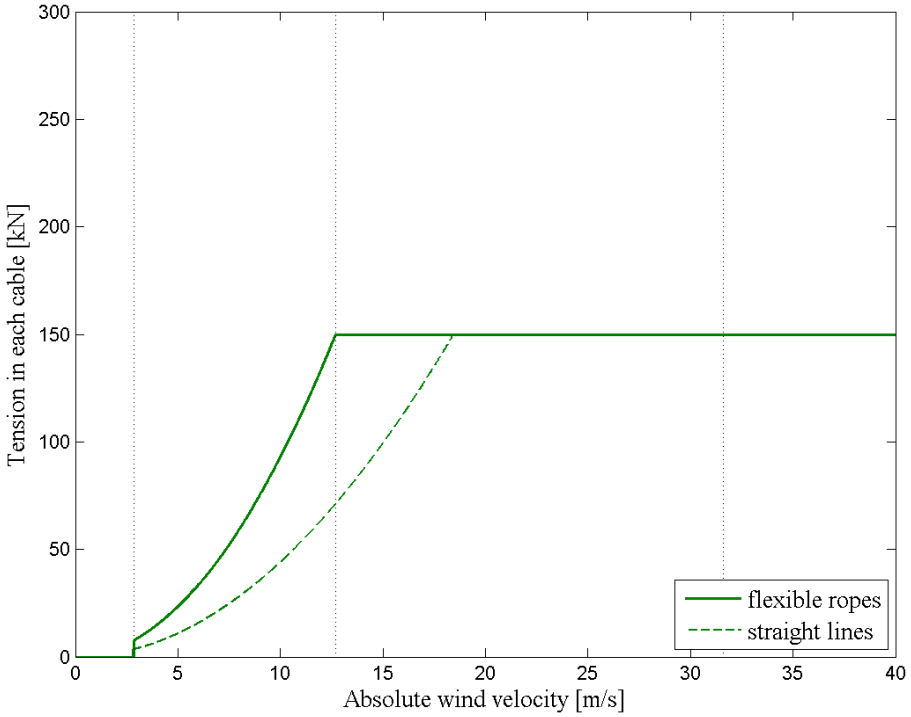

Fig. B. 22: Traction force on each line vs absolute wind speed of a KiteGen system operating with two 2616m long cables. Comparison between straight lines approach and flexible lines approach.

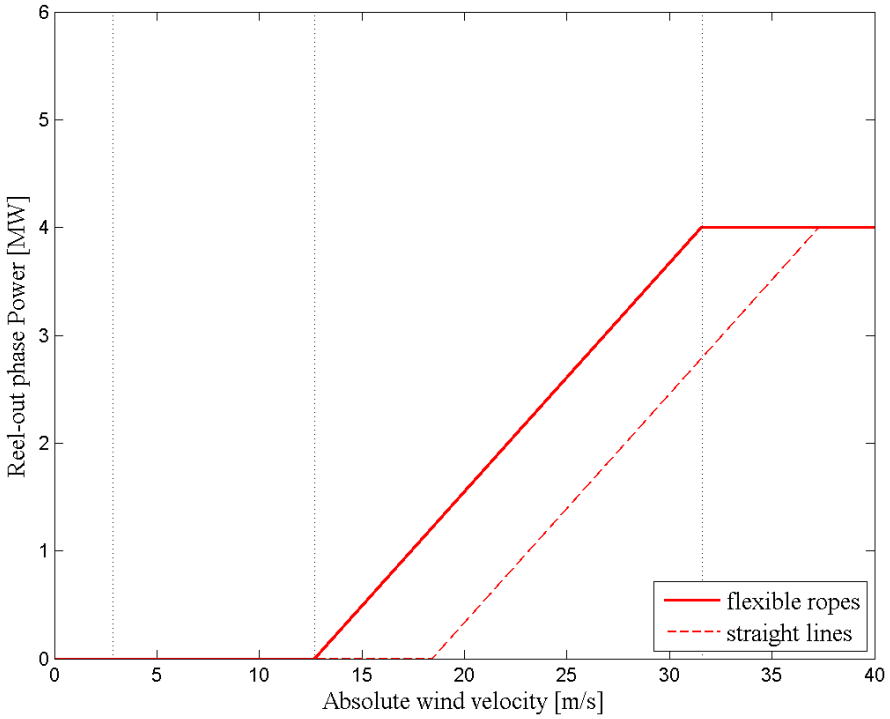

Fig. B. 23: Reel-out phase power vs absolute wind speed of a KiteGen system operating with two 2616m long cables. Comparison between straight lines approach and flexible lines approach.

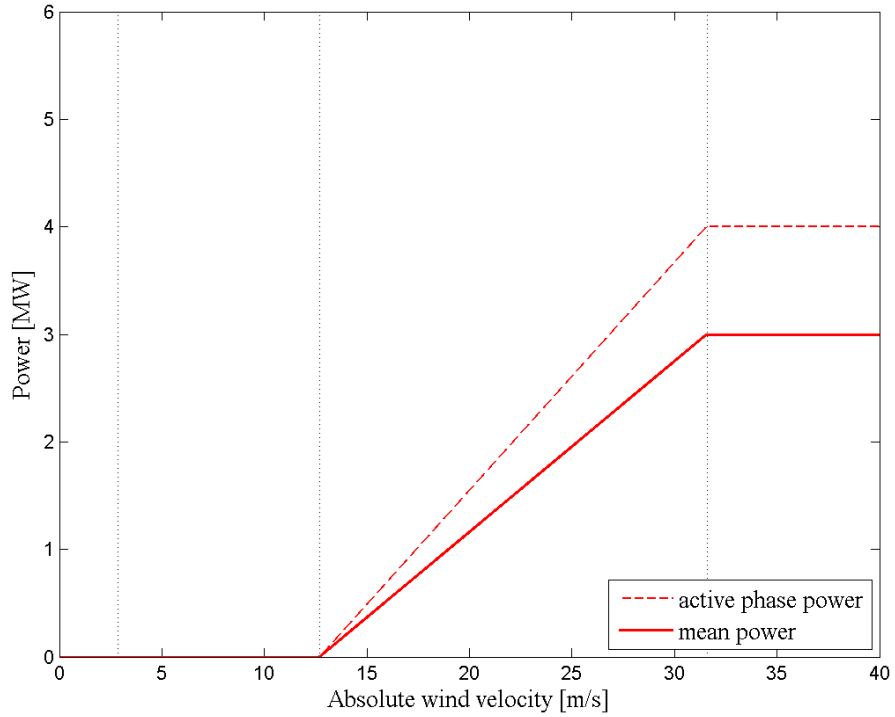

Fig. B. 24: Comparison between the power produced during the active phase and the mean power output of a KiteGen system with two 2616m long flexible ropes.

Cables length: 3000 m

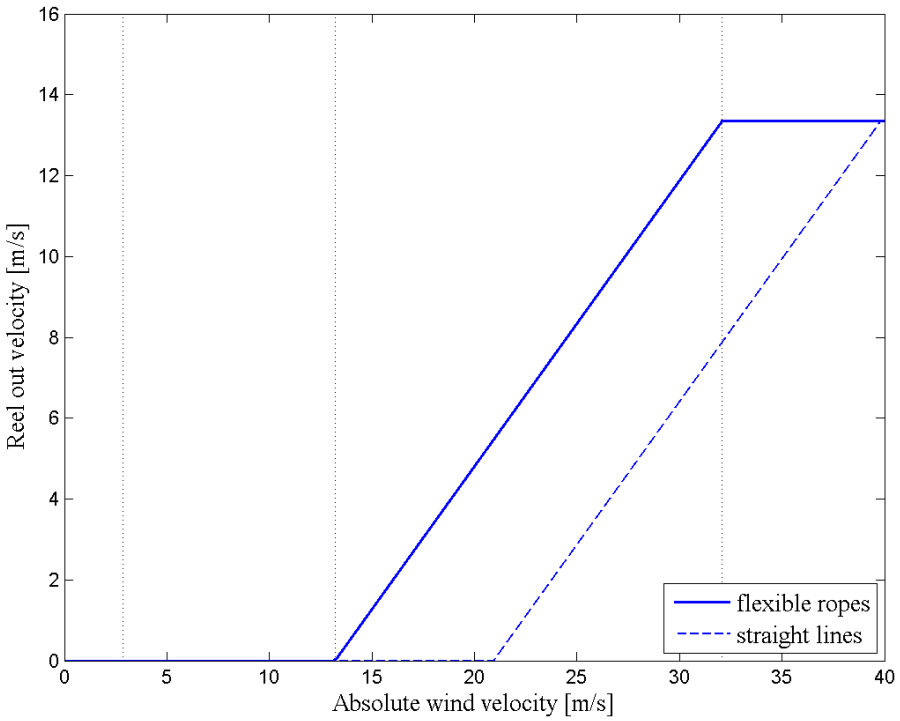

Fig. B. 25: Reel-out velocity vs absolute wind speed of a KiteGen system operating with two 3000m long cables. Comparison between straight lines approach and flexible lines approach.

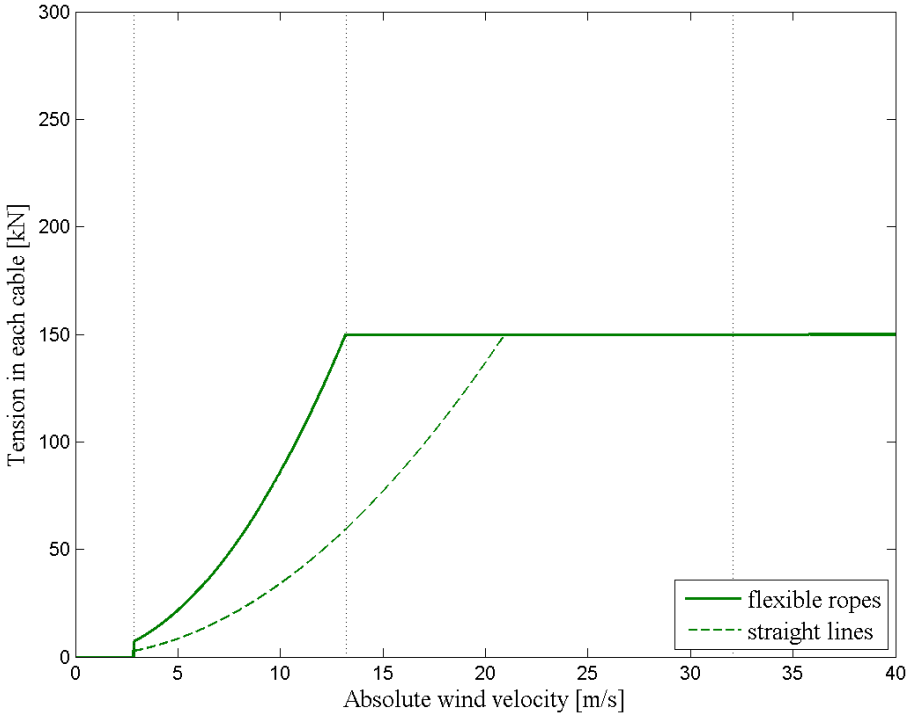

Fig. B. 26: Traction force on each line vs absolute wind speed of a KiteGen system operating with two 3000m long cables. Comparison between straight lines approach and flexible lines approach.

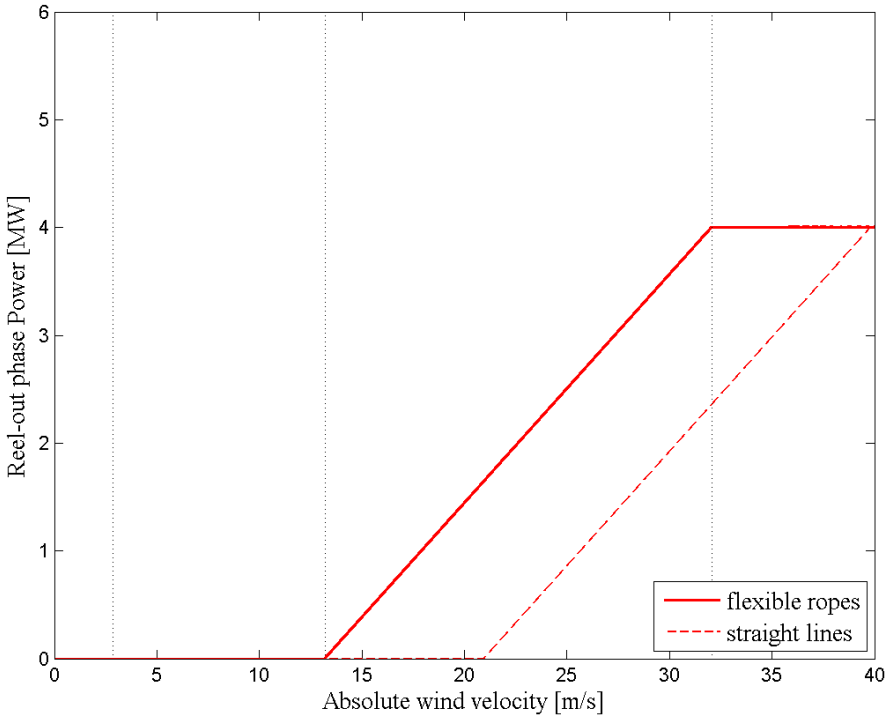

Fig. B. 27: Reel-out phase power vs absolute wind speed of a KiteGen system operating with two 3000m long cables. Comparison between straight lines approach and flexible lines approach.

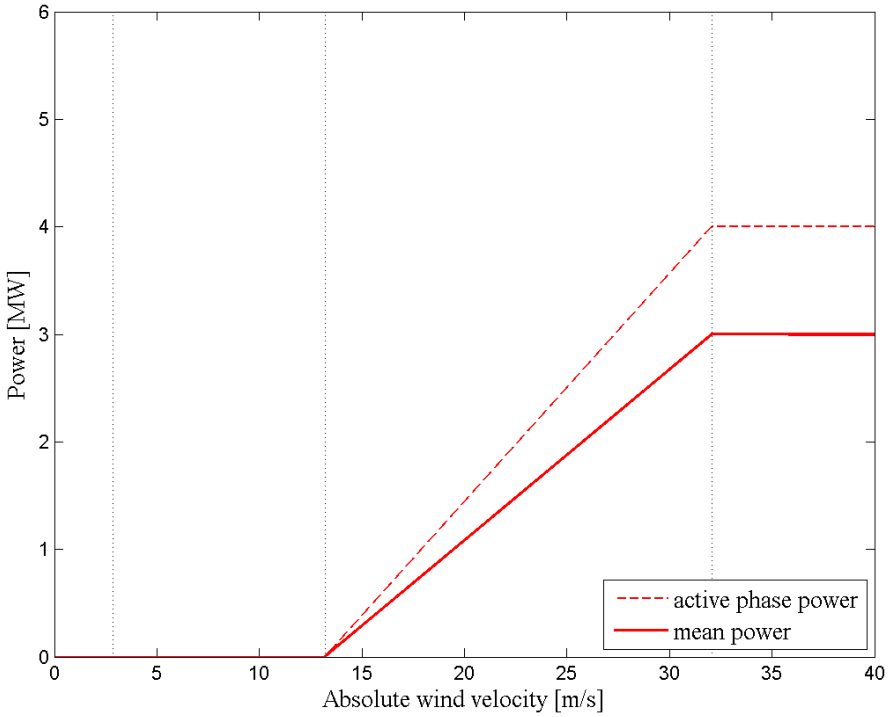

Fig. B. 28: Comparison between the power produced during the active phase and the mean power output of a KiteGen system with two 3000m long flexible ropes.

List of Tables

List of Figures

References

[1] Core Writing Team, R. K. Pachauri, and L.A. Meyer (eds.), "Climate Change 2014: Synthesis Report. Contribution of Working Groups I, II and III to the Fifth Assessment Report of the Intergovernmental Panel on Climate Change," Geneva, Switzerland, 2014, p. 151pp.

[2] International Energy Agency (IEA), "Key World Energy Statistics 2015." Paris, France: IEA PUBLICATIONS, 2015.

[3] International Energy Agency (IEA), "Energy and Climate Change – World Energy Outlook Special Report." Paris, France: IEA PUBLICATIONS, 2015.

[4] World Wind Energy Association, "World Wind Energy Report 2014." 2015.

[5] M. O. L. Hansen, *Aerodynamics of Wind Turbines*, Second Edition. Earthscan, 2008.

[6] International Organization for Standardization, "Standard Atmosphere, ISO 2533:1975." 1975.

[7] C. L. Archer and K. Caldeira, "Global assessment of high-altitude wind power," vol. Energies 2, no. 2, pp. 307–319, 2009.

[8] A. Cherubini, A. Papini, R. Vertechy, and M. Fontana, "Airborne Wind Energy Systems: A review of the technologies," *Renewable and Sustainable Energy Reviews*, vol. 51, pp. 1461–1476, Nov. 2015.

[9] M. Canale, L. Fagiano, M. Ippolito, and M. Milanese, "Control of tethered airfoils for a new class of wind energy generator," in Decision and Control, 2006 45th IEEE Conference on, 2006, pp. 4020–4026.

[10] *http://news.nationalgeographic.com/energy/2015/12/151228-eight-tech-breakthroughs-that-could-help-power-the-world/*. .

[11] *http://www.cleantech.com/indexes/global-cleantech-100/*. .

[12] Italian Council for Eco Innovation, "Rapporto 2015. Tecnologia e Innovazione nella Green Economy Italiana." Settembre-2015.

[13] *http://www.skysails.info/english/power/development/2-demonstrator-1-mw/*. .

[14] *http://twingtec.ch/product/*. .

[15] *http://www.lr.tudelft.nl/en/organisation/departments/aerodynamics-wind-energy-flight-performance-and-propulsion/wind-energy/research/kite-power/automated-control-of-kite-power-systems/*. .

[16] U. Fechner and R. Schmehl, "Design of a Distributed Kite Power Control System," in Control Applications (CCA), 2012 IEEE International Conference on, 2012, pp. 800–805.

[17] *http://www.kitegen.com/en/products/kite-gen-carousel/*. .

[18] *www.kitegen.com*. .

[19] *https://www.google.com/makani/technology/*. .

[20] *http://techcrunch.com/2013/05/22/google-x-acquires-makani-power-and-its-airborne-wind-turbines/*. .

[21] *http://www.jobyenergy.com/*. .

[22] *http://www.bloomberg.com/news/articles/2015-08-27/mitsubishi-heavy-invests-in-altaeros-airborne-wind-technology*. .

[23] L. Fagiano, "Control of Tethered Airfoils for High - Altitude Wind Energy Generation," PhD Thesis, Politecnico di Torino, 2009.

[24] *www.mackiteboarding.com/kiteboarding-wind-window.htm*. .

[25] *www.kiteboardingevolution.com/trainer-kite-practice.html*. .

[26] *https://jezkot.wordpress.com/2007/06/16/kiteboarder-handbook-wind-window/*. .

[27] *www.youtube.com/watch?v=Zl_tqnsN_Tc*. .
[28] C. Novara, L. Fagiano, and M. Milanese, "Direct Data-Driven Inverse Control of a Power Kite for High Altitude Wind Energy Conversion," in Control Applications (CCA), 2011 IEEE International Conference on, 2011, pp. 240–245.
[29] L. Fagiano, M. Milanese, and D. Piga, "High–altitude wind power generation," *IEEE Transactions on Energy Conversion*, vol. 25, no. 1, pp. 168–180, 2010.
[30] B. Houska and M. Diehl, "Optimal control of towing kites," in Decision and Control, 2006 45th IEEE Conference on, 2006, pp. 2693–2697.
[31] M. L. Loyd, "Crosswind Kite Power," *Journal of Energy*, vol. 4, no. 3, pp. 106–111, 1980.
[32] I. Argatov, P. Rautakorpi, and R. Silvennoinen, "Estimation of the mechanical energy output of the kite wind generator," *Renewable Energy*, vol. 34, no. 6, pp. 1525–1532, 2009.
[33] *www.armare.it/*. .
[34] DSM, "Product data sheet: Dyneema® SK99 dtex880." .
[35] *http://radiosondemuseum.org/wp-content/uploads/2012/03/WhatIsARadiosonde.jpg*. .
[36] A. Roshko, "Experiments on the Flow Past a Circular Cylinder at Very High Reynolds Number," *Journal of Fluid Mechanics*, vol. 10, no. 3, pp. 345–356, 1961.
[37] D. J. Tritton, "Experiments on the Flow Past a Circular Cylinder at Low Reynolds Numbers," *Journal of Fluid Mechanics*, vol. 6, no. 4, pp. 547–567, 1959.
[38] *http://scienceworld.wolfram.com/physics/CylinderDrag.html*. .
[39] M. Belan and D. Tordella, "Asymptotic Expansion for Two Dimensional Symmetrical Laminar Wakes," *Zamm*, vol. 82, no. 4, p. 219, 2002.
[40] I. Argatov, P. Rautakorpi, and R. Silvennoinen, "Apparent wind load effects on the tether of a kite power generator," *Journal of Wind Engineering and Industrial Aerodynamics*, vol. 99, no. 10, pp. 1079–1088, Oct. 2011.